International Journal of Aerospace Engineering

Load Transportation using Aerial Robots

Lead Guest Editor: Ti Chen
Guest Editors: Miaomiao Wang, Hao Wen, and Junyi Geng

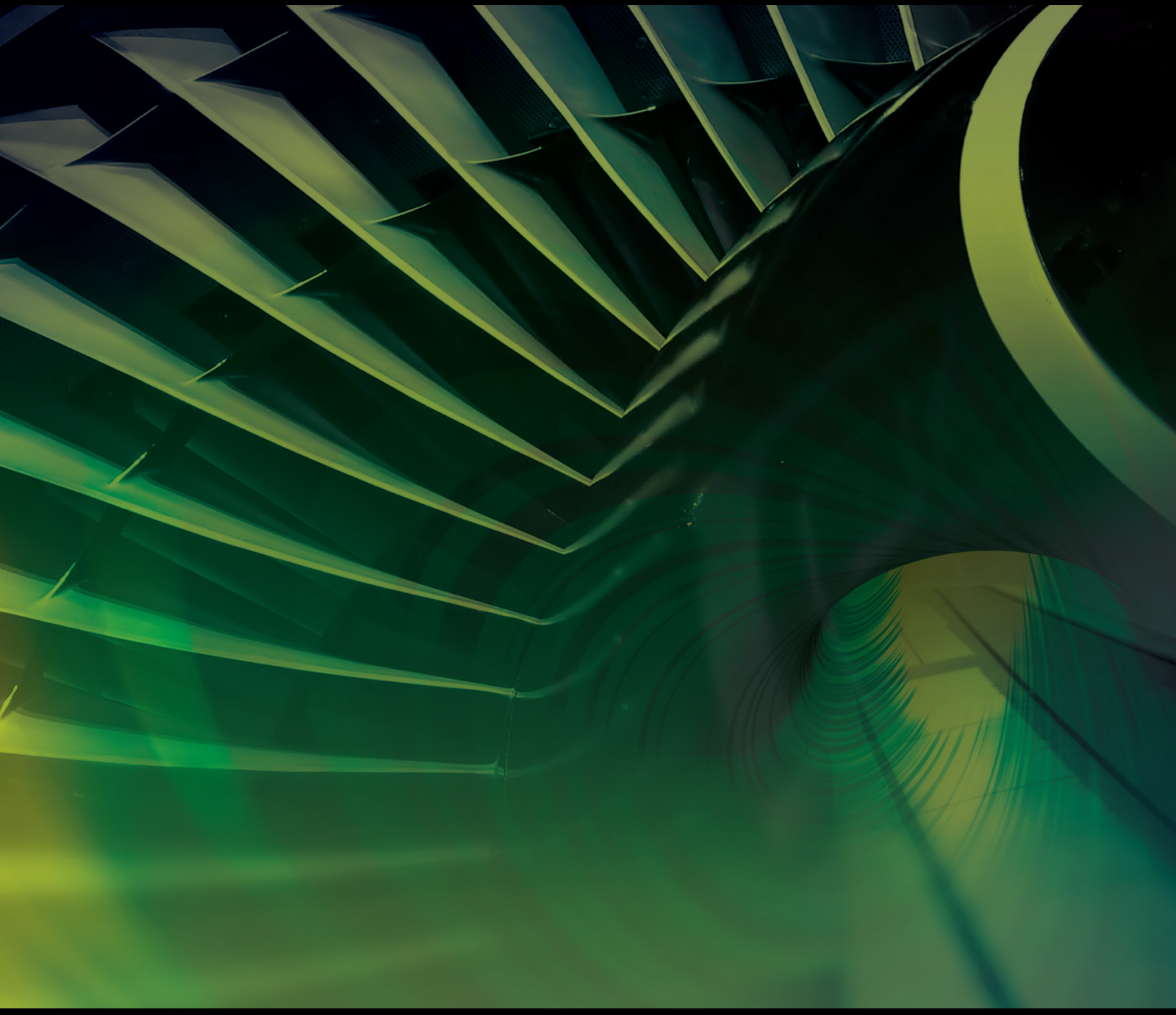

Load Transportation using Aerial Robots

International Journal of Aerospace Engineering

Load Transportation using Aerial Robots

Lead Guest Editor: Ti Chen
Guest Editors: Miaomiao Wang, Hao Wen, and Junyi Geng

Contents

Hindawi
International Journal of Aerospace Engineering
Volume 2022, Article ID 2002423, 11 pages
https://doi.org/10.1155/2022/2002423

Research Article

Optimization of Lateral Collision Risk of Aircraft Based on the Skid-Slip Event Model

Hao Liu,[1] Daiwu Zhu,[2] Xiaofan Xie,[3] Jiuhao Chen,[4] and Xiaokang Liu[5]

[1]*College of ATM, Civil Aviation Flight University of China, Guanghan, 618300 Sichuan, China*
[2]*Library, Civil Aviation Flight University of China, Guanghan, 618300 Sichuan, China*
[3]*Center for Teacher Development and Teaching Evaluation, Civil Aviation Flight University of China, Guanghan, 618300 Sichuan, China*
[4]*Academic Affairs Office, Civil Aviation Flight University of China, Guanghan, 618300 Sichuan, China*
[5]*School of Electronic Information, Zhongyuan University of Technology, Zhengzhou, 450007 Henan, China*

Correspondence should be addressed to Daiwu Zhu; 364890003@qq.com

Received 7 March 2022; Revised 11 June 2022; Accepted 7 July 2022; Published 15 July 2022

Academic Editor: Ti Chen

With the development of aircraft flow under the existing airspace capacity now, the shortage of airspace resources and flight delays have become significantly severe. Therefore, building a safe and efficient mathematical model from quantitative analysis and improving the scientificity of route planning and management are essential propositions for future research on new navigation systems. Based on the traditional event collision risk assessment model, the collision module is upgraded to an ellipsoid according to the performance of aircraft, integrating the boundary curvature optimization characteristics of the TSRRT (task-space rapidly-exploring random trees) algorithm. An aircraft event lateral conflict resolution model based on the TSRRT algorithm is proposed. Taking the A320 aircraft and 737-800 aircraft as experimental subjects, the corresponding collision coefficients are imported into software tools for the simulation and the Kalman filtering is combined to verify the smoothness of the front and rear boundary curvatures. The result proves that the event side collision risk of aircraft based on TSRRT is 15% of the traditional event model and the smooth curvature error is reduced by 80% due to the improvement. Therefore, the improved event model is practical and valuable, providing a theoretical basis for future track-based operations.

1. Introduction

With the rapid increase of aircraft flow, the existing air route network has become congested with limited airspace resources, which not only limits the increase in flight traffic but also causes much insecurity to flight [1]. Therefore, it is necessary to evaluate the collision risk of navigation from the scientific quantification perspective.

Domestic and foreign scholars have made many efforts to research the airway collision risk model. In 1966, Reich proposed the earliest collision risk model when evaluating the safety of separation standards for the North Atlantic route [2]. In 1984, Brooker applied the Reich model to the North Atlantic lateral collision risk study [3]. Brewer-Dougherty et al. [4] established a collision risk model of PBN (performance-based navigation) based on the Reich model in 2016. However, Kim and Hwang [5] conducted a practical comparison and analysis of the event model and Reich model in 2018, finding out that the event models are more inclusive and the models have apparent advantages in applying multiple integrations and superimposed factors. The event model (also known as the post-Reich model) was proposed by professor Brooker [6] of the United Kingdom in 2003, and a traditional cuboid collision template was established. In 2008, Xiaohao et al. [7] proposed using a cylindrical collision template instead of the traditional one to realize the function of risk assessment and calculating lateral intervals. In 2010, Wenjun et al. [8] used a spherical collision template to replace the traditional template to assess the safety of cross-route separation. In 2011, Yuling et al. [9] established a collision risk model based on a given arrival time interval for the flight at the same altitude and the same

direction with the help of the probability theory. In 2013, Zongping et al. [10] analyzed the approach risk of paired aircraft based on the accident tree analysis method and obtained the variation curve of the aircraft's longitudinal collision risk with relevant parameters through simulation calculation. It was assessed by Xingwu and Zhaoning [11] in 2015. In 2017, Jian [12] fully considered the speed error, navigation error, initial safe distance, and other factors of the two aircraft during the paired approach of the short-distance parallel runway to establish a paired approach collision risk assessment model; in 2018, Xinsheng and Zhi [13] studied the flight interval and conflict relief threshold under the influence of multiple random factors. In 2019, Shuo [14] used a cylinder-rectangular collision temlate to study the collision probability of UAVs. In 2021, Xie et al. [15] comprehensively considered the influence of aircraft yaw and established a paired approach longitudinal collision risk assessment model for the longitudinal separation calculation of aircraft at each stage. However, none of the above-mentioned event collision models can reflect the speed vector changes in the aircraft space and the aircraft sideslip curvature cannot be described. More importantly, due to the aircraft's pitch angle limitation, the aircraft will generally change the height to prevent a collision when the two aircraft are approaching, so the space formed by the aircraft's deflection around the lateral axis of the wing is not a cuboid or sphere, but a cylinder close to it. Therefore, a skid-slip event lateral conflict resolution model is proposed to analyze and study the lateral risk of the air routes.

2. Event Lateral Model Construction and Improvement

2.1. Event Model Construction. The event model evaluates the collision risk of adjacent-tracking aircraft (labeled AIR-A and AIR-B) with a lateral separation of S. AIR-A is used as the center point to simulate a cylinder with a radius of D (λ_x and λ_y representing the horizontal and vertical lengths of the aircraft, respectively. It is assumed that the wingspan and the length of the aircraft are equal, that is, $\lambda_x = \lambda_y$, both expressed in terms of aircraft length D) and a height of $2\lambda_z$ (the height of the aircraft is represented by λ_z, taking the center point of the aircraft as the center of the cylinder, and the height of the cylinder is $2\lambda_z$) [16]. AIR-B is used as the origin to simulate a plane with no thickness on the x–z-axes. When the spacing piece of AIR-B is in contact with the cylinder of AIR-A, that is, AIR-A and AIR-B are in an absolute collision, the schematic diagram is described in Figure 1 as follows.

For AIR-A and AIR-B, T_C is used to represent the voyage time and the number of collisions per unit time of voyage can be expressed as follows:

$$\mathrm{CR} = 2\mathrm{NP} \times \mathrm{HOR}(T_C) \times P_z(S_z) \times \left(1 + \frac{\pi D|z|}{4\lambda_z V_{\mathrm{rel}}^C}\right), \quad (1)$$

where NP is the number of aircraft logs per hour and HOR (T_C) is the probability that AIR-A and AIR-B overlap

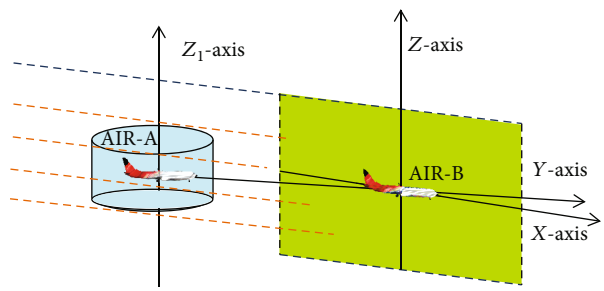

Figure 1: The collision box laterally traverses the spacer layer.

horizontally. $P_z(S_z)$ is the probability that AIR-A and AIR-B overlap vertically when the horizontal overlap occurs, which generally takes a fixed value of 6.6×10^{-6}. $|z|$ is the average vertical relative speed. V_{rel}^C is the average horizontal relative speed. When studying the lateral risk model of adjacent trajectories, the voyage report period is set to T hours, the number of planes is set to $\mathrm{NP} = 1/T$ when calculating the lateral interval, and it is assumed that the two planes fly at the cruise level. When the lateral interval is unknown, it can be replaced by $P_z(0)$ and the number of collisions per hour on the same track can be expressed as follows:

$$\mathrm{CR}(T) = \frac{2}{T} \times \mathrm{HOR}(T + \tau) \times P_z(0) \times \left(1 + \frac{\pi D|z|}{4\lambda_z V_{\mathrm{rel}}^C}\right). \quad (2)$$

τ is the communication and controller intervention buffer value based on the CPDLC data link (controller and pilot data link communication); the horizontal overlap probability $\mathrm{HOR}(T + \tau)$ is based on the vertical overlap probability and lateral overlap at $t = T + \tau$. So, the probability can be expressed as follows:

$$\begin{aligned} &\mathrm{HOR}(T + t) = \mathrm{LOP} \times P_y(0), \\ &P_{(T+t)} = \mathrm{LOP} \times P_y(0) \times P_z(0) \times \left(1 + \frac{\pi D|z|}{4\lambda_z V_{\mathrm{rel}}^C}\right), \end{aligned} \quad (3)$$

where LOP is the probability of the longitudinal overlap and $P_y(0)$ is the probability of the lateral overlap of 2 aircraft on adjacent levels of the track.

2.2. Collision Ratio R

2.2.1. Conavigation Collision Relationship Ratio R. Figure 2 shows the movement of the crash box laterally and longitudinally across the spacer in the case of codirectional flight. If a collision occurs, the aircraft point B must be within the line segment JK. When the aircraft point B is outside the line segment JK on the line segment IL, that is, on the line segment IJ and the line segment KL, there will be no collision. In the event model, since the collision box is the cuboid shown in the figure, during the entire process of crossing the spacer, as long as point B is on the line segment IL, a collision may occur. When flying on the same heading, the collision box laterally traverses the spacer and moves in the lateral and longitudinal directions. According to the geometric principles, point B collides in the line segment JK.

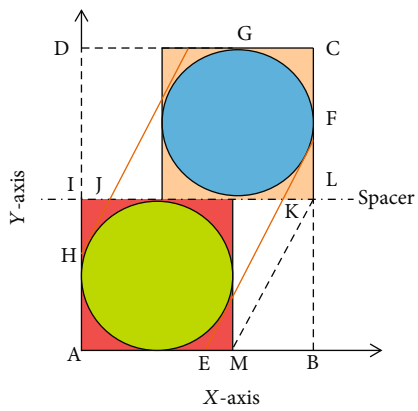

Figure 2: Collision geometry diagram in the same direction.

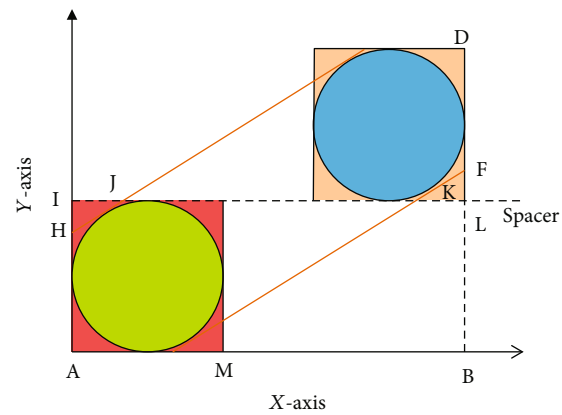

Figure 3: Reverse navigation collision geometry diagram.

Otherwise, it does not crash. According to the characteristics of the event model, it can be described that when point B is on the line segment IL, AIR-A and AIR-B will hit each other.

Assuming that B is relatively stationary, considering the collision probability relationship ratio $R(S)$ from a geometric point of view, the longitudinal movement distance of AIR-A is BM, which can be expressed as follows:

$$R(S) = \frac{\mathrm{JK}}{\mathrm{IL}}, \quad \mathrm{BM} = \frac{2D}{V} \times U. \tag{4}$$

U, V, and W are the relative velocities of A-AIR through the AIR-B spacer in the longitudinal, lateral, and vertical directions when sailing in the same direction [17]. At the same time, they can float in the same direction according to the geometry and the event model motion principle. The collision probability relationship ratio is as follows:

$$R(S) = \frac{U + 2V}{2U + 2V}. \tag{5}$$

2.2.2. Reverse Navigation Collision Relationship Ratio R1. The longitudinal relative speed of AIR-A and AIR-B when cruising in the reverse direction is $2U_{\mathrm{at}}$. It is assumed that the relative speed change value in the lateral and vertical movement is 0, that is, the time for the reverse sailing to pass through the interval is equal to the time in the same direction. The schematic diagram of the collision cylinder passing through the spacing piece when traveling in the reverse direction is shown in Figure 3.

According to Figure 3, considering the geometric ratio relationship, the length of MB and IL can be expressed as follows:

$$\mathrm{MB} = \frac{2D}{V} \times 2U_{\mathrm{at}}, \quad \mathrm{IL} = 2D + \frac{2D}{V} \times 2U_{\mathrm{at}}. \tag{6}$$

Since IL is much larger than KL, the approximate length of the KL line segment is D and the collision probability relationship between AIR-A and AIR-B when sailing in the reverse direction is as follows:

$$R(O) = \frac{2U_{\mathrm{at}}}{2U_{\mathrm{at}} + V}. \tag{7}$$

2.3. Integration of Skid-Slip Event Model. Since the TSRRT algorithm will integrate kinematic model constraints into the route planning, the curvature of the overall planning can be optimized so that the path curvature can meet the need for parameter continuity [18]. Also, it is easy to solve the length of the line segment and rough value of KL in the same direction and reverse navigation collision geometric model. Because the TSRRT algorithm adopts the Dubins curve, it can effectively reduce the convergence time of risk assessment when the sailing demands are met.

The motion model of the Dubins curve only allows the moving body to move forward and not to return, and the line can connect the shortest path in a two-dimension surface under the circumstances that the curve is satisfied with path constraints. This article uses RSL to represent the shortest path connecting the two control points of P_0 and P_1, where the radius in the curve circle is the radius of the bottom surface of the cylinder. That is, R and D are equal and the corresponding RSL diagram is shown in Figure 4 as follows.

The TSRRT firstly samples and marks the nodes in the areas prone to lateral overlap, integrating the heuristic function to calculate the value of the central point of the lateral adjacent overlap area. Let G be the combination of adjacent nodes with the smallest total value of the current risk.

$$G = \arg\min\,(H(S)). \tag{8}$$

$H(S)$ is the substitute value of adjacent overlapping risk areas. Let $H(Q)$ be the total risk calculation cost from the initial risk overlapping point to the current period, and

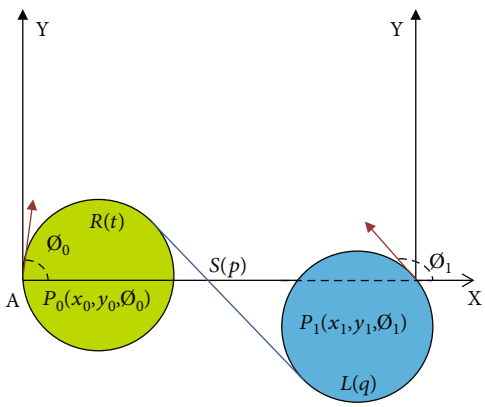

Figure 4: Schematic diagram of RSL.

$H(G)$ is the estimated value at risk from the current period to the target point.

$$H(Q) = \sum_{i=2}^{n} L_{bci},$$
$$L_{bci} = \frac{2L_c + (n-1)L_p}{n+1}. \tag{9}$$

L_{bci} is the approximate length of the i_{th} adjacent point and the Bezier curve, and n is the Bezier order, which is the side collision surface of A-AIR and B-AIR running in the same or reverse direction.

3. Kalman Filter Error Model Based on RNP

The fusion of the TSRRT algorithm and the event model could reduce the convergence time and increase the accuracy of KL under geometric analysis. However, it cannot meet the requirements of free navigation in the ICAO.DOC9750 global navigation plan [19]. The yaw probability-based Kalman filtering is introduced to evaluate the multifactor superimposition effect on the collision model so that the practicability, accuracy, and reproducibility of the event lateral conflict model can be improved in future navigation systems [20, 21]. The total yaw error TSE (total system error) under lateral confliction error is generally composed of NSE (navigation system error), PDE (path definition error), and FTE (flight technical error). The RNP (required navigation performance) program can be selected as a benchmark when measuring the error probability under lateral conflict. RNPN can be described as the aircraft's actual position being within ±95% of the total flight time. In other words, it is safe in the range of N NM [22, 23] and there will be no risk of collision, as shown in Figure 5.

The Kalman filter is based on the theory of the state equation and motion vector equation of the moving aircraft, and the least mean square error is used as the reference to estimate the system state [24]. Therefore, the minimum mean square error threshold can be selected to correspond to the RNP regulations. The filter error is used to measure the event's lateral direction, the applicability, and the rationality of the conflict model. The Kalman system equation is as follows:

$$\begin{aligned} X(n) &= A(n|n-1)X(n-1) + B(n|n-1)\omega(n-1), \\ Z(n) &= H(n)X(n) + v(n), \end{aligned} \tag{10}$$

where $X(n)$ is the state vector, which represents the value of the motion vector at time n. $A(n \mid n-1)$ is the state transition matrix used to describe the motion of the target object. $B(n \mid n-1)$ is the interference transition matrix. $\omega(n)$ represents the system noise of the motion model. $Z(n)$ represents the observation vector, describing the observation value at time n. $H(n)$ is the observation matrix; $v(n)$ is the motion observation noise generated during the estimation process, and $\omega(n)$ and $v(n)$ are independent of each other. Its statistical characteristics are as follows:

$$\begin{aligned} E\left[\omega(n)\omega^T(i)\right] &= \begin{cases} Q(n), & i = n, \\ 0, & i \neq n, \end{cases} \\ E\left[v(n)v^T(i)\right] &= \begin{cases} R(n), & i = n, \\ 0, & i \neq n, \end{cases} \end{aligned} \tag{11}$$

$$E\left[w(n)v^T(i)\right] = 0. \tag{12}$$

At the same time, the Kalman equation of motion can be divided into the time update equation and the observation update equation, here named

$$\begin{aligned} X(n|n-1) &= A(n|n-1)X(n-1|n-1), \\ P(n|n-1) &= A(n|n-1)P(n-1|n-1)\cdot A^T(n|n-1) \\ &\quad + B(n|n-1)Q(n-1)\cdot B^T(n|n-1), \\ X(n|n) &= X(n|n-1) + K(n)[Z(n) - H(n)X(n|n-1)], \\ K(n) &= P(n|n-1)H^T(n)\left[H(n)\cdot P(n|n-1)H^T(n) + R(n)\right]^{-1}, \\ P(n|n) &= [I - K(n)H(n)]P(n|n-1), \end{aligned} \tag{13}$$

where $Q(n)$ is the symmetric nonnegative definite azimuth matrix of the system noise $\omega(n)$. $R(n)$ is the symmetric positive definite variance matrix of the observation noise $v(n)$. $P(n \mid n)$ is the error variance matrix. $K(n)$ is the filter gain matrix [25].

According to the definition of the abovementioned system equations and the physical relationship of the

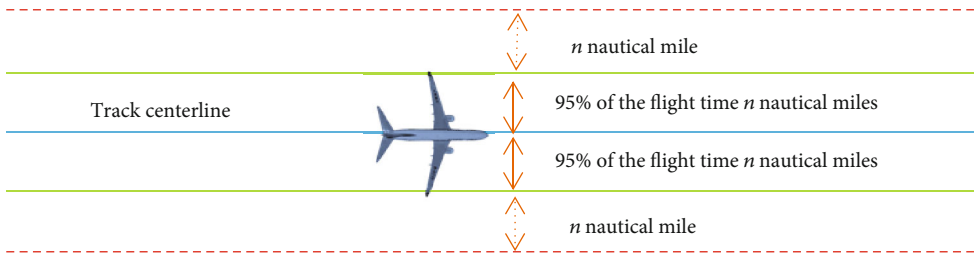

Figure 5: Schematic diagram of the RNP procedure.

parameters, the state transition matrix $A(n \mid n-1)$ and the observation matrix $H(n)$ can be obtained.

$$A(n|n-1) = \begin{bmatrix} 1 & 0 & T & 0 & \frac{T^2}{2} & 0 \\ 0 & 1 & 0 & T & 0 & \frac{T^2}{2} \\ 0 & 0 & 1 & 0 & T & 0 \\ 0 & 0 & 0 & 1 & 0 & T \\ 0 & 0 & 0 & 0 & 1 & 0 \\ 0 & 0 & 0 & 0 & 0 & 1 \end{bmatrix}, \quad (14)$$

$$H(n) = \begin{bmatrix} 1 & 0 & 0 & 0 & 0 & 0 \\ 0 & 1 & 0 & 0 & 0 & 0 \end{bmatrix}. \quad (15)$$

4. Simulation Calculations

To test the effectiveness and efficiency of the aircraft event lateral conflict resolution model based on TSRRT, an Intel Core i7 processor is selected as the hardware operating environment with a 16 GB memory capacity.

The wingspan, fuselage, and fuselage heights of the A320 aircraft are 34.1 m, 37.6 m, and 11.8 m, respectively, $R_1 = \max(34.1, 37.6)$ (unit: m). The wingspan, fuselage, and fuselage height of the B737-800 aircraft are 35.79 m, 39.47 m, and 12.57 m, respectively, $R_2 = \max(35.79\,\text{m}, 39.47\,\text{m})$. The ADS-B-based position and time information of the A320 and B737-800 aircraft are selected as the primary simulation data in the experiment. Some of the position and time data are shown in Tables 1 and 2.

According to the requirements of ⟪introduction to safety assessment of flight intervals⟫ [26], considering the maximum risk of lateral collision, the lateral relative velocity v is set to 6.44 m/s and the longitudinal relative velocity u is set to 514 m/s, vertical relative velocity $|z| = w = 0.78$ m/s, $D_1 = 37.6$ m, $D_2 = 39.47$ m, $\lambda_{z1} = 11.80$ m, and $\lambda_{z2} = 12.57$ m. According to the literature [27–29], the lateral overlap probability is $P_y(0) = 0.0432$, the longitudinal overlap probability $\text{LOP} = P_x(0) = 0.0432$, the vertical overlap probability $P_z(S_z) = 6.6 \times 10^{-6}$, the longitudinal proximity rate $E(0)$ is 0.01, $\tau = 4$ min, the longitudinal interval W of the aircraft is 10 km, the target offset rate $P_{\text{goal}} = 0.1$, the maximum curvature $k_{\max} = 0.05$, the maximum sideslip steering angle $\gamma = 0.4$ pi, and the sampling step length $d = 10$ km, as shown in Table 3.

The event parameters set in Table 3 are brought into the lateral conflict model, and the collision risk values of the original cylindrical event lateral conflict model and the improved skid-slip event lateral conflict model are obtained; the obtained calculation result (retaining two decimal places) is shown in Table 4.

As the safety target level specified in ICAO Annex 6 11th Edition [30] is 5×10^{-9}, the collision probabilities of the traditional event model and the improved skid-slip event model are 1.12×10^{-10} and 7.48×10^{-10}, respectively, when choosing the 1st combination (A320), which meets the target level specified by ICAO, and the optimized event collision probability becomes 15% ($1.12 \times 10^{-10}/7.48 \times 10^{-10}$). Similarly, the collision probabilities of the traditional event model and the improved skid-slip event model are 1.12×10^{-10} and 7.43×10^{-10} when using the B737-800 combination. The collision probability of the B737-800 combination model before and after the improvement is less than 5×10^{-9}, and the optimized event collision probability becomes 15% ($1.12 \times 10^{-10}/7.43 \times 10^{-10}$) of the traditional event model.

5. Main Factor Analysis and Improved Model Test

5.1. Analysis of Main Factors. It can be seen in Tables 3 and 4 that the collision risk probability is mainly affected by the flight time and the speed error. The following mainly analyzes the collision risk from the two aspects of the flight time change and the speed error parameter. Let the airplane speed $v = 460$ kt, the value of airplane speed error parameter $\sigma = 7.0$, and the time interval be 5 min. The safety target-level risk time specified in ICAO Annex 6 is 5×10^{-9} times/flight hour [30], and the logarithm based on 10 is $\lg(5 \times 10^{-9}) = -8.301$, which is different for different RNP specifications. The changing trend of collision risk is shown in Figure 6.

It can be seen in Figure 6 that the risk of collision and the collision specifications of different navigation sources also differ significantly as the flight time increases. Taking RNP4 as an example, the collision risk changes from 10^{-18} to 10^{-9} overtime. The collision risk change interval of RNP10 is $[10^{-11}, 11^{-9}]$ because the navigation error parameter value of RNP10 is 5.1, which is 2.5 in the case of RNP4. The difference in navigation specifications makes the flight error significantly increase. When the flight time is 90 minutes, the collision risk of RNP10 is 5.3×10^{-9} (which is

Table 1: Part of the A320 passenger location and time information table based on ADS-B.

Serial numbers	Times	Latitudes	Longitudes	Heading	m/s
01	07:47:16	29.3472	118.3324	120°	213.6
02	07:48:10	29.3037	118.2116	120°	225.2
03	07:49:10	29.2551	118.0766	120°	233.3
04	07:49:43	29.2293	118.0037	120°	232.7
			…		
20	08:02:15	28.6792	116.4662	120°	226.6
21	08:02:45	28.6568	116.4034	120°	231.7
22	08:03:15	28.6332	116.3378	120°	233.3
			…		

Table 2: Part of B737-800 location time information table based on ADS-B.

Serial numbers	Times	Latitudes	Longitudes	Heading	m/s
01	07:47:16	28.4138	118.4220	143°	226.7
02	07:48:10	28.4060	118.3654	143°	230.6
03	07:49:10	28.3941	118.2832	143°	234.2
04	07:49:43	28.3838	118.2149	143°	232.5
			…		
20	08:02:15	28.3740	116.1492	143°	231.9
21	08:02:45	28.3623	116.0717	143°	232.5
22	08:03:15	28.3515	116.0001	143°	232.5
			…		

Table 3: Event lateral conflict model parameter setting table based on TSRRT.

Parameters	Numbers	Parameters	Numbers
u (m·s^{-1})	514	D_1 (m)	37.60
v (m·s^{-1})	6.44	D_2 (m)	39.47
w (m·s^{-1})	0.78	λ_{z1} (m)	11.80
d (km)	10	λ_{z2} (m)	12.57
$P_x(0)$	0.0432	$P_y(0)$	0.0432
$P_z(S_z)$	6.6×10^{-6}	$E(0)$	0.01
τ (min)	4	W (km)	10
P_{goal}	0.1	$k_{\max}$	0.05
γ	0.4 pi		

Table 4: Collision risk assessment results.

Collision combination types	The original cylinder event model	Improved event model based on TSRRT	Safety target level
Combination 1 (A320)	1.12×10^{-10}	7.48×10^{-10}	5×10^{-9}
Combination 2 (B738)	1.12×10^{-10}	7.43×10^{-10}	5×10^{-9}

more than the 5.0×10^{-9}), which cannot meet the given safety target level of ICAO. The requirements can be met only by shortening the flight time or increasing the time interval. As shown in Figure 7, the number of collisions under different navigation specifications increases when the speed error parameter value σ changes. When $\sigma = 2$, the number of collisions of RNP4, RNP5, and RNP10 are −27.1, −22.0, and −11.6, respectively. Under the same speed error σ, RNP10 safety factor > RNP5 safety factor > RNP4 safety factor, and as the speed error parameter value increases, the collision risk changes decrease.

5.2. Improved Model Checking. When the Kalman filter is used to test the yaw probability model, the sampling period

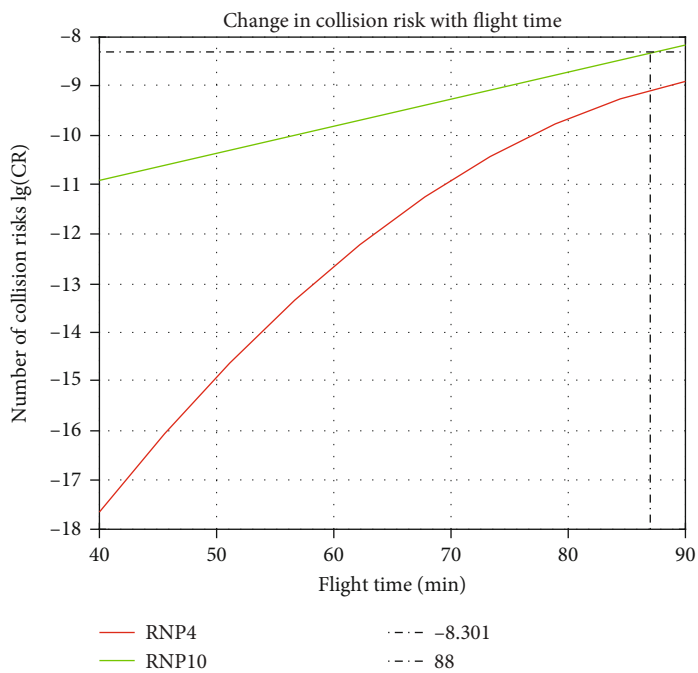

Figure 6: Collision risk changes with the flight time.

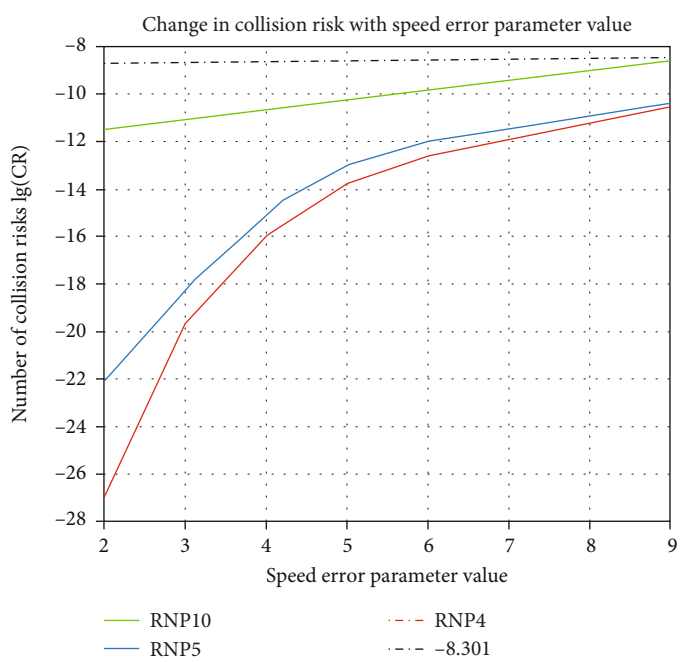

Figure 7: Collision risk changes with navigation speed error.

is controlled within the interval of $35 \pm 5S$ and the observed noise value $R(n) = 0.01 \times I_{4\times4}$, $Q(n) = I_{1\times1}$, $P(0 \mid 0) = 8 \times I_{6\times6}$, the system noise parameter is $B(n|n\text{-}1) = 0.01 \times I_{6\times1}$, with equations (12)–(15), and the corresponding motion filter is shown in Figures 8 and 9,

According to the requirements of ICAO.DOC4444《air traffic management》 [31], the width of the route is 20 km, with 10 km on both sides of the centerline. When conditions restrict a specific route section, the width can be reduced but it should not be less than 8 km. The maximum distance of ADS-B pulse yaw in Figure 8 is 10 km, and the minimum is 4 km, so it can well meet the navigation requirements of ICAO. At the same time, the curve clusters are analyzed. The comparison of $P(n \mid n)$ of the central mainline to the right benchmark mainly fluctuates in the range of [−10,0], and the $P(n \mid n)$ comparison benchmarks of a small part of

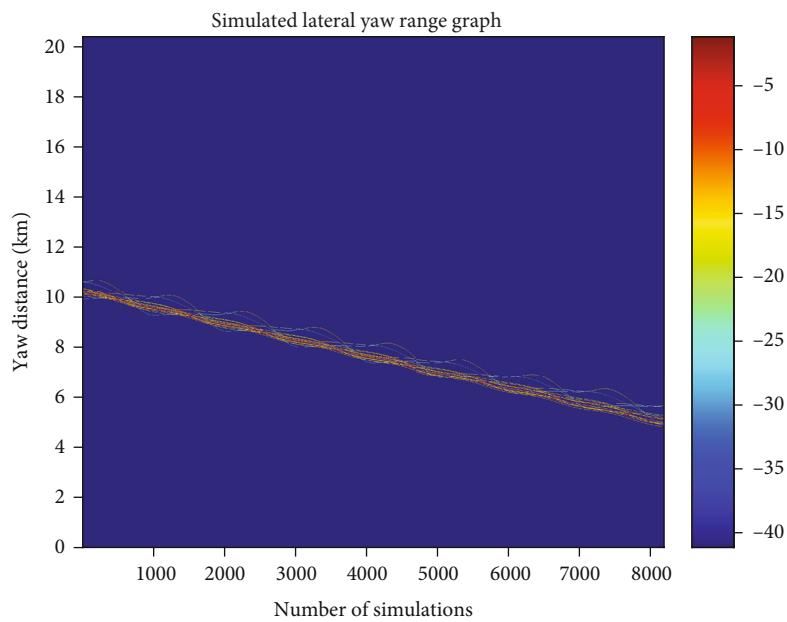

Figure 8: The simulated yaw curve under the ADS-B pulse pair.

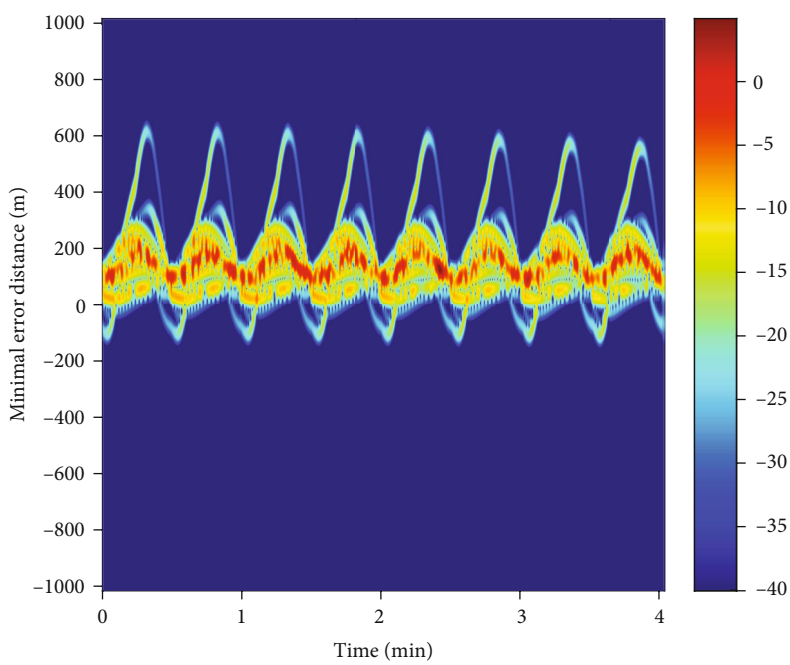

Figure 9: Research on track smoothness based on the Kalman filter.

the edge curves are mainly in [−30, −25] (unit: m) range. It can also meet the requirements for CNS in ICAO Annex 6 [28]. At the same time, the aircraft lateral slip analysis is performed on the filtering of Figure 9. The minimum error distance mainly fluctuates in the interval of [200,300] (unit: m). Because the general route width is ±20 km, the relative route slip ratio during the sailing time is 0.01. The RNP is selected as the flight navigation specification in the air route. The required coefficient of the sideslip time is ≤0.05, and the minimum sideslip coefficient of the RNP is 0.05. The filter sideslip rate of Figure 9 is much less than 0.05. The test shows that the event lateral conflict model based on TSRRT is effective and reasonable. It can meet the needs of TBO (trajectory-based operation).

$$f(x) \sim N\left(\mu(x), k\left(x, x'\right)\right), \tag{16}$$

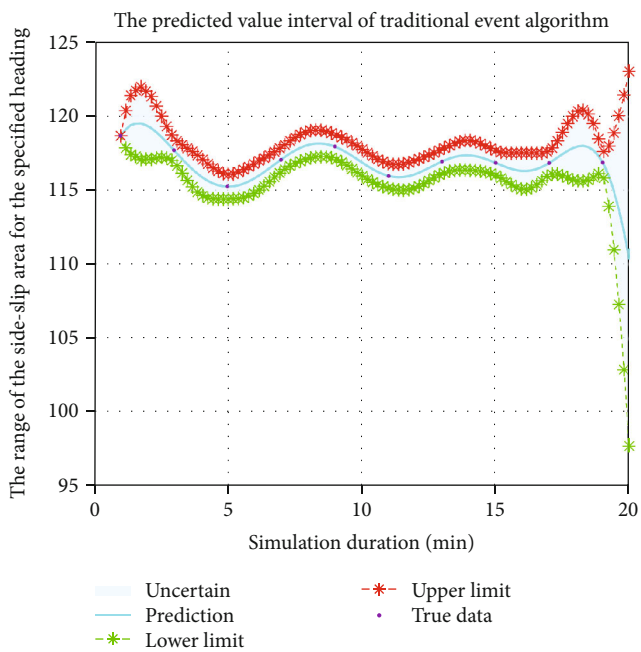

Figure 10: Prediction points and prediction intervals based on the traditional event model.

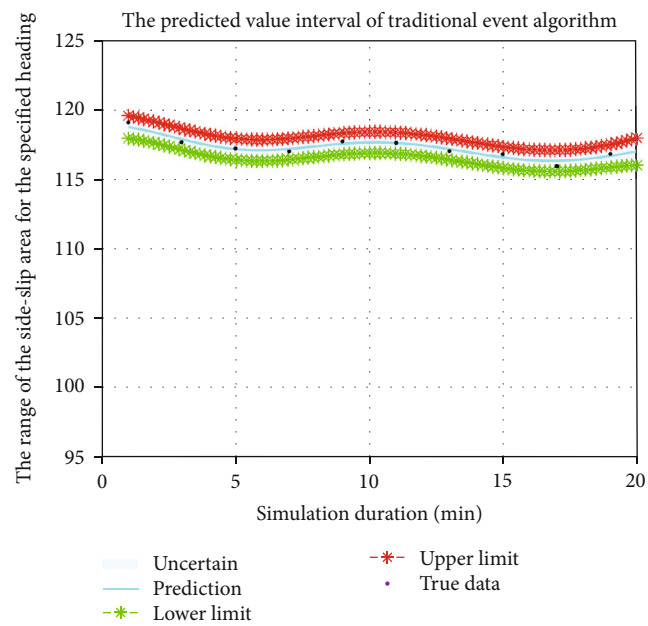

Figure 11: Forecast points and forecast intervals based on the improved event model.

$$k\left(x, x'\right) = \theta_0^2 \exp\left(-\frac{\left(x - x'\right)^2}{2\theta_1^2}\right) + \sigma^2 \delta_{ij}, \tag{17}$$

where $\mu(x)$ is the mean function; $k(x, x')$ is the covariance function; δ_{ij} is the Dirac function; when $i = j$, $\delta_{ij} = 1$; otherwise, it is 0.

At the same time, because the Kalman filter is based on the state equation and motion vector equation of the moving aircraft, the minimum mean square error is used as the basis to estimate the system state [24]. Gaussian process regression (GPR) includes the noise variance test and Gaussian process prior. The maximum likelihood function in the Gaussian process regression is selected as the test standard. The lateral offset margin can be estimated while predicting the accurate point of the route to provide higher safety and reliability for future free navigation. Putting the parameters in Table 3 into formula (17) ($\theta_0 = \theta_1 = 0.3$), the predicted values and intervals of its traditional event model and skid-slip event model can be obtained, as shown in Figures 10 and 11.

As shown in Figure 10, in the traditional event model, the upper limit of the interval is 122° and the lower limit of the interval is 115°; that is, the prediction interval is [115°,122°], the maximum difference of the prediction interval is 7°, and the interval boundary is volatile. It is not convenient for maneuvering in the main and auxiliary sections of the RNP route. In the improved event model of Figure 11, the upper limit of the interval is 119° and the lower limit of the interval is 116°; that is, the prediction interval is [116°,119°] and the maximum difference is 3°, compared with before the improvement, the sideslip angle is reduced by 4°. In addition, the interval boundary line is relatively smooth, which is more in line with RNP route specifications and operation well.

6. Conclusion

This paper selects the event lateral conflict resolution model based on TSRRT and takes the combination of A320 aircraft and B737-800 aircraft as the experimental subject. The calculation shows that the side collision probability of the improved event model is 15% of the collision probability of the traditional event model and the dynamic sideslip curvature error per unit time is reduced by 80%, indicating that the improved event model is effective and reasonable.

Through the analysis of the flight time change parameters and speed error parameter values in the event model, the collision risk increases with the parameter value. The collision risk decreases with the RNP error change within a given time, and it will be free to sail in the future. The performance of the CNS system can be improved to shorten the flight time or appropriately increase the safety margin.

Because the Kalman filter can analyze errors and improve the prediction accuracy, this article uses ICAO.DOC4444 as a guide to calculate the data obtained by the ADS-B query response pulse using the Kalman filter to verify that the improved event model is efficient.

The research object of this paper is only studying the lateral conflict model to satisfy the 4D trajectory operation in ASBU (aviation system block upgrade). It can be studied from the longitudinal, vertical, and mixed directions in the future to obtain a more practical conflict resolution model.

Data Availability

The numerical simulation data used to support the findings of this study are included in the article.

Conflicts of Interest

The authors declare that they have no conflicts of interest.

Acknowledgments

This work was sponsored in part by the "Visual Flight Programming and Approval Guidelines Project of RNAV Procedures" (no. 14002600100015J013), "Special Guidance Found of Building World-Class Universities (Disciplines) and Characteristic Development" (no. D202103), and "Innovation and Entrepreneurship Training Program for College Students of Sichuan Province" (no. 202210624005).We are grateful for the support of these funds.

References

[1] Q. Yuling, *Research on Air Traffic Collision Risk Models*, Nanjing University of Aeronautics and Astronautics, Nanjing, 2012.

[2] P. Reich, "Analysis of long-range air traffic systems: separation standards—III," *Journal of Navigation*, vol. 19, no. 3, pp. 331–347, 1966.

[3] P. Brooker, "Aircraft collision risk in the North Atlantic region," *Journal of the Operational Research Society*, vol. 35, no. 8, pp. 695–703, 1984.

[4] T. Brewer-Dougherty, B. Colamosca, C. Gerhardt-Falk et al., "Collision risk modeling in the Northern Pacific airspace under separation reduction and improvements in navigational performance," *Air Traffic Control Quarterly*, vol. 14, no. 4, pp. 257–282, 2006.

[5] K. Kim and I. Hwang, "Intent-based detection and characterization of aircraft maneuvers in en route airspace," *Journal of Aerospace Information Systems*, vol. 15, no. 2, pp. 72–91, 2018.

[6] P. Brooker, "Lateral collision risk in air traffic track systems: a 'post-Reich' event model," *Journal of Navigation*, vol. 56, no. 3, pp. 399–409, 2003.

[7] X. Xiaohao, W. Zhenyu, and Z. Hongsheng, "Event-based side collision risk improvement model," *Journal of the Civil Aviation University of China*, vol. 3, pp. 1–4, 2008.

[8] Y. Wenjun, L. Tingting, and L. Jimin, "Research on the safety assessment of cross-airway flights interval," *Aeronautical Computing Technology*, vol. 40, no. 1, pp. 11–15, 2010.

[9] Q. Yuling, H. Songchen, and Z. Ming, "Collision risk model of turning airway," *Transportation Engineering*, vol. 11, no. 3, pp. 88–92, 2011.

[10] L. Zongping, L. Yanfei, and Z. Zhaoning, "Research on collision risk for paired approach based on fault tree analysis method," *Science Technology and Industry*, vol. 13, no. 4, pp. 130–134, 2013.

[11] C. Xingwu and Z. Zhaoning, "Cross route collision risk assessment based on event improved model," *Journal of China Civil Aviation University*, vol. 33, no. 3, pp. 1–4, 2015.

[12] W. Jian, *Study on the Risk of Paired Approach Collision in Close Parallel Runway*, Civil Aviation University of China, Tianjin, 2017.

[13] Y. Xinsheng and R. Zhi, "Study on flight interval assessment and conflict resolution threshold under the influence of multiple random factors," *Journal of Safety and Environment*, vol. 18, no. 1, pp. 1–4, 2018.

[14] Y. Shuo, *Research on the Modeling Method of Large-Scale UAV Collision Models*, Hebei University of Science and Technology, Shijiazhuang, 2019.

[15] C. Xie, X. Liang, and F. Lu, "Based on thestatistical distribution, the risk assessment of paired approach longitudinal collisions in close parallel runways," *Science Technology and Engineering.*, vol. 21, no. 10, pp. 4284–4288, 2021.

[16] D. A. Hsu, "The evaluation of aircraft collision probabilities at intersecting air routes," *Journal of Navigation*, vol. 34, no. 1, pp. 78–102, 1981.

[17] W. Pingan, "Risk prediction of collision between military aviation domain and civil aviation route in the lateral interval," *Firepower and Command Control*, vol. 44, no. 1, pp. 87–92, 2019.

[18] K. Yang and S. Sukkarieh, "An analytical continuous-curvature path-smoothing algorithm," *IEEE Transactions on Robotics*, vol. 26, no. 3, pp. 561–568, 2010.

[19] International Civil Aviation Organization (ICAO), *Doc9750-AN/963-2016-2030 Global Air Navigation Plan (FIFTH EDITION)*, ICAO, Montréal,Canada, 2016.

[20] L. Ma, Y. Tian, S. Yang, C. Xu, and A. Hao, "A scheme of sustainable trajectory optimization for aircraft cruise based on comprehensive social benefit," *Discrete Dynamics in Nature and Society*, vol. 2021, Article ID 7629203, 15 pages, 2021.

[21] Y. Zou, H. Zhang, G. Zhong, H. Liu, and D. Feng, "Collision probability estimation for small unmanned aircraft systems," *Reliability Engineering & System Safety*, vol. 213, p. 107619, 2021.

[22] Z. Daiwu and H. Guangqin, *Visual and Instrument Flight Program Designs*, Southwest Jiaotong University Press, Chengdu, 3rd edition, 2016.

[23] International Civil Aviation Organization (ICAO), *Doc 8168-OPS/611-Volume II Procedure for Air Navigation Services-Aircraft Operation (Volume II)Construction of Visual and Instrumental Flight Procedures (Sixth Edition)*, ICAO, Montréal, Canada, 2014.

[24] Z. Shuibing, T. Cheng, L. Shan, and W. Dejun, "Ship trajectory prediction based on improved Kalman filter in the controlled river," *Computer Applications*, vol. 32, no. 11, pp. 3247–3250, 2012.

[25] Y. Yang, Z. Suqin, and D. Guilan, "Integrated navigation technology based on federated Kalman filtering on the Beidou double star positioning system," *Computer Science*, vol. 3, pp. 110–113, 2007.

[26] Z. Zhaoning, W. Lili, and L. Dongbin, *Introduction to Flight Separation Safety Assessment*, Science Press, Beijing, 2009.

[27] Z. Xiaoyan and P. Weijun, "Safety assessment of vertical separation in RVSM airspace," *Aeronautical Computing Technology*, vol. 39, no. 5, pp. 5–8, 2009.

[28] K. I. Tenekedjiev, N. D. Nikolova, and K. Kolev, "Applications of Monte Carlo simulation in modelling of biochemical processes," in *Applications of Monte Carlo Methods in Biology, Medicine and Other Fields of Science*, C. J. Mode, Ed., InTech, Rijeka (HR), 2011, Chapter 4.

[29] G. Moek, E. Lutz, and W. Mosborg, *Risk Assessment of RNP1 and RVSM in the Southern Atlantic Flight Identification Regions,20833*, ARINC, Annapolis, 2001.

[30] International Civil Aviation Organization (ICAO), *International Standards and Recommended Practices, Annex 6, Operation of Aircraft (Tenth Edition)*, ICAO, Montréal, Canada, 2018.

[31] Convention on International Civil Aviation, *Doc 4444:Air Traffic Management*, Montréal INTERNATIONAL CIVIL AVIATION ORGANIZATION (ICAO), Montreal, 2016.

Hindawi
International Journal of Aerospace Engineering
Volume 2022, Article ID 8004478, 17 pages
https://doi.org/10.1155/2022/8004478

Research Article

Real-Time Trajectory Planning and Control for Constrained UAV Based on Differential Flatness

Dongli Wu,[1] **Hao Zhang**,[2] **Yunping Liu**,[2] **Weihua Fang**,[3] **and Yan Wang**[2]

[1]*CMA Meteorological Observation Center, Beijing 100081, China*
[2]*Jiangsu Collaborative Innovation Center of Atmospheric Environment and Equipment Technology (CICAEET), Nanjing University of Information Science & Technology, Nanjing 210044, China*
[3]*Nanjing Institute of Hydraulic and Hydrology Automation, Ministry of Water Resources, China*

Correspondence should be addressed to Dongli Wu; wudongli666@126.com and Yunping Liu; liuyunping@nuist.edu.cn

Received 7 January 2022; Revised 22 March 2022; Accepted 11 May 2022; Published 20 June 2022

Academic Editor: Hao Wen

The trajectory planning of UAV with nonholonomic constraints is usually taken as differential algebraic equation to solve the optimal control problem of functional extremum under the condition of inequality constraints. However, it can be challenging to meet the requirements of real-time for the high complexity. A differential flat theory based on B-spline trajectory planning can replace the optimal control problem with nonlinear programming and be a good means to achieve the efficient trajectory planning of an UAV under multiple dynamic constraints. This research verifies the feasibility of this theory with actual flight experiments.

1. Introduction

Unmanned aerial vehicles (UAV) [1] have been widely used [2] in challenging operations due to its advantageous features such as strong maneuverability, small size, autonomous flight, and accurate positioning, which turned them into a promising tool in modern military and civilian scenarios [3]. With the continuous development of vision, the combination of the two technologies [4] also has broad prospects, and the closest contact between both fields is the track planning of a UAV [5]. The autonomous flight design of a UAV ultimately depends on its flight path planning [6]. The current planning problems are mainly divided into motion planning and trajectory planning. Among them, the latter refers to the implementation of point-to-point routes in a known environment. Trajectory planning usually combines the dynamic model [7] with the motion planning to solve the overall optimal control issue of the moving body, which leads to other problems, e.g., high complexity, complicated operation, and low computational efficiency, greatly increasing the difficulty of its application [8]. At present, the track planning algorithms are mainly divided into four categories: (i) the schematic method consisting of the general view method, the Voronoi diagram method, and the contour method [9–11]; (ii) the unit decomposition plan composed of the grid and the quadtree method [12]; (iii) the artificial potential field method consisting of the wave propagation method and the harmonic function method [13, 14]; (iv) the heuristic planning method based on the genetic algorithm and the neural network algorithm [15–17]. The above algorithms all consider the trajectory planning issues with various constraints and verify the feasibility of the methods through simulation. However, they are only suitable for experiments, but their practical feasibility has not been taken into consideration yet. In addition, UAVs also involve related control algorithms. The addition of the above planning algorithms will expand the scale of the problem, significantly increase the time needed, and reduce the planning efficiency, which goes in the opposite direction of the actual application requirements.

The differential flatness method can transform many classical nonlinear systems into flat systems for research, such as robot controlling and planning problems and tracking control problems [18] with nonholonomic

constraints [19]. In reference [20], the theory is applied to the trajectory planning of vehicle-like robots with nonholonomic constraints and compared with the planning method of the opportunity polynomial input. Similarly, reference [21] adopted the theory to design robot controllers in a dynamic environment. Reference [22] proposed the real-time trajectory generation based on differential flatness systems, satisfying state equations, paths, and actuator constraints.

With the development of control algorithms and image processing algorithms, the problem of UAV capturing and trajectory planning has received extensive attention in recent years. Ghadiok et al. built a slam map based on an infrared camera, but it was characterized by a lengthy process [23]. Spica et al. verified the feasibility of an UAV capturing moving objects with the features of the differential flatness theory [24]. Thomas et al. used the motion capture system to achieve visual-based capture with reference to the birds capture behavior, but the price of the motion capture system was too high for practical use [25]. Arputha and Dutta proposed a method for collaborative trajectory planning for multiple UAVs and conducted motion planning on the convex surface by building connections among them [26]. Zhang et al. adopted the ant colony algorithm to accurately estimate the heading angle deviation of a UAV [27]. Penin et al. proposed a minimum time trajectory planning method, using receding horizon control (RHC) to modify the reference trajectory online [28]. Although the above method proposes a path planning method suitable for UAVs, most of them cannot be applied to actual flight control, and many studies lack verification methods based on actual flight experiments. Some of them have achieved the goal of path planning, but with expensive techniques that cannot meet the actual application of promotion.

Aiming at the problems of high planning complexity and poor real-time performance, this study focuses on a UAV equipped with robot arms while taking into consideration the possible constraints of the flight. The first step is to establish the dynamic model of the most suitable system for this UAV, with its position and attitude being used as the flat output. The feasibility of the trajectory planning was proved by verifying the differential flatness theory, and its trajectory was smoothed by the B-spline [29]. We proposed the design of a controller combining the sliding mode and the PID control and verified the feasibility of the abovementioned schemes with proper experiments. Compared with the traditional UAV trajectory planning issue, our method reduces the complexity of planning under the premise of ensuring stability and is more suitable for practical embedded systems. Furthermore, it provides guarantee for high-precision planning actions such as drone capture.

2. Dynamic Model and Controller

2.1. Dynamic Model. Figure 1 illustrates a simplified model image of the UAV. In this paper, the three coordinate systems below are established——earth coordinate system $E-XYZ$, quadrotor carrier coordinate system $B-xyz$, and robot arm coordinate system $A-ax, az$. It is also assumed that the robot arm can only rotate around the center in the plane $ax-az$. $\varphi, \theta, \psi, \alpha$ represent the roll angle, pitch angle, attitude angle of the UAV, and the tilt angle of the arm from the axis az, respectively. B represents the centroid position of the quadrotor, and $F_i(i=1,2,3,4)$ provides the lift for the rotor. The detailed description of the symbols used in this paper is organized in Symbols.

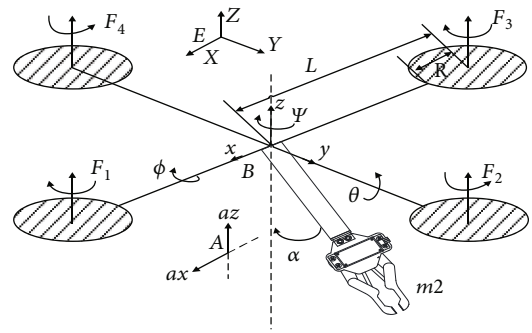

Figure 1: System structure diagram.

The generalized coordinate vector $q=(\phi,\theta,\psi,x,y,z,\alpha)^T$ and the pseudovelocity vector $p=(\rho,q,r,u,v,w,b)^T$ are defined as outlined above. The pseudovelocity is a multibody system domain that relies on the generalized coordinate to describe the velocity of motion. Here, the velocity vector of the quadrotor in the body coordinate $B-xyz$ system is defined. The spatial position of the system (including the three corners and the displacement along the coordinates) is described by q. p defines the number of velocities of the system (including the three angular velocities and the displacement velocity along the coordinates). The dynamic model of the system is established by the Euler-Ponkale equation as follows:

$$\begin{cases} \dot{q}=V(q)p, \\ M(q)\dot{p}+C(q,p)p+F(p,q,u)=0. \end{cases} \tag{1}$$

Vector $\eta=(\varphi,\theta,\psi)^T$ represents the attitude of the flight system, and vector $X=(x,y,z)^T$ refers to the position of the system centroid in the Earth's coordinate system. $V(q)$ indicates the angular velocity at which the arm rotates, and ω represents the system's pseudovelocity and the generalized velocity attitude transformation matrix. $F(p,q,u)$ represents the sum of aerodynamics, gravity, and control inputs; u is the total system control input; and $M(q)$ is the inertial matrix of the system. $C(p,q)$ describes the gyro matrix of the system and can be defined in a simplified manner as $S_\phi=\sin\phi$, $S_\theta=\sin\theta$, $S_\alpha=\sin\alpha$, $C_\theta=\cos\theta$, $S_\psi=\sin\psi$, $C_\psi=\cos\psi$, and $C_\alpha=\cos\alpha$. The result of the final calculation is

$$F(p,q,u)=\begin{bmatrix} -LU_2+gm_2RC_\alpha C_\theta S_\Phi \\ -LU_3+gm_2R(C_\theta C_\Phi S_\alpha+C_\alpha S_\theta) \\ -LU_4-gm_2RC_\theta S_\alpha S_\theta \\ -g(m_1+m_2)S_\theta \\ g(m_1+m_2)C_\theta S_\phi \\ -U_1+g(m_1+m_2)C_\theta C_\phi \\ -T+gm_2R\left(C_\theta C_\phi S_\alpha+C_\alpha S_\theta\right) \end{bmatrix}. \tag{2}$$

$$M(q)=\begin{bmatrix} I_x+m_2R^2{C_\alpha}^2 & 0 & -m_2R^2C_\alpha S_\alpha & 0 & m_2RC_\alpha & 0 & 0 \\ 0 & I_y+J_y+m_2R^2 & 0 & -m_2RC_\alpha & 0 & m_2RS_\alpha & J_y+m_2R^2 \\ -m_2R^2C_\alpha S_\alpha & 0 & I_z+m_2R^2{S_\alpha}^2 & 0 & m_2RS_\alpha & 0 & 0 \\ 0 & -m_2RC_\alpha & 0 & m_1+m_2 & 0 & 0 & -m_2RC_\alpha \\ m_2RC_\alpha & 0 & -m_2RS_\alpha & 0 & m_1+m_2 & 0 & 0 \\ 0 & m_2RS_\alpha & 0 & 0 & 0 & m_1+m_2 & m_2RS_\alpha \\ 0 & J_y+m_2R^2 & 0 & -m_2RC_\alpha & 0 & m_2RS_\alpha & J_y+m_2R^2 \end{bmatrix}. \tag{3}$$

Among them, the control variables of lifting, rolling, pitching, and yaw are U_1, U_2, U_3, and U_4, respectively. T is the control variable of the tilt angle of the arm, and $F_i(i=1,2,3,4)$ is the pulling force of each rotor. The area of the rotor is represented by $A=\pi R^2$, and the coefficient is $K=C_Q/C_T$, then

$$\left\{\begin{array}{c} U_1=F_1+F_2+F_3+F_4 \\ U_2=F_2-F_4 \\ U_3=F_1-F_3 \\ U_4=K(F_1-F_2+F_3-F_4) \\ F=\dfrac{1}{2}\rho AC_TR^2\Omega^2 \end{array}\right\}. \tag{4}$$

The total control input $u=[U_1,U_2,U_3,U_4,T]^T$ is set for the system, and when it experiences low air resistance at low speeds, the force can be ignored. If we assume that ϕ and θ in the flight process are considerably small, and its rate of change is also sufficiently small, it can be substituted into Equation (1) for simplification:

$$\begin{bmatrix} \dot\phi \\ \dot\theta \\ \dot\varphi \end{bmatrix}=\begin{bmatrix} 1 & 0 & 0 \\ 0 & 1 & 0 \\ 0 & 0 & 1 \end{bmatrix}\begin{bmatrix} p \\ q \\ r \end{bmatrix}. \tag{5}$$

The kinetic model of the system is simplified by Equation (5), and the formulas available are

$$\left\{\begin{array}{l} \ddot\phi=\dfrac{2LI_z(m_1+m_2)+m_1m_2R^2(-LU_2C_{2\alpha}+LU_4S_{2\alpha})}{A_5}, \\ \ddot\theta=\dfrac{-T+LU_3}{I_y}, \\ \ddot\psi=\dfrac{L\left\{2I_x(m_1+m_2)+m_1m_2R^2\right\}U_4+m_1m_2R^2(LR_4C_{2\alpha}+U_2S_{2\alpha})}{A_5}, \\ \ddot x=\dfrac{4m_2(m_1+m_2)RTC_\alpha-2m_2R\left\{2b^2J_y(m_1+m_2)+2b^2m_1m_2R^2+2m_2RU_1C_\alpha\right\}S_\alpha+A_4*gS_\theta}{A_4}, \\ \ddot y=\dfrac{-2I_zLm_2RU_2C_\alpha+2I_xLm_2RU_4S_\alpha-g\left[2I_xI_z(m_1+m_2)+(I_x+I_z)m_1m_2R^2\right]C_\theta S_\phi+g(I_x-I_z)m_1m_2R^2C_{2\alpha}C_\theta S_\phi}{A_5}, \\ \ddot z=\dfrac{A_1+A_2*U_1-A_3*T}{A_4}, \\ \ddot\alpha=\dfrac{\left[(I_y+J_y)(m_1+m_2)+m_1m_2R^2\right]T-L\left\{J_y(m_1+m_2)+m_1m_2R^2\right\}U_3-I_ym_2RU_1S_\alpha}{I_yJ_y(m_1+m_2)+I_ym_1m_2R^2}. \end{array}\right. \tag{6}$$

The above letters are defined as follows:

$$\begin{cases} A_1 = -4g(m_1+m_2)\left[J_y(m_1+m_2)+m_1m_2R^2\right]C_\theta C_\varphi - m_2R\left[4\dot{\alpha}^2J_y(m_1+m_2)+4\dot{\alpha}^2m_1m_2R^2\right]C_\alpha, \\ A_2 = 2\left[2J_y(m_1+m_2)+m_2R^2(2m_1+m_2)\right]-2m_2^2R^2C_{2\alpha}, \\ A_3 = 4m_2(m_1+m_2)RS_\alpha, \\ A_4 = 4(m_1+m_2)\left[J_y(m_1+m_2)+m_1m_2R^2\right], \\ A_5 = 2I_xI_y(m_1+m_2)+2m_1m_2R^2\left(I_zC_\alpha{}^2+I_xS_\alpha{}^2\right). \end{cases} \tag{7}$$

2.2. Controller Design. Our research adopts the differential trajectory planning method based on differential flatness and the sliding mode PID control (combined control of sliding mode control and traditional PID control) [30] to enhance the anti-interference ability and response speed of the system [31]. This methodology was designed based on the control requirements of the UAV. The methods can be applied to the actual control, and the shortest sampling period of the clock is set to 0.02 s, that is, the position of the next desired point of the UAV is determined every 0.02 s. Once the control requirements are implemented, the specific control flow is represented in Figure 2.

The position control of the quadrotor can be divided into horizontal position and height control. Since the system uses four inputs to control six degrees of freedom, it is considered an underactuated and strongly coupled nonlinear system. The system is then decomposed into full a drive module and an underdrive module for easy analysis. We have established the mathematical relationship between the attitude angle, the position, and height control U_1 to achieve the purpose of trajectory tracking by continuously adjusting the attitude angle and the height. Both the horizontal position and the pull-down tilt angle are controlled using PID. The relationship between the desired position $(x_d y_d)$ and the desired acceleration $(\ddot{x}_d \ddot{y}_d)$, the desired tilt angle α_d, the angular acceleration of the robot arm $\ddot{\alpha}$, and the control rates of x, t, T are designed as follows:

$$\begin{cases} \ddot{x}_d = k_{p1}(x_d - x) + k_{i_1}\int(x_d - x) + k_{d_1}(\dot{x}_d - \dot{x})d_x, \\ \ddot{y}_d = k_{p2}(y_d - y) + k_{i_2}\int(y_d - y) + k_{d_2}(\dot{y}_d - \dot{y})d_y, \\ \ddot{\alpha}_d = k_{p3}(\alpha_d - \alpha) + k_{i_3}\int(\alpha_d - \alpha) + k_{d_3}(\dot{\alpha}_d - \dot{\alpha})d_\alpha. \end{cases} \tag{8}$$

The height control and attitude angle control are proposed using the sliding mode PID algorithm. The design of the sliding mode PID controller includes the selection of sliding mode surface and control law design. The surface is generally selected as $s = 0$, and the control objective of the sliding mode PID is designed to make the surface function finally stable, achieving a stable control. Taking the height as an example of control, Z_d, Z indicates the desired and actual height, and two errors are calculated as

$$e_z = Z_d - Z. \tag{9}$$

Then, the next step is to design the sliding surface function:

$$S_z = \dot{e}_z + d_1 * e_z + c_1 * \int e_z d_t. \tag{10}$$

To ensure that the system can quickly converge to the sliding mode for large values of S. After that, the exponential convergence law rate is chosen to derive U_1:

$$\dot{S}_z = -\varepsilon \operatorname{sgn}(S_z) - kS_z. \tag{11}$$

In the above formula, ε takes the value 0.01, k takes the value 3, and sgn (s) denotes the sign function. The Lyapunov function is used to determine the stability of the system, and its positive definite function is designed as follows:

$$V_z = \frac{1}{2}S_z{}^2. \tag{12}$$

Then, its derivative along the track line is

$$\dot{V}_z = S_z\dot{S}_z = S_z[-\varepsilon \operatorname{sgn}(S_z) - kS_z] = -\varepsilon\|S_z\| - k\|S_z\|^2 \le 0. \tag{13}$$

Therefore, the kinetic model satisfies the stability criterion of Lyapunov asymptotic stability and is considered an asymptotically stable system, i.e., the error function will slowly converge to 0 over time and can eventually arrive at the sliding mode.

A combination of sliding mode control and PID control is adopted to enhance the anti-jamming and fast response characteristics of the UAV. By combining the control laws of both modes, the sliding mode PID control in this section is obtained, and the stability and robustness of the quadrotor control can be greatly improved by combining the advantages of each control. The position control of the quadrotor can be divided into horizontal position and altitude control.

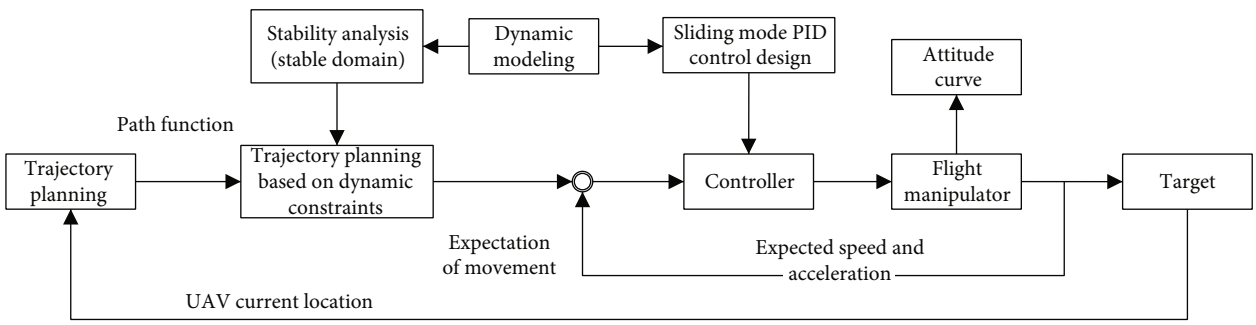

Figure 2: Control process.

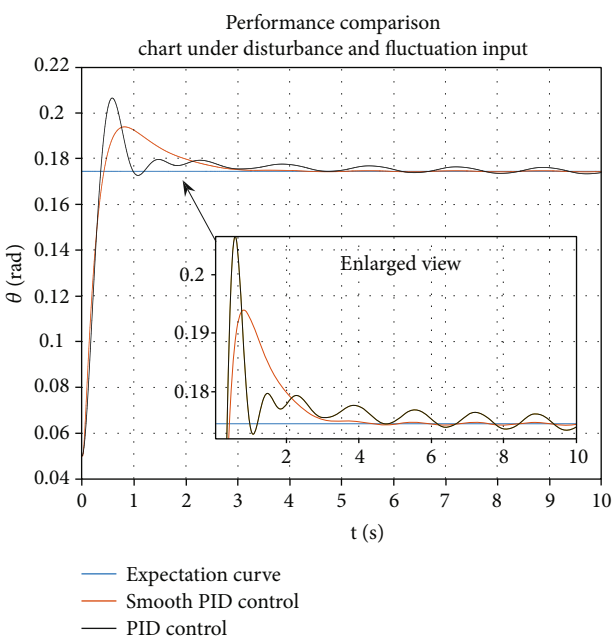

Figure 3: Performance comparisons under disturbance and fluctuation control inputs.

Since the system uses four inputs to control six degrees of freedom, it is an under-driven, strongly coupled nonlinear system. It is necessary to establish the mathematical relationship between attitude angle and position and height control quantities to achieve the purpose of trajectory tracking by continuously adjusting both.

Furthermore, to test the performance of the sliding mode PID controller, we first enable the two controls to quickly reach a steady state and stay under a stable input and without disturbance. Then, the control input is converted into a sinusoidal wave input, and complex disturbances are added to it. This process shows that significant control differences exist in traditional PID. It was proved that the sliding mode PID control has strong anti-interference and fast response capability, and Figure 3 is the result of a comparison between the two controllers under disturbance and fluctuation control inputs.

2.3. Robotic Arm Design. The design of the UAVs robot arm contains three servos. Their rotation direction is around the y-axis forward and backward and around the height direction of the z-axis rotation, and the last servo is responsible for clamping. The control of the robot arm is done through manual grasping, that is, by receiving commands from the remote control to achieve grasping. This means that when the UAV can be moved to the target area by manually controlling the mechanical claw. Figure 4 shows the design of the experiment and the printed product made of ABS (acrylonitrile butadiene styrene plastic). The control of the robot arm is controlled by an MCU that generates PWM waves with a common frequency that ranges between 0.5 ms and 2.5 ms. The time difference between adjacent pulses is 2 ms. The width of the pulse varies by changing its duty cycle to achieve various angular rotations of the servo, and its operating voltage is usually 5 V.

3. Trajectory Planning

UAV trajectory planning with constraints is generally used as an optimal control problem for solving the generalized polar values of differential algebraic equations under inequality constraints. The direct solutions of these equations are normally challenging and inefficient, and their stability is difficult to analyze. To address these issues, this chapter introduces the differential flatness theory based on B-sample trajectory planning to transform the optimal control problem into nonlinear planning. If the solution is successful, we can achieve convenient and real-time planning of the UAV's trajectory under kinetic constraints, e.g., position, velocity, and acceleration.

3.1. Differential Flatness Applied to Trajectory Planning. The definition of differential flatness for nonlinear systems relies on the idea that if the spatial state quantities and control input variables of a system can be expressed using finite order differentials of the system output, then, the nonlinear system with the above characteristics has differential flatness properties.

If we define a nonlinear system $\dot{x} = f(x, u), x \in R^n, u \in R^m$ with input u of the system without feedback and define the flat output as $y = h(x, u, \dot{u}, \cdots, u^{(r)})$, the trajectory function $(x(t), u(t))$ can be set to be an equation with respect to the flat output y and its differential $x = \phi(y, \dot{y}, \cdots, y^{(q)}), u = \alpha(y, y, \cdots, y^{(q)})$. The trajectory planning problem contains a starting

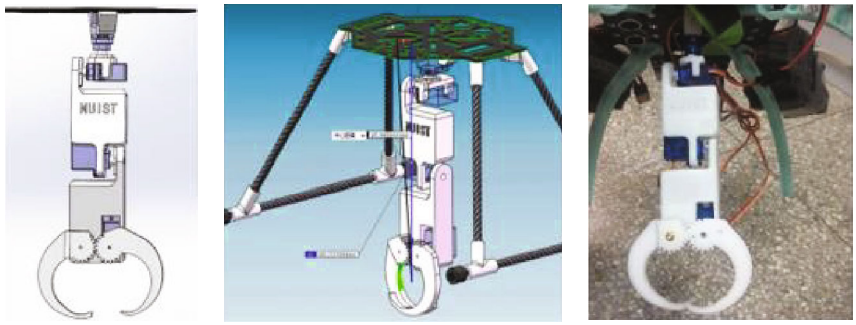

(a) (b) (c)

Figure 4: UAV robot arm design. (a) Design drawings. (b) Installation schematic. (c) Physical picture.

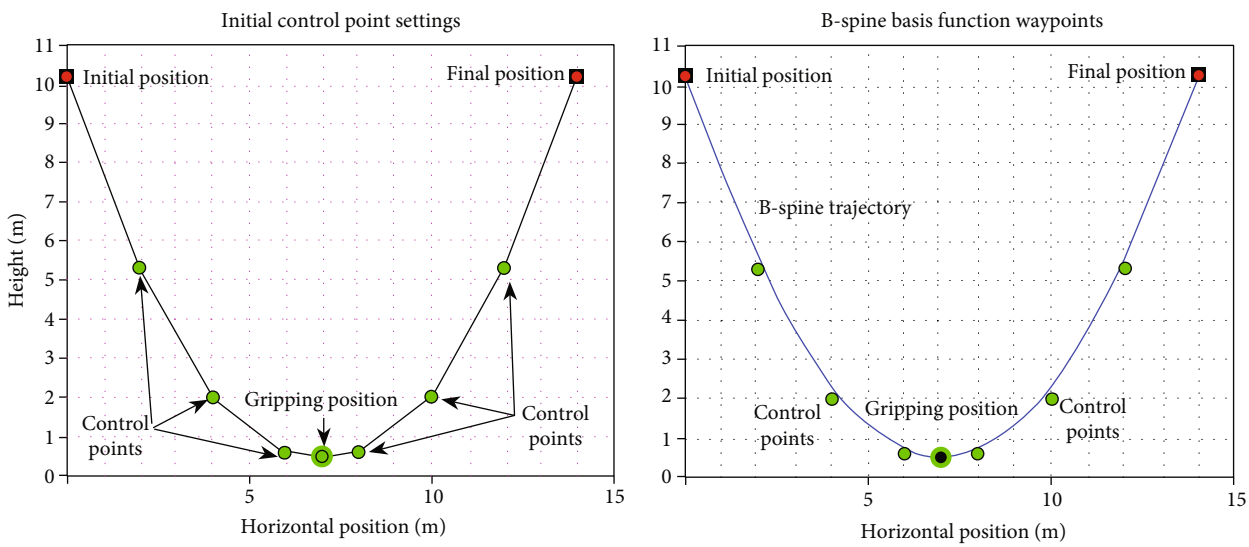

(a) (b)

Figure 5: Location of the initial control node. (a) Initial control points choice. (b) B-spline basis function waypoints.

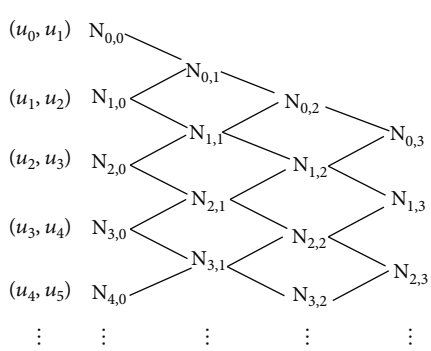

Figure 6: B-spline basis function subnode calculation.

state and an arrival state, and the flat output of the system is assumed to be a vector containing y_i, so

$$y_i = \sum_j A_{ij}\lambda_j(t), \tag{14}$$

where λ_j, $j = 1, 2, \cdots, N$ is a basis function, and the problem of defining the flat output element y_i is equivalent to finding its spatial prediction in the space composed of the basis functions λ_i. Assuming that the state quantity at the starting moment of the trajectory t_0 is x_0 and the state quantity at the termination moment of t_f is x_f, then, the coefficients A_{ij} should satisfy the following conditions:

$$\begin{aligned} y_i(t_0) &= \sum_j A_{ij}\lambda_i(t_0) & y_i(t_f) &= \sum_j A_{ij}\lambda_i(t_f) \\ &\cdots & &\cdots \\ y_i^{(q)}(t_0) &= \sum_j A_{ij}\lambda_j^{(q)}(t_0) & y_i^{q}(t_0) &= \sum_j A_{ij}\lambda_j^{(q)}(t_0) \end{aligned} \tag{15}$$

Provided that generality is guaranteed and assuming the dimension $i = 1$ of the planar output vector, $y = [y_1]$ (these

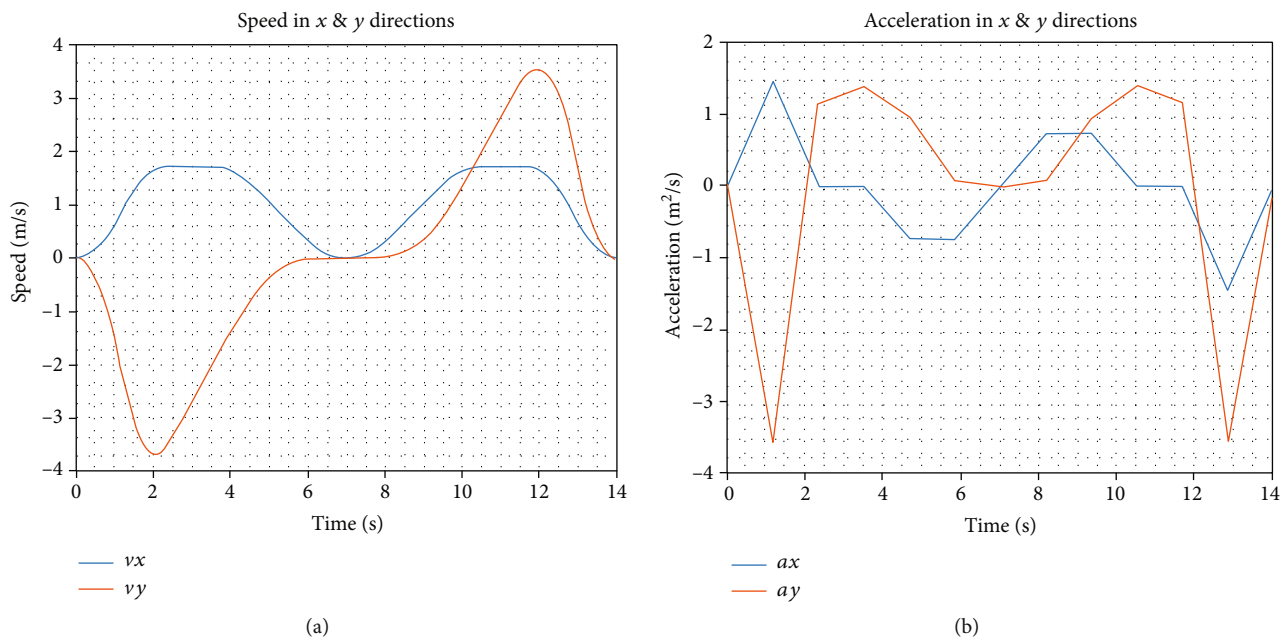

Figure 7: B-spline generated basis function path and speed curve. (a) Speed. (b) Acceleration.

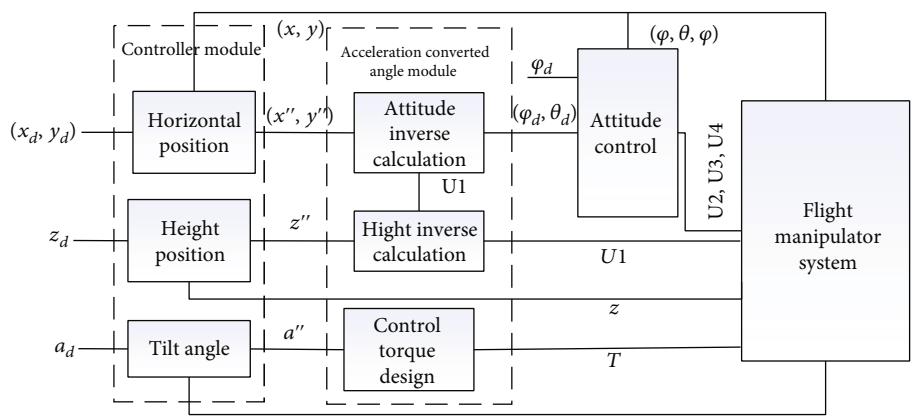

Figure 8: Control flow diagram.

results can also be generalized to the multidimensional case), the other variables are defined as follows:

$$\tilde{y}_0 = \left(y_1(\tau_0),\cdots,y_1^{(q)}(\tau_0)\right),$$
$$\tilde{y}_f = \left(y_1(\tau_f),\cdots,y_1^{(q)}(\tau_f)\right), \quad (16)$$
$$\tilde{y} = \left(\tilde{y}_0, \tilde{y}_f\right).$$

Combining equations A and B yields

$$y = \begin{pmatrix} \Lambda(\tau_0) \\ \Lambda(\tau_i) \end{pmatrix} A = \Lambda A, \quad (17)$$

where Λ is a full rank matrix, which means that the space equation λ_j must be an absolute full rank. This shows that the path planning problem for differential flat systems is feasible according to the linear algebraic theory.

3.2. The Cubic B-Spline Curve. The aim of trajectory planning is to achieve gripping. The first step is to set the initial position, gripping position, and final position. Second, a few control points are set for the UAV's obstacle avoidance paths, velocity, and acceleration constraints. Finally, cubic B spline smoothing was carried out on the track.

The cubic B-spline curve generates a path segment for each of the four control points, and then it splices each segment path to obtain a smooth global planning path. A series of smooth nodes can be obtained through the derivation of the finite control points. As shown in Figure 5(b), the plane coordinate system of the UAV's flight is established for convenient analysis, and the initial position of the vehicle is

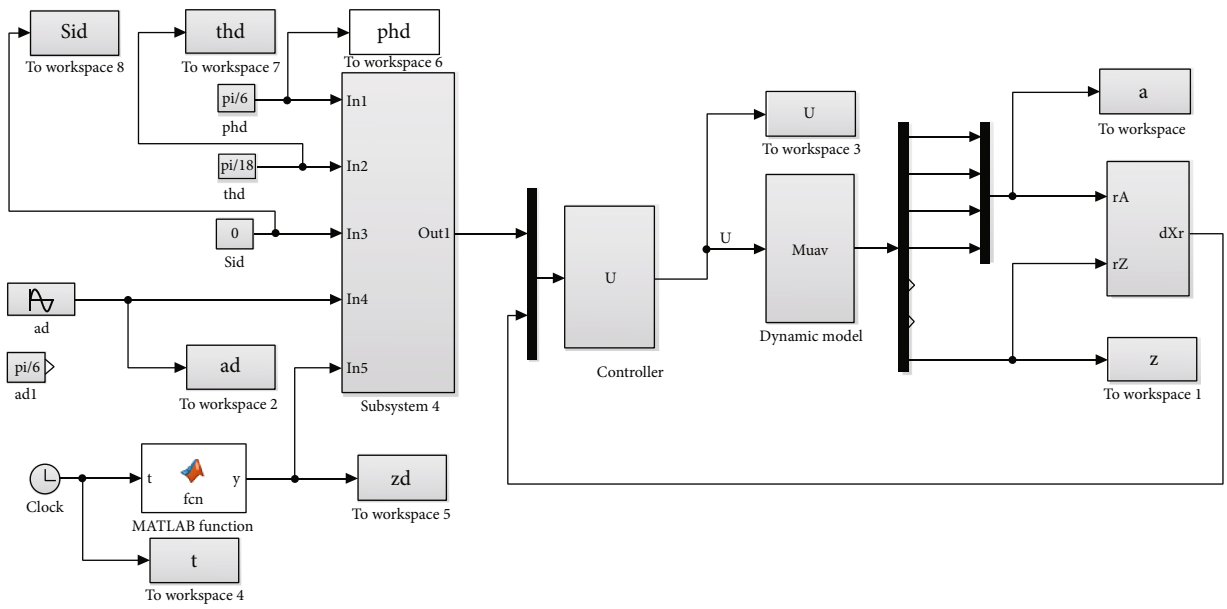

Figure 9: Simulation design of UAV with robotic arm.

assumed to be (0, 10), the gripping position (7, 0.5), and the final position (14, 10). According to the data obtained, the maximum descent speed of four-axis rotors is 4 m/s, the maximum rise speed is 10 m/s, and the maximum acceleration is 5 m/s^2. In addition, we set six control points to constrain the path selection, speed, and acceleration due to the presence of obstacles and other influences during flight. Equation (19) is the constraint condition of the UAV flight, (x_i, y_i). It indicates the coordinates of the UAV at time i, then sets the shortest path as its penalty function, d_i pointing out the distance from the obstacle. L represents the length of the UAV arm, and v_i and $\dot{v}_i$ represent the speed and acceleration of the vehicle.

$$\begin{cases} \min f(i) = \sum_{i-T}^{t} \sqrt{(x_i - x_{i-1})^2 + (y_i - y_{i-1})^2} \\ \text{s.t.} d_i < \sqrt{(x_i - x_o)^2 + (y_i - y_o)^2} + L \\ v_i < 4, \dot{v}_i < 5 \\ i = 0, 1, \cdots, t. \end{cases} \tag{18}$$

The coordinates are (2, 5.3), (4, 2), (6, 0.6), (8, 0.6), (10, 2), and (12, 5.3). Figure 5(a) illustrated the initial path of the selected initial control node and its description.

Through the six control points designed above, it is possible to effectively limit the overall speed of the UAV's movement, but due to the large position difference between the points, the vehicle will appear in various processes during point-to-point flight. To enable the UAV to fly stably and smoothly and to consider different deviations, we defined the cubic B-spline basis function to refine the path between the points and the vehicle according to the function. The task is divided into more subtle phase control objectives, and the basis function of the B-spline is defined as

$$\begin{cases} N_{i,o}(u) = \begin{cases} 0, u_i \le u < u_{i+1}, \\ 1, \quad \text{otherwise}, \end{cases} \\ N_{i,p}(u) = \dfrac{u - u_i}{u_{i+p} - u_i} N_{i,p-1}(u) + \dfrac{u_{i+p+1} - u}{u_{i+p+1}} N_{i+1,p-1}(u), \end{cases} \tag{19}$$

where p represents the degree of basis functions, u_i is the node, and $N_{i,p}(u)$ represents $i - th$ B-spline basis function of degree p. The cubic B-spline function nodes between the step length are set as 0.01, and then the location of the basis functions can be obtained according to the function between adjacent nodes. The specific way is derived as shown in Figure 6, and the basis function location point is the change over time in the process of UAV control at the desired location.

All the desired nodes of UAV movement can be calculated according to the cubic B-spline basis function described above. As shown in Figure 5(b), these are connected to form the desired trajectory of the UAV, and each of the subnode is a subtarget point of the vehicle during the cycle. Figure 7 shows the velocity and acceleration of the planned path and proves that the constraints of speed and acceleration are properly met.

4. Sliding Mode PID Controller Design

The sliding mode PID control presented in this section is obtained by combining the PID control and the sliding mode control laws. The stability and robustness of the

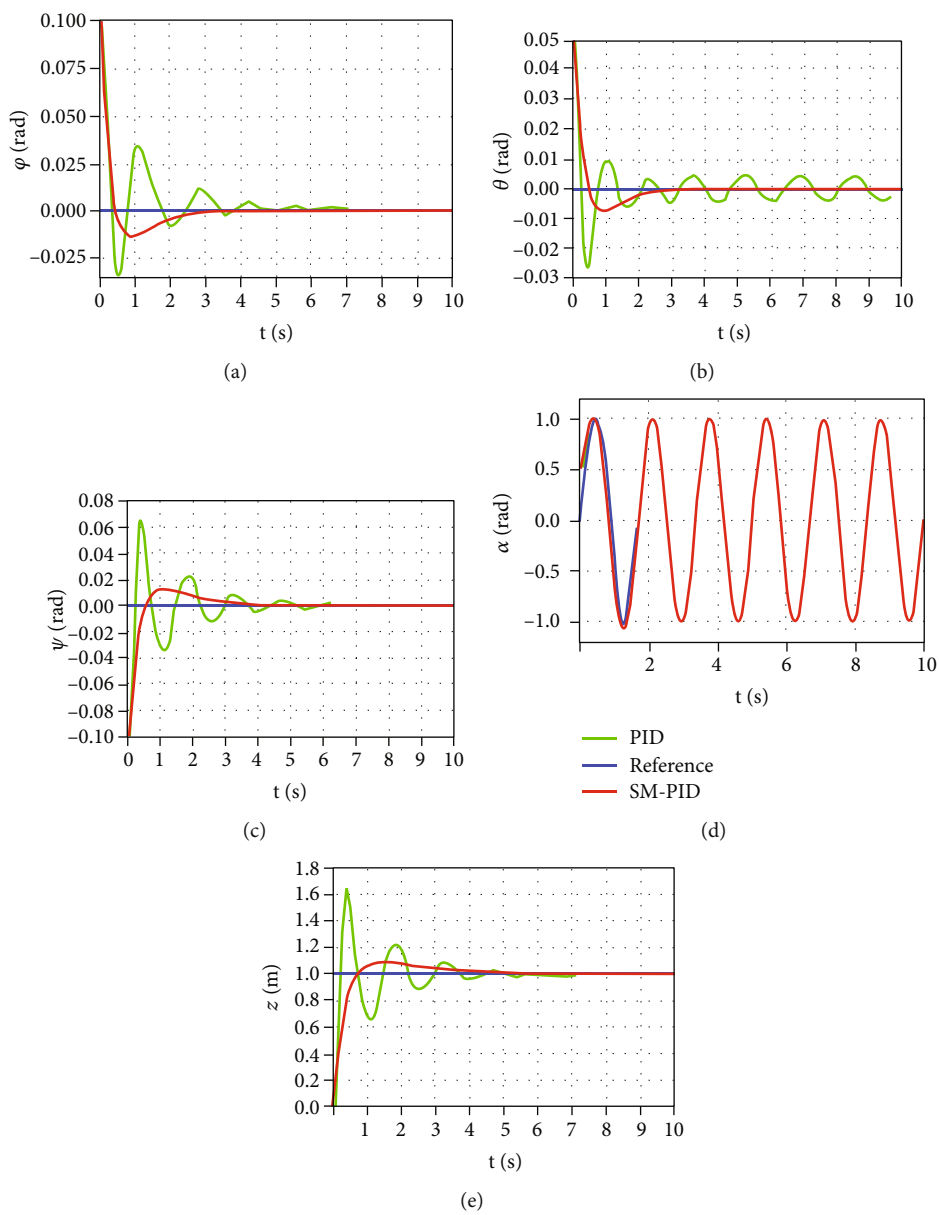

Figure 10: SM-PID control and attitude profile under PID control. (a) Rolling angle. (b) Pitch angle. (c)Yaw angle. (d) Pull down tilt angle. (e)Altitude change.

quadrotor control can be greatly improved by combining the advantages of each control. The position control of the quadrotor can be divided into horizontal position and altitude control. Since the system uses four inputs to control six degrees of freedom, it is an under-driven, strongly coupled nonlinear system. We have established the mathematical relationship between attitude angle and position and height control quantities to achieve the purpose of trajectory tracking by continuously adjusting attitude angle and position height. Figure 8 illustrates the control flow diagram of the sliding mode PID control system.

The horizontal position and the pull-down tilt angle are controlled by PID, and the control laws of x, y, α are designed by the relationship between the desired position (x_d, y_d) and the desired acceleration $(\ddot{x}_d, \ddot{y}_d)$, the desired tilt angle α_d, and the angular acceleration $\ddot{\alpha}$ of the robot arm:

$$\begin{aligned}
\ddot{x} &= k_{p_1}(x_d - x) + k_{i_1}\int(x_d - x)dt + k_{d_1}(\dot{x}_d - \dot{x}),\\
\ddot{y} &= k_{p_2}(y_d - y) + k_{i_2}\int(y_d - y)dt + k_{d_2}(\dot{y}_d - \dot{y}),\\
\ddot{\alpha} &= k_{p_3}(\alpha_d - \alpha) + k_{i_3}\int(\alpha_d - \alpha)dt + k_{d_3}(\dot{\alpha}_d - \dot{\alpha}).
\end{aligned} \tag{20}$$

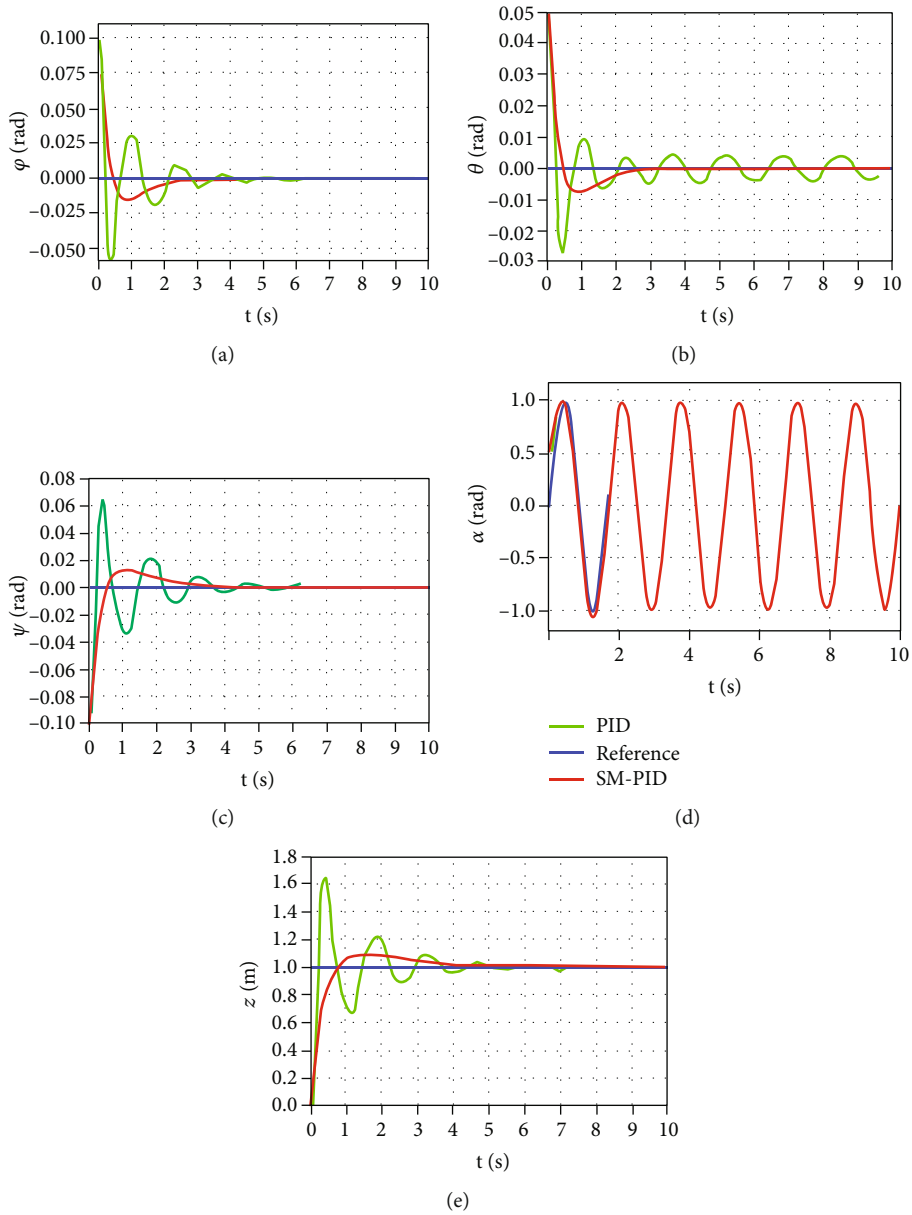

Figure 11: Attitude curves under two types of control under sinusoidal motion. (a) Rolling angle. (b) Pitch angle. (c) Yaw angle. (d) Pull down tilt angle. (e) Altitude change.

The design of the sliding mode PID controller includes the selection of the sliding mode surface and the design of the control law. The sliding mode surface is generally selected as $s = 0$. Then, the control goal of the sliding mode PID is outlined to make the function of the sliding mode surface finally stable near the sliding mode surface, finally achieving stable control.

We have used the sliding mode PID algorithm to control the height design, and z_d, z indicate the desired and actual height. So, we can define the error between them as

$$e_z = z_d - z. \tag{21}$$

The slip surface function is designed as

$$s_z = \dot{e}_z + d_1 * e_z + c_1 * \int e_z dt. \tag{22}$$

To ensure that the system converges to the sliding mode at high speed for large values of s, the exponential convergence rate is chosen to derive U_1:

$$\dot{s}_z = -\varepsilon \operatorname{sgn}(s_z) - k s_z, \tag{23}$$

where s takes the value of 0.01, k takes the value of 3, and $\operatorname{sgn}(s)$ denotes the symbolic function. The Lyapunov

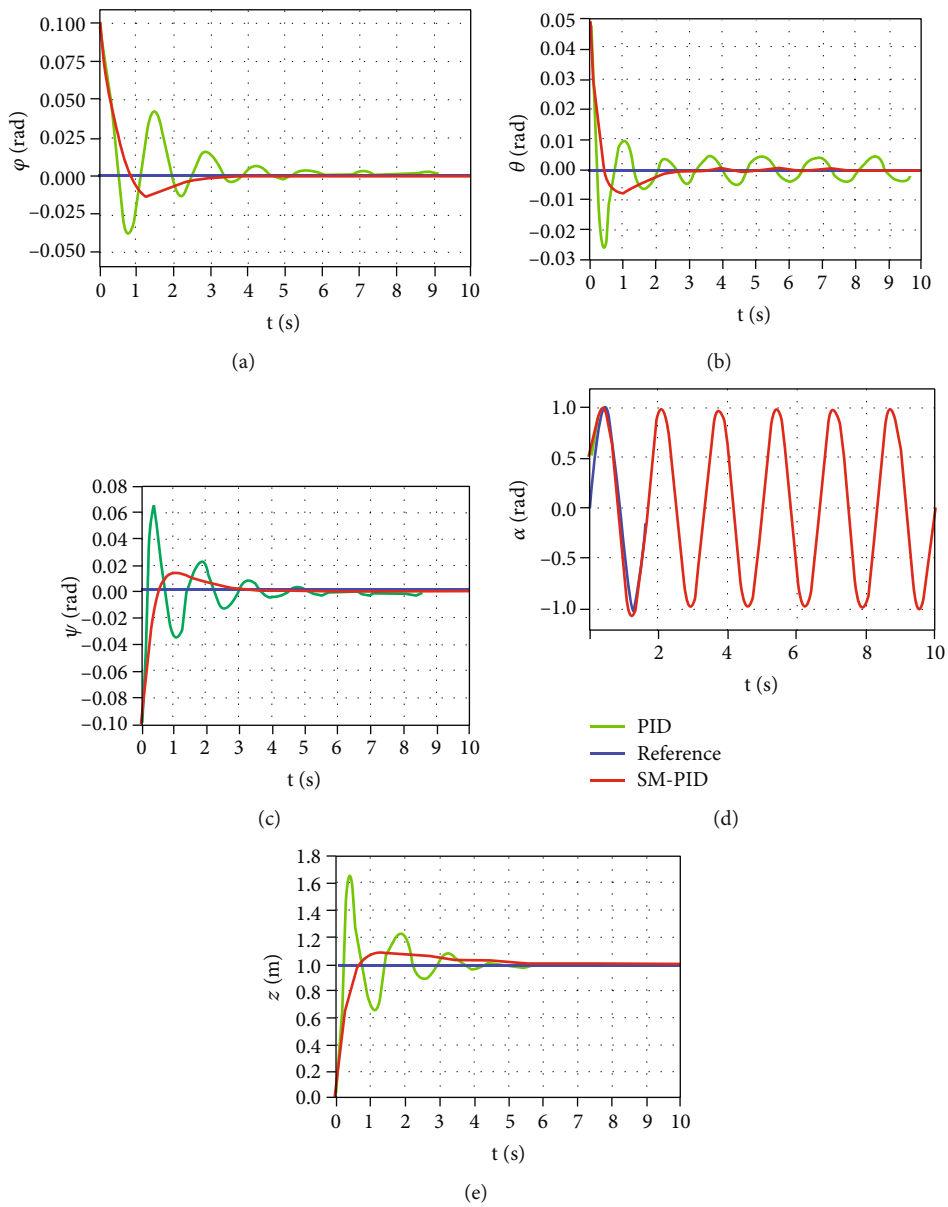

Figure 12: Attitude profiles for two controls under sinusoidal motion and perturbation. (a) Rolling angle. (b) Pitch angle. (c) Yaw angle. (d) Pull down tilt angle. (e) Altitude change.

function is used to determine the stability of the system, and its positive definite function is designed:

$$V_z = \frac{1}{2} s_z{}^2. \tag{24}$$

Then, its derivative along the track line is

$$\dot{V}_z = s_z \dot{s}_z = s_z[-\varepsilon \operatorname{sgn}(s_z) - k s_z] = -\varepsilon \|s_z\| - k \|s_z\|^2 < 0. \tag{25}$$

Therefore, the kinetic model satisfies the stability criterion of Lyapunov asymptotic stability and is an asymptotically stable system. This means that the error function will slowly converge to 0 over time and can eventually arrive at the sliding mode.

5. Experimental Verification

5.1. Theoretical Simulation. The aforementioned steps can be used to obtain the position of the UAV at different time periods. Then, these input points are used as control inputs of the simulation, which is designed according to the control flow in Figure 8. Simulink was used to carry out simulation analysis of the system, and two control modules (controller module U and power module Muav) were built with s-function. The simulation structure diagram is shown in Figure 9. The sequence of points obtained in Section 3 is set as a continuous input that changes with time, which means that the trajectory planning based on the segmentation control is achieved by giving different desired targets to the UAV in different time periods.

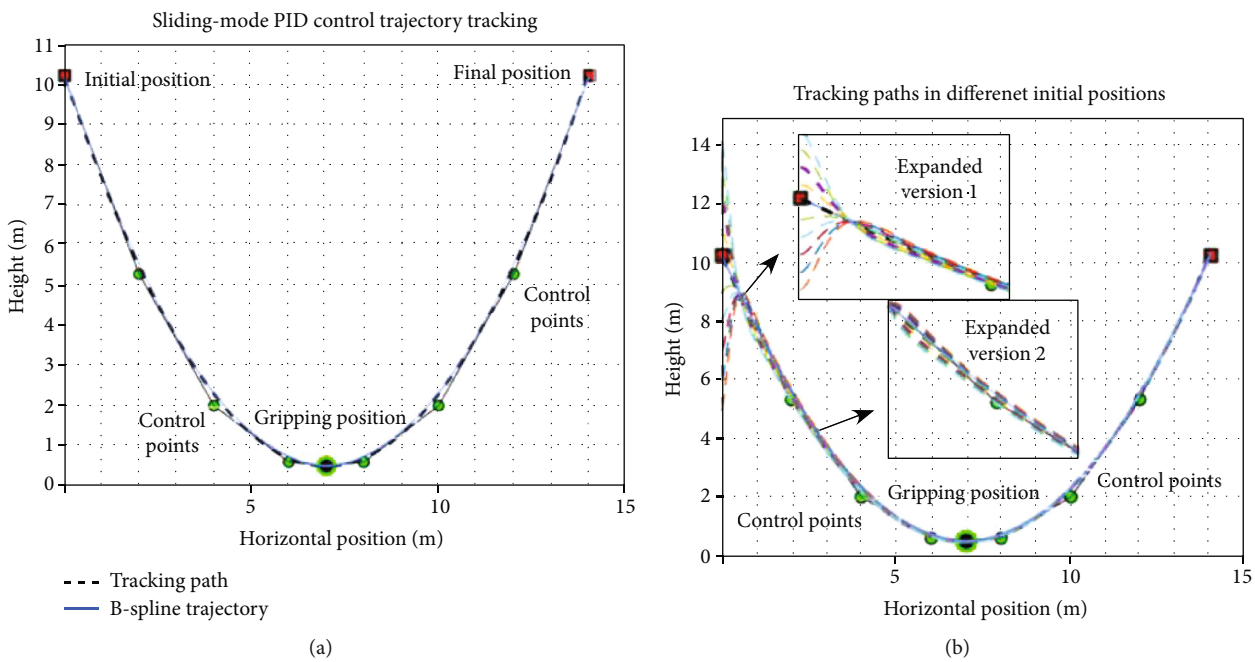

Figure 13: Influence of initial position on tracking effect. (a) Trajectory tracking control. (b) Tracking trajectories at different initial positions.

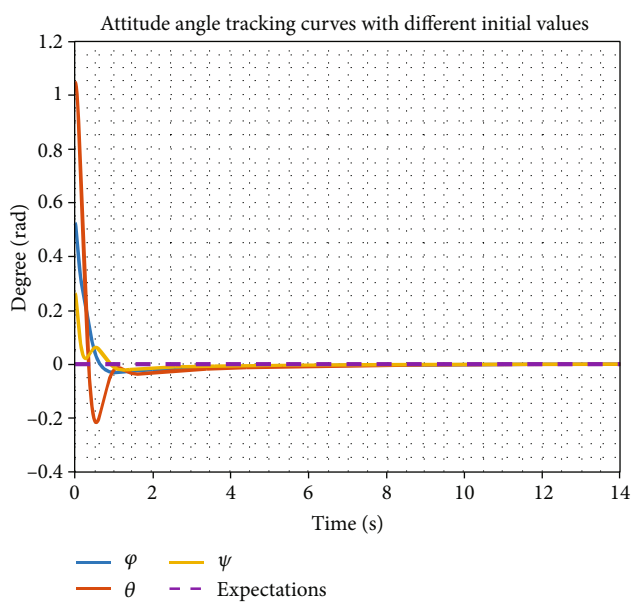

Figure 14: Attitude angle curve.

As shown in Figure 9, simulation through Simulink can get the data of each position and attitude angle of the quadrotor. The primary purpose of this research is to study and analyze its stability, so the specific analysis of the attitude angle and the altitude at the following figure is based on the above input values and expected values using sliding mode PID control and PID control. Both are used to obtain the UAV's attitude curve.

As shown in Figure 10, the simulation shows that in the sliding mode PID control, the adjustment time of pitch and roll angle is about 3.2 s, and the adjustment time of yaw angle is 4 s, which can converge to the desired value after a reduced adjustment time. The tilt angle of the pull-down robot arm converges to the desired value at 2.5 s and remains unchanged, while the height value converges to the desired value at 5.5 s. At this stage, the adjustment time in the PID control is 6 s, 6 s, 6.4 s, 7.2 s, and 5.5 s, respectively. We identified that the adjustment time in each direction tends to increase a lot, while the overshoot of PID is much larger than that of the sliding mode PID. The fluctuation amplitude and flatness are larger, and the sliding mode PID is smoother.

Figure 15: UAV flight test.

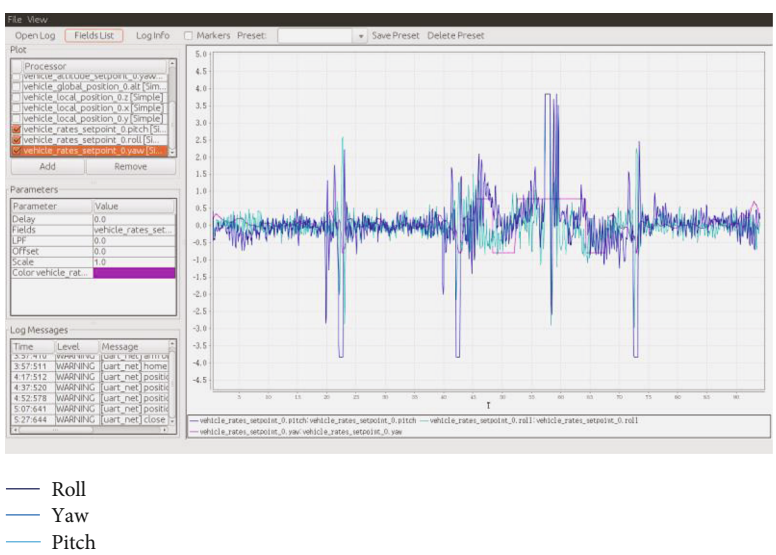

Figure 16: UAV flight attitude angle.

Figure 11 shows a periodic sine wave with a desired tilt angle changed to a frequency of 1.2π rad/s and an amplitude of 1. The tracking effect of the two controls is compared when the desired motion of the robotic arm is sinusoidal. The results show that when the desired tilt angle of the robot arm fluctuates sinusoidally, the adjustment time will grow accordingly, and the sinusoidal motion of the robot arm will affect the change of the pitch angle. Then, the pitch angle in the sliding mode PID control will show smaller fluctuations up and down, while the pitch angle in the PID control will produce larger fluctuations. These fluctuations will always exist and move up and down around the expected value in

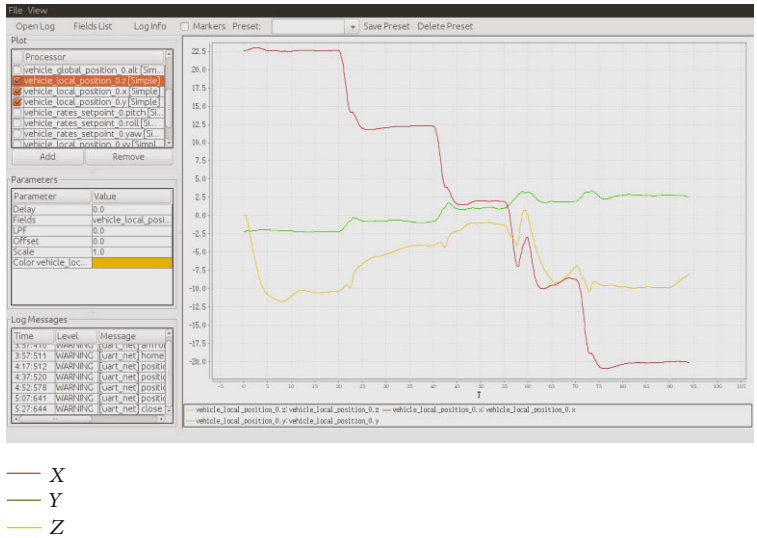

Figure 17: Displacement of UAV.

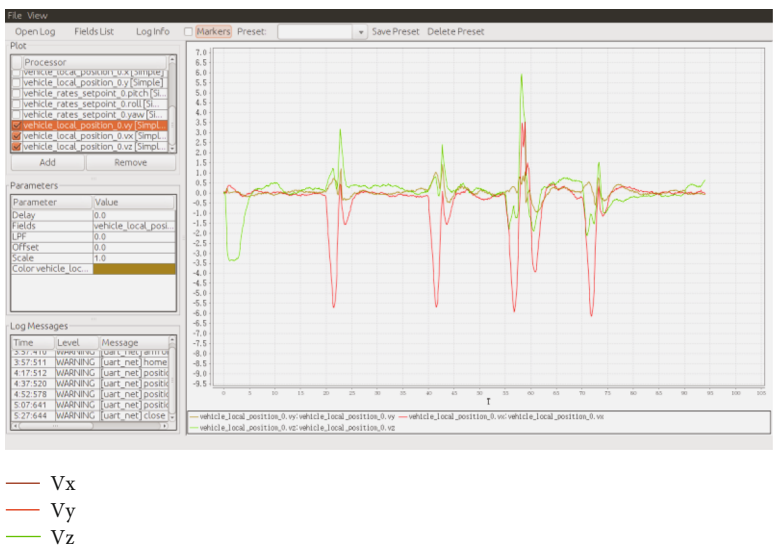

Figure 18: Movement speed of the UAV.

an approximate sinusoidal wave, making it difficult to reach the desired state. This is mainly due to the oscillation of the pulled-down object affecting the stability of the whole system in the x-axis direction. Furthermore, the anti-interference ability of PID is not as strong as that of the sliding-mode PID control, so it also triggers inevitable fluctuations in the pitch angle.

Figure 12 shows the attitude waveforms produced by adding appropriate perturbations to both control systems under the condition that the tilt angle expectation is a sine wave. The response time of both controllers increases relatively by a few seconds, but the waveform of the PID controller shows strong vibrations after adding the perturbation. We have also identified small periodic fluctuations in each attitude after a long-time adjustment, but the same phenomenon was not identified in the sliding mode controller, which also confirms that the sliding mode PID control is more resistant to disturbance than the PID control. Our observations point out that the sliding mode PID control is more robust to external disturbance and parameters, has strong antidisturbance characteristics against external disturbances and parameter uptake, and has strong robustness and self-adaptability.

The simulation model is built by Simulink according to the above control flow and procedures, and the established dynamic model and the control method are input into it. Figure 13(a) shows the path of the UAV on Bx and Bz, and Figure 13(b) shows the influence of different initial heights on the trajectory tracking of the UAV. As shown, as the UAV moves away from the preset initial position

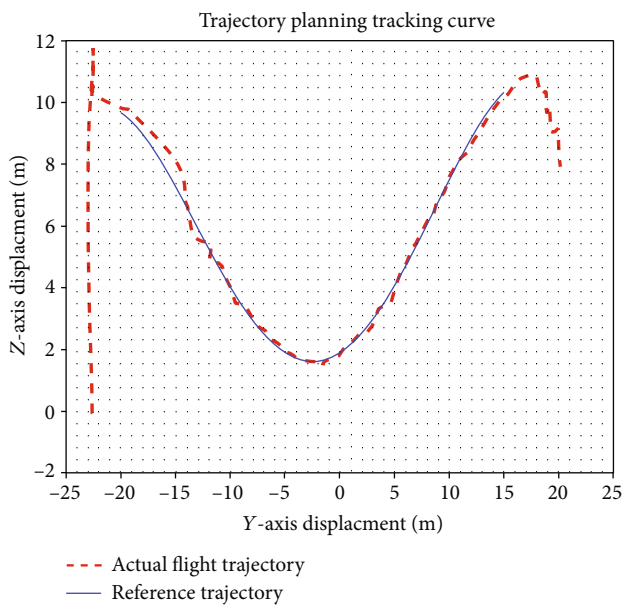

Figure 19: Trajectory planning tracking curve.

offset, it needs more real-time tracking. The longer the adjustment time, the greater the deviation and the more time it takes to reach the steady state. Figure 14 shows the performance results of the respective attitude curves in Figure 13 (a) reaching steady state.

5.2. Flight Experiment. The x-axis and z-axis coordinates of the path points obtained by Matlab simulation were imported and then divided into two arrays as the target expectation function of their respective changing with time. The flying robot arm successfully functioned after continuously giving the desired position of the drone through the cycle. Grab the trajectory plan. Figure 15 is a snapshot of several key points of the actual flight. It can be seen that the path point settings are generally in line with the planned Section 4.

Figures 16, 17, and 18 show the attitude angle, relative offset position, and motion speed of the UAV when it is grabbing the track. As shown in Figure 16, the change of the attitude angle of the UAV is small, fluctuating within the range ±1°, and the maximum deviation of the yaw angle is about ±4°, which basically meets the stability requirements of the vehicle. According to the above indicators, it can be concluded that the sliding mode PID is effective in the stability control of the drone. Furthermore, in the above flight curve, the movement of the mechanical arm is also controlled by the remote controller to increase the disturbance during the movement through the actual flight. The attitude curve also confirms that the drone can still achieve its stability quickly through the sliding mode PID control with the addition of disturbance.

As shown in Figure 17, in the x and y-axis direction can be found in the UAV in the x-axis direction has been decreasing, which is the direction of flight of the UAV in the experiment is to fly from north to south, and in the Earth's coordinate system x-axis to north as positive, y-axis to east as positive, so the UAV in the x-axis direction is always decreasing. According to Figure 18, it can be found that the velocity of v_x and v_y is within the range of ±1.5/s, and the velocity of v_y is within the range of 3.5m/s~6m/s, which basically conforms to the relevant constraints set in this paper.

Figure 19 is a comparative analysis between the flight trajectory designed using trajectory planning and the actual flight trajectory, it can be found that the flight path of the UAV is flying up and down around the preset trajectory, and the error is basically in line with the control requirements of the UAV from large to small.

6. Conclusion

This research introduced the differential flatness theory as a means to solve the problems in aircraft trajectory planning with nonintegrity constraints. Throughout this research, the steps of trajectory generation based on differential flatness are explained in detail considering the theory's basic concepts and properties. The flat output was determined by the flat property of the dynamics and kinematics of the aircraft, and B-spline was adopted to parameterize the flat output and transform the optimal control problem into a general nonlinear programming problem to reduce the difficulty. In addition, the methodology used in this study optimized the traditional PID control by using the sliding mode control, which enhances the anti-interference and fast response capability of the UAV. Finally, the mathematical model of the UAV contained input into the control model to achieve a good tracking simulation based on the above trajectory. All of these procedures were used to verify the trajectory planning of the B-spline based on the differential flat.

This research proves that the differential flatness theory can better solve the trajectory planning problem of nonintegrity constraint systems. It is easier to find the most suitable setting in the appropriate output space by representing the flat system's input and state by the output and its finite differential term. This methodology can also be used to optimize solutions and then map them to the state space, which greatly reduces the difficulty of solving the control variables.

Symbols

symbol:	Symbol description
m_1:	Quadrotor mass
m_2:	Robot arm mass
g:	Local acceleration of gravity
L:	Distance from centroid to motor
Ω:	Rotor speed of revolution
C_T:	Rotor lift factor
C_Q:	Rotor torque factor
R:	Rotor radius
ρ:	Air density
I_x:	The moment of inertia about axis B_x

I_y: The moment of inertia about axis *By*

I_z: The moment of inertia about axis *Bz*.

Data Availability

The data used to support the findings of this study are included within the article.

Conflicts of Interest

The authors declare that they have no conflicts of interest.

Acknowledgments

This project is supported by National Natural Science Foundation of China (Grant no. 51875293).

References

[1] K. Nonami, "Prospect and recent research & development for civil use autonomous unmanned aircraft as UAV and MAV," *Journal of System Design and Dynamics*, vol. 1, no. 2, pp. 120–128, 2007.

[2] H. Cai and Q. Geng, "Research on the development process and trend of unmanned aerial vehicle," *Proceedings of 2015 International Industrial Informatics and Computer Engineering Conference*, 2015.

[3] N. Yin, R. Liu, B. Zeng, and N. Liu, "A review: UAV-based remote sensing," *Proceedings of the 2nd International Symposium on Application of Materials Science and Energy Materials*, vol. 490, 2019.

[4] D. H. Yeon and J. R. Morrison, "Development of vision tracking and landing for persistent UAV system," *Proceedings of Spring Conference of Korean Society of Industrial Engineering*, pp. 1054–1054, 2018.

[5] Y. Lu, Z. Xue, G. S. Xia, and L. Zhang, "A survey on vision-based UAV navigation," *Geo-Spatial Information Science*, vol. 21, pp. 1–12, 2018.

[6] H. Y. Irwanto, "Development of autonomous controller system of high speed UAV from simulation to ready to fly condition," *Journal of Physics Conference Series*, vol. 962, p. 012015, 2018.

[7] D. M. Vijayakumari, S. Kim, J. Suk, and H. Mo, "Receding-horizon trajectory planning for multiple UAVs using particle swarm optimization," *AIAA Scitech 2019 Forum*, pp. 1165–2019, 2019.

[8] C. Sampedro, H. Bavle, J. L. Sanchez-Lopez et al., "A flexible and dynamic mission planning architecture for UAV swarm coordination," in *2016 International Conference on Unmanned Aircraft Systems (ICUAS) IEEE*, Arlington, VA, USA, 2016.

[9] N. B. Hui and D. K. Pratihar, "A comparative study on some navigation schemes of a real robot tackling moving obstacles," *Robotics and Computer-Integrated Manufacturing*, vol. 25, no. 4-5, pp. 810–828, 2009.

[10] C. Mou, W. Qing-Xian, and J. Chang-Sheng, "A modified ant optimization algorithm for path planning of UCAV," *Applied Soft Computing Journal*, vol. 8, no. 4, pp. 1712–1718, 2008.

[11] R. Marie, H. B. Said, J. Stéphant, and O. Labbani-Igbida, "Visual servoing on the generalized Voronoi diagram using an omnidirectional camera," *Journal of Intelligent and Robotic Systems*, vol. 94, no. 3-4, pp. 793–804, 2019.

[12] P. Marin-Plaza, A. Hussein, D. Martin, and A. D. L. Escalera, "Global and local path planning study in a ROS-based research platform for autonomous vehicles," *Journal of Advanced Transportation*, vol. 2018, 10 pages, 2018.

[13] F. Bounini, D. Gingras, H. Pollart, and D. Gruyer, "Modified artificial potential field method for online path planning applications," *2017 IEEE Intelligent Vehicles Symposium (IV) IEEE*, 2017.

[14] J. Sun, J. Tang, and S. Lao, "Collision avoidance for cooperative UAVs with optimized artificial potential field algorithm," *IEEE Access*, vol. 5, pp. 18382–18390, 2017.

[15] J. D. Silva Arantes, M. D. Silva Arantes, C. F. Motta Toledo, O. T. Júnior, and B. C. Williams, "Heuristic and genetic algorithm approaches for UAV path planning under critical situation," *International Journal of Artificial Intelligence Tools*, vol. 26, no. 1, p. 1760008, 2017.

[16] S. Perez-Carabaza, E. Besada-Portas, J. A. Lopez-Orozco, and J. M. de la Cruz, "Ant colony optimization for multi-UAV minimum time search in uncertain domains," *Applied Soft Computing*, vol. 62, pp. 789–806, 2018.

[17] V. Ghadiok, J. Goldin, and W. Ren, "Autonomous indoor aerial gripping using a quadrotor," in *2011 IEEE/RSJ International Conference on Intelligent Robots and Systems*, San Francisco, CA, USA, 2011.

[18] Z. Qu, J. Wang, and C. E. Plaisted, "A new analytical solution to mobile robot trajectory generation in the presence of moving obstacles," *IEEE Transactions on Robotics*, vol. 20, no. 6, pp. 978–993, 2004.

[19] F. Antritter, "On the relations between different flatness based design methods for tracking controllers," in *American Control Conference*, pp. 1740–1745, Seattle, WA, USA, 2008.

[20] W. Dong and Y. Guo, "New trajectory generation methods for nonholonomic mobile robots," *Proceedings of the 2005 International Symposium on IEEE*, 2005.

[21] Y. Guo, Y. Long, and W. Sheng, "Global trajectory generation for nonholonomic robots in dynamic environments," *Robotics and Automation*, pp. 1324–1329, 2007.

[22] N. Faiz, S. Agrawal, and R. Murray, "Trajectory planning of differentially flat systems with dynamics and inequalities," *Journal of Guidance, Control, and Dynamics*, vol. 24, no. 2, pp. 219–227, 2001.

[23] V. Ghadiok, J. Goldin, and W. Ren, "On the design and development of attitude stabilization, vision-based navigation, and aerial gripping for a low-cost quadrotor," *Autonomous Robots*, vol. 33, no. 1-2, pp. 41–68, 2012.

[24] R. Spica, A. Franchi, G. Oriolo, H. H. Bülthoff, and P. R. Giordano, "Aerial grasping of a moving target with a quadrotor UAV," *IEEE/RSJ International Conference on Intelligent Robots & Systems IEEE*, 2012.

[25] J. Thomas, G. Loianno, J. Polin, K. Sreenath, and V. Kumar, "Toward autonomous avian-inspired grasping for micro aerial vehicles," *Bioinspiration & Biomimetics*, vol. 9, no. 2, article 025010, 2014.

[26] A. A. B. John and R. Dutta, "Cooperative trajectory planning in an intercommunicating group of UAVs for convex plume wrapping," *Sarnoff Symposium*, pp. 1–6, 2017.

[27] L. Zhang, J. Chen, and F. Deng, "Aircraft trajectory planning for improving vision-based target geolocation performance," *2017 13th IEEE International Conference on Control & Automation (ICCA) IEEE*, 2017.

[28] B. Penin, R. Spica, P. R. Giordano, and F. Chaumette, "Vision-based minimum-time trajectory generation for a quadrotor UAV," *IEEE/RSJ International Conference on Intelligent Robots & Systems IEEE*, 2017.

[29] M. B. Milam, K. Mushambi, and R. M. Murray, "A new computational approach to real-time trajectory generation for constrained mechanical systems," *IEEE Conference on Decision & Control*, Vancouver, BC, Canada, 2000.

[30] O. Mofid and S. Mobayen, "Adaptive sliding mode control for finite-time stability of quad-rotor UAVs with parametric uncertainties," *ISA Transactions*, vol. 72, pp. 1–14, 2018.

[31] A. K. Singh and L. Dewan, "Adaptive-PID with sliding mode control for longitudinal flight of an UAV," *MR International Journal of Engineering & Technology*, vol. 4, pp. 1–6, 2018.

Hindawi
International Journal of Aerospace Engineering
Volume 2022, Article ID 9391236, 15 pages
https://doi.org/10.1155/2022/9391236

Research Article

Robust Integrated Guidance and Control Design for Angle Penetration Attack of Multimissiles

Huan Zhou and Xin Zhao

Aviation Engineering School, Air Force Engineering University, Xi'an, China

Correspondence should be addressed to Xin Zhao; 2182597520@qq.com

Received 14 January 2022; Revised 5 May 2022; Accepted 9 May 2022; Published 20 May 2022

Academic Editor: Miaomiao Wang

Angle penetration attack ability plays a more and more important role for missiles in modern warfare, and the traditional separate guidance and control system design problem is the key to restrict the improvement of time-sensitive attack and cooperative attack ability of multimissiles. Firstly, the deviation control strategy of line-of-sight angle and attack angle is put forward in this paper, and the integrated guidance and control system model with impact angle constraint is established, according to the characteristics of angle penetration attack. Then, an integrated guidance and control controller for angle penetration attack is designed by using adaptive dynamic surface control, with the dynamic constraints, nonlinear input saturation, and terminal line-of-sight and attack angle constraints concerned. In order to ensure the robustness of the system, nonlinear disturbance observers are introduced to estimate the uncertainty of the system model. Finally, the stability of the integrated design method is proven based on the Lyapunov theory. Simulation results verify the effectiveness of the integrated guidance and control design method proposed in this paper in multimissile angle penetration attack.

1. Introduction

Multimissile angle penetration attack is a combat mode in which multiple missiles strike the target at different terminal impact angles. It plays an irreplaceable important role in modern war by meeting a variety of specific combat requirements to destroy the enemy target to the greatest extent [1, 2]. In the process of multimissile attack mission, the guidance and control system is the key to realize cooperative precision attack, and the performance of the system will ultimately determine the operational effectiveness of the missile.

The traditional design scheme of the missile guidance and control system is to separate the guidance system from the control system and then design two systems separately [3, 4]. The core of the traditional separate guidance and control design method lies in the design of guidance law. The designed system gives the desired control command through the guidance law and then executes the control command by the flight control system, in order to control the missile to maintain a stable flight attitude and perform the task of attacking battlefield targets.

In the design of attack time cooperation, Jeon et al. [5] proposed an attack time control guidance law for antiship missiles based on the idea of optimal control. Kumar and Ghose [6] set the error term between the preset attack time and the remaining attack time, added it to the proportional guidance law, and designed a new guidance law through the sliding mode control method to ensure that the preset attack time constraints are met. Both the attack time control guidance law and the sliding mode guidance law do not fully consider the interaction and cooperation in the flight process of missiles; therefore, Ref. [7, 8] designed a two-layer structure of cooperative guidance framework and cooperative proportional guidance law. In the process of combat flight, missiles share the remaining attack time information through online data link and adjust its own flight state in real time to achieve the coordination of the final attack time. In terms of the impact angle cooperation, Harl and Balakrishnan [9] designed a cooperative guidance law with attack time and attack angle constraints based on sliding mode control and comprehensively adopted line-of-sight rate adjustment technology and second-order sliding mode

method to meet the attack time and attack angle constraints. Jung and Kim [10] designed the offset proportional guidance law by using the backstepping control method, in which the offset term comprehensively considered the attack time error and attack angle error.

The traditional guidance and control system design scheme can realize the cooperative attack flight guidance and control of multimissiles by designing the cooperative guidance law. However, the time constant of the guidance loop becomes smaller and the bandwidth becomes larger with the gradual reduction of the relative distance between the missile and the target. At this time, the assumption of frequency spectrum separation will no longer be tenable; the traditional separation design scheme will lead to the problems that seriously restrict the missile combat capability, such as sharp performance degradation, large miss distance, and flight instability. The integrated guidance and control (IGC) scheme is an effective way to solve this problem [11, 12].

The research on the IGC mainly focuses on the control of a single aircraft/missile, mainly including optimal control method [13], backstepping control method [14], sliding mode control method [15], trajectory linearization control method [16], and dynamic surface control method [17]. It is extremely difficult to apply the IGC to the cooperative control of multimissiles. In particular for the angle penetration attack, the guidance and control system should not only ensure that the terminal impact angle attitude of each missile meets a specific constraint requirement but also minimize the attack angle of missiles when intercepting the target. At the same time, the existing cooperative IGC design lacks full consideration and in-depth research on the problems of system stability and robustness caused by the nonlinearity and time variability of the missile itself, the perturbation of missile aerodynamic parameters, and the limitation of input saturation.

The dynamic surface control method is first proposed by Swaroop et al. [17], to overcome the problem of "item explosion" in backstepping control method and sliding mode control method. Its basic idea is to add a first-order low-pass filter between the designs of the two-step control laws of the original backstepping control, so as to avoid the direct differentiation of some nonlinear signals in the next design [18]. The deficiency of the dynamic surface control method is how to improve its adaptive and robust performance in complex system environment.

The IGC system modelling of multimissile angle penetration attack is a typical nonlinear problem, which is very difficult to control [19, 20]. The contribution of this work is to design a robust IGC method to increase the adaptive and robust performance of the DSC when the missile system itself has control input saturation, and there is nonlinearly parameterized no-matching uncertainty in the system. Meanwhile, the cooperative problem of the IGC control is effectively processed.

Aimed at the problem of multimissile cooperative attack on one stationary target, a three-channel independent decoupling model of the integrated guidance and control (IGC) system with impact angle constraint is established firstly, according to the requirements of angle penetration attack. On this basis, a robust IGC control method for angle penetration attack is designed by using adaptive dynamic surface (DSC) control and nonlinear disturbance observer (NDO) technology. Finally, simulation experiments are carried out, in order to verify the effectiveness of the IGC design method proposed for multimissile angle penetration attack.

2. IGC System Modelling of Multimissile Angle Penetration Attack

The flight control system model of a single missile and the three-channel independent decoupling model of the IGC system are shown in document [21, 22]. This section mainly establishes the cooperative IGC system model of multimissiles with impact angle constraints according to the relative motion relationship for angle penetration attack between multimissiles and the target. In order to ensure the coordination of the flight state of multiple missiles, the photoelectric infrared detector can obtain the corresponding distance and angle information, but the price is expensive. In practice, the small radar or radio spectrum detection equipment can be put on every missile for a distributed control system, or the data of each missile comes from the central data link.

2.1. Relative Motion Relationship between Multimissiles and Targets. At the end of multimissile cooperative attack, assuming that N missiles attack one target and the target is stationary, the relative motion relationship between each missile and the target in the three-dimensional environment can be decomposed into independent relative motions in the longitudinal and lateral planes. The relative motion relationships in the two planes are shown in Figure 1(a) and 1(b), respectively.

In Figure 1, all quantities including subscripts y, z represent the components of missile and target related parameters in the longitudinal plane and lateral plane, respectively, where $R_{i,y}, R_{i,z}$ is the relative distance between the i-th missile and the target. By omitting the subscript i for convenience, V_{uy}, V_{uz} and V_{ty}, V_{tz} represent the speed of the i-th missile and the target, respectively; $\varphi_{uy}, \varphi_{uz}$ represent the included angle between the velocity vector of the i-th missile and the reference plane, that is, the track inclination and track deflection angle of the missile; $\varphi_{ty}, \varphi_{tz}$ are the angle between the target velocity vector and the reference plane, that is, the track inclination and track deflection angle of the target; $\varphi_{ry}, \varphi_{rz}$ are the line-of-sight (LOS) angle between the i-th missile and the target.

For the longitudinal plane pitch channel, the relative motion equation between the i-th missile and the target can be obtained from Figure 1(a):

$$\begin{cases} \dot{R}_y = -V_{uy} \cos\left(\varphi_{ry} - \varphi_{uy}\right), \\ R_y \dot{\varphi}_{ry} = V_{uy} \sin\left(\varphi_{ry} - \varphi_{uy}\right). \end{cases} \tag{1}$$

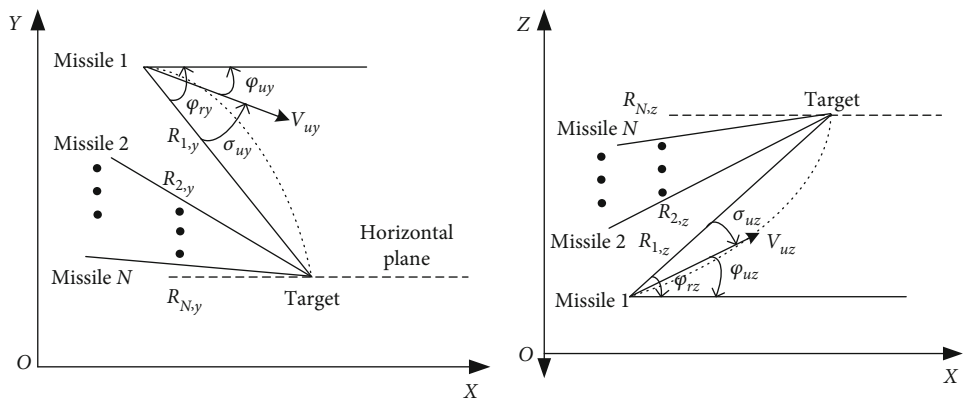

(a) Relative motion in the longitudinal plane

(b) Relative motion in the lateral plane

Figure 1: Relative motion relationship between N missiles and one target.

By differentiating on both sides of equation (1), we get

$$\ddot{\varphi}_{ry} = \left[\frac{\dot{V}_{uy}}{V_{uy}} - \frac{2\dot{R}_y}{R_y}\right]\dot{\varphi}_{ry} + \frac{\dot{R}_y}{R_y}\dot{\varphi}_{uy}. \tag{2}$$

On the basis of Ref. [18], by adding the track inclination of the missile to the pitch channel subsystem, the pitch channel subsystem of the missile becomes

$$\begin{cases} \dot{\theta} = \dfrac{qSc_y^{\alpha} + P}{mV}\alpha + \Delta\theta, \\ \dot{\alpha} = \omega_z - \dfrac{qSc_y^{\alpha} + P}{mV}\alpha + \Delta\alpha, \\ \dot{\omega}_z = \dfrac{qSL}{J_z}\left(m_z^{\alpha}\alpha + m_z^{\delta_z}\delta_z + m_z^{\omega_z}\omega_z\right) + \Delta\omega_z, \end{cases} \tag{3}$$

where θ, α, w_z represent the track inclination, attack angle, and pitch angle rate of the missile, respectively, and $\Delta\theta, \Delta\alpha, \Delta w_z$ represent the corresponding unknown bounded uncertainty. The physical quantities represented by other parameters are shown in Ref. [18].

Combining equations (2) and (3), the following can be obtained:

$$\ddot{\varphi}_{ry} = \left[\frac{\dot{V}_{uy}}{V_{uy}} - \frac{2\dot{R}_y}{R_y}\right]\dot{\varphi}_{ry} + \frac{\left(qSc_y^{\alpha} + P\right)\dot{R}_y}{mV_{uy}R_y}\alpha + \Delta\varphi_{ry}. \tag{4}$$

Similarly, for the lateral plane yaw channel, the relative motion equation between the i-th missile and the target can be obtained from Figure 1(b):

$$\begin{cases} \dot{R}_z = -V_{uz}\cos\left(\varphi_{rz} - \varphi_{uz}\right), \\ R_z\dot{\varphi}_{rz} = V_{uz}\sin\left(\varphi_{rz} - \varphi_{uz}\right). \end{cases} \tag{5}$$

By differentiating on both sides of equation (5), we get

$$\ddot{\varphi}_{rz} = \left[\frac{\dot{V}_{uz}}{V_{uz}} - \frac{2\dot{R}_z}{R_z}\right]\dot{\varphi}_{rz} + \frac{\dot{R}_z}{R_z}\dot{\varphi}_{uz}. \tag{6}$$

On the basis of Ref. [18], by adding the track deflection angle of the missile to the yaw channel subsystem, the yaw channel subsystem of the missile becomes

$$\begin{cases} \dot{\psi} = -\dfrac{qSc_z^{\beta} - P}{mV}\beta + \Delta\psi, \\ \dot{\beta} = \omega_y + \dfrac{qSc_z^{\beta} - P}{mV}\beta + \Delta\beta, \\ \dot{\omega}_y = \dfrac{qSL}{J_y}\left(m_y^{\beta}\beta + m_y^{\delta_y}\delta_y + m_y^{\omega_y}\omega_y\right) + \Delta\omega_y, \end{cases} \tag{7}$$

where ψ, β, w_y represent the track yaw angle, sideslip angle, and yaw angle rate of the missile, respectively, and $\Delta\psi, \Delta\beta, \Delta w_y$ represent the corresponding unknown bounded uncertainty. The physical quantities represented by other parameters are shown in Ref. [18].

Since $\varphi_{uz} = \psi$, combining equations (6) and (7), the following can be obtained:

$$\ddot{\varphi}_{rz} = \left[\frac{\dot{V}_{uz}}{V_{uz}} - \frac{2\dot{R}_z}{R_z}\right]\dot{\varphi}_{rz} - \frac{\left(qSc_z^{\beta} - P\right)\dot{R}_z}{mV_{uz}R_z}\beta + \Delta\varphi_{rz}. \tag{8}$$

Therefore, equations (4) and (8) describe the differential expressions of the line-of-sight angle rate of the i-th missile and target in the longitudinal plane and lateral plane, respectively.

2.2. Three-Channel Independent Decoupling Model of the IGC System with Impact Angle Constraint. Through the analysis of the relative motion relationship between the missile and the target, the desired impact angles of the longitudinal plane and the lateral plane are noted as φ_{ry}^{d} and φ_{rz}^{d},

respectively, and the relationship between the current line-of-sight angle, the desired line-of-sight angle, the line-of-sight angle rate, and other state variables is established. The multimissile angle penetration attack is transformed into the problem of line-of-sight angle deviation and attack angle control.

Let the error between the current and the desired line-of-sight angle in the longitudinal plane and the lateral plane be, respectively,

$$\varphi_{ry}^{e} = \varphi_{ry} - \varphi_{ry}^{d}, \tag{9}$$

$$\varphi_{rz}^{e} = \varphi_{rz} - \varphi_{rz}^{d}. \tag{10}$$

By calculating the first derivative and the second derivative on both sides of equations (9) and (10), respectively, it can be seen that

$$\dot{\varphi}_{ry}^{e} = \dot{\varphi}_{ry}, \tag{11}$$

$$\ddot{\varphi}_{ry}^{e} = \ddot{\varphi}_{ry}, \tag{12}$$

$$\dot{\varphi}_{rz}^{e} = \dot{\varphi}_{rz}, \tag{13}$$

$$\ddot{\varphi}_{rz}^{e} = \ddot{\varphi}_{rz}. \tag{14}$$

According to equations (3), (4), (9), (11), and (12), by taking $[\varphi_{ry}^{e}\dot{\varphi}_{ry}^{e}\alpha\omega_z]^T$ as state variables, the subsystem model of the IGC pitch channel of the missile with impact angle constraint can be obtained as

$$\begin{cases} \dot{\varphi}_{ry}^{e} = \dot{\varphi}_{ry}^{e}, \\ \ddot{\varphi}_{ry}^{e} = \left[\dfrac{\dot{V}_{uy}}{V_{uy}} - \dfrac{2\dot{R}_y}{R_y}\right]\dot{\varphi}_{ry}^{e} + \dfrac{\left(qSc_y^{\alpha} + P\right)\dot{R}_y}{mV_{uy}R_y}\alpha + \Delta\varphi_{ry}, \\ \dot{\alpha} = \omega_z - \dfrac{qSc_y^{\alpha} + P}{mV}\alpha + \Delta\alpha, \\ \dot{\omega}_z = \dfrac{qSL}{J_z}\left(m_z^{\alpha}\alpha + m_z^{\delta_z}\delta_z + m_z^{\omega_z}\omega_z\right) + \Delta\omega_z. \end{cases} \tag{15}$$

Similarly, according to equations (7), (8), (10), (13), and (14), by taking $[\varphi_{rz}^{e}\dot{\varphi}_{rz}^{e}\beta\omega_y]^T$ as state variables, the subsystem model of the IGC yaw channel of the missile with impact angle constraint can be obtained as

$$\begin{cases} \dot{\varphi}_{rz}^{e} = \dot{\varphi}_{rz}^{e}, \\ \ddot{\varphi}_{rz}^{e} = \left[\dfrac{\dot{V}_{uz}}{V_{uz}} - \dfrac{2\dot{R}_z}{R_z}\right]\dot{\varphi}_{rz} - \dfrac{\left(qSc_z^{\beta} - P\right)\dot{R}_z}{mV_{uz}R_z}\beta + \Delta\varphi_{rz}, \\ \dot{\beta} = \omega_y + \dfrac{qSc_z^{\beta} - P}{mV}\beta + \Delta\beta, \\ \dot{\omega}_y = \dfrac{qSL}{J_y}\left(m_y^{\beta}\beta + m_y^{\delta_y}\delta_y + m_y^{\omega_y}\omega_y\right) + \Delta\omega_y. \end{cases} \tag{16}$$

Continue to take $[\gamma\omega_x]^T$ as state variables, and the subsystem model of the IGC roll channel of the missile with impact angle constraint can be obtained as

$$\begin{cases} \dot{\gamma} = \omega_x + \Delta\gamma, \\ \dot{\omega}_x = \dfrac{qSL}{J_x}m_x^{\delta_x}\delta_x + \Delta\omega_x. \end{cases} \tag{17}$$

To sum up, equations (15), (16), and (17) constitute the IGC three-channel independent decoupling system model of the missile with impact angle constraint.

3. Robust IGC Control Method for Angle Penetration Attack

The difference between the cooperative IGC model obtained above and the single IGC model described in Ref. [18] is that the single IGC model is a single-output linear time-varying system, while the cooperative IGC model is a multioutput linear time-varying system. At the same time, the missile angle penetration attack not only needs to meet the impact angle constraint but also needs to minimize the attack angle when completing the target attack. Therefore, by taking the subsystem model of the IGC pitch channel in the longitudinal plane as an example, a cooperative robust IGC control method based on the adaptive dynamic surface and nonlinear disturbance observer is designed.

Because the missile needs to meet the requirements of angle penetration attack, the motion of missiles will become more complex, compared with the precise attack flight process of a single missile. At this time, the control limitation of each rudder deflection angle of the missile needs to be considered.

Note the elevator yaw control limit as

$$|\delta_z| \le \delta_{z_{\max}}, \tag{18}$$

where $\delta_{z_{\max}} > 0$.

Define the actual rudder deflection angle of elevator as $\mathrm{real}(\delta_z)$; then,

$$\mathrm{real}(\delta_z) = \begin{cases} \delta_{z_{\max}}, \delta_z \geq \delta_{z_{\max}}, \\ \delta_z, \\ \delta_{z_{\max}}, \delta_z \leq -\delta_{z_{\max}}. \end{cases} \tag{19}$$

Let the state variables $x_1{}' = \varphi_{rz}^e$, $x_2{}' = \dot{\varphi}_{rz}^e$, $x_3{}' = \alpha$, and $x_4{}' = \omega_z$ and the control variable $u = \delta_z$ and $\Delta\varphi_{ry}, \Delta\alpha, \Delta\omega_z$ be recorded as $d_{\varphi_{ry}}, d_\alpha, d_{\omega_z}$, respectively; then, equation (15) can be rewritten into a general state space expression:

$$\begin{cases} \dot{x}_1{}' = f_1{}' + g_1{}' x_2{}', \\ \dot{x}_2{}' = f_2{}' + g_2{}' x_3{}' + d_{\varphi_{ry}}, \\ \dot{x}_3{}' = f_3{}' + g_3{}' x_4{}' + d_\alpha, \\ \dot{x}_4{}' = f_4{}' + g_4{}' \mathrm{real}(\delta_z) + d_{\omega_z}, \end{cases} \tag{20}$$

where

$$\begin{bmatrix} f_1{}' \\ f_2{}' \\ f_3{}' \\ f_4{}' \end{bmatrix} = \begin{bmatrix} 0 \\ \left[\dfrac{\dot{V}_{uy}}{V_{uy}} - \dfrac{2\dot{R}_y}{R_y}\right]\dot{\varphi}_{ry}^e \\ -\dfrac{qSc_y^\alpha + P}{mV}\alpha \\ \dfrac{qSL}{J_z}\left(m_z^\alpha \alpha + m_z^{\omega_z}\omega_z\right) \end{bmatrix}; \begin{bmatrix} g_1{}' \\ g_2{}' \\ g_3{}' \\ g_4{}' \end{bmatrix} = \begin{bmatrix} 1 \\ \dfrac{\left(qSc_y^\alpha + P\right)\dot{R}_y}{mV_{uy}R_y} \\ 1 \\ \dfrac{qSLm_z^{\delta_z}}{J_z} \end{bmatrix}. \tag{21}$$

3.1. Robust IGC Controller Based on the Adaptive Dynamic Surface. For the IGC system model shown in equation (20), which contains unknown uncertainty and has control input constraints, the control goal is to design the controller to make the terminal line-of-sight angle between each missile and the target meet the desired impact angle requirements and ensure that the line-of-sight angle rate tends to zero and meet the requirements of low miss distance.

Before designing the control law, make the following assumptions.

Assumption 1. The system (20) is BIBO stable.

To compensate for the impact of input saturation, the following auxiliary subsystems are established:

$$\begin{cases} \dot{\xi}_1{}' = -h_1{}'\xi_1{}' + \xi_2{}', \xi_1{}'(0) = 0, \\ \dot{\xi}_2{}' = -h_2{}'\xi_2{}' + \xi_3{}', \xi_2{}'(0) = 0, \\ \dot{\xi}_3{}' = -h_3{}'\xi_3{}' + \xi_4{}', \xi_3{}'(0) = 0, \\ \dot{\xi}_4{}' = -h_4{}'\xi_4{}' + g_4{}'\Delta\delta_z, \xi_4{}'(0) = 0, \end{cases} \tag{22}$$

where $h_i{}' > 0 (i = 1, 2, 3, 4)$ and $\Delta\delta_z = \mathrm{real}(\delta_z) - \delta_z$.

The design steps of the dynamic surface are as follows.

Step 1. Define the first dynamic face as

$$s_1{}' = x_1{}' - \xi_1{}'. \tag{23}$$

By deriving from both sides of equation (23) and combining the first equation in equation (20), the following can be obtained:

$$\dot{s}_1{}' = f_1{}' + g_1{}' x_2{}' + h_1{}'\xi_1{}' - \xi_2{}', \tag{24}$$

where $x_2{}'$ is selected as the virtual control variable and designed as

$$x_{2c}{}' = \frac{-f_1{}' - k_1{}' s_1{}' - h_1{}'\xi_1{}' + \xi_2{}'}{g_1{}'}, \tag{25}$$

where $k_1{}'$ is the constant to be set, and it meets that $k_1{}' > 0$. Since $g_1{}' = 1 \neq 0$, $x_{2c}{}'$ is always nonsingular.

$x_{2c}{}'$ is transmitted through the following first-order filter:

$$\tau_2{}'\dot{x}_{2d}{}' + x_{2d}{}' = x_{2c}{}', x_{2d}{}'(0) = x_{2c}{}'(0), \tag{26}$$

where $\tau_2{}'$ is the time constant of the filter.

Step 2. Define the second dynamic face as

$$s_2{}' = x_2{}' - x_{2d}{}' - \xi_2{}'. \tag{27}$$

By deriving from both sides of equation (27) and combining the second equation in equation (20), the following can be obtained:

$$\dot{s}_2{}' = f_2{}' + g_2{}' x_3{}' + d_{\varphi_{ry}} - \dot{x}_{2d}{}' + h_2{}'\xi_2{}' - \xi_3{}', \tag{28}$$

where $x_3{}'$ is selected as the virtual control variable and designed as

$$x_{3c}{}' = \frac{-f_2{}' - k_2{}' s_2{}' - \hat{d}_{\varphi_{ry}} + \dot{x}_{2d}{}' - h_2{}'\xi_2{}' + \xi_3{}'}{g_2{}'}, \tag{29}$$

where $k_2{}'$ is the constant to be set, and it meets that $k_2{}' > 0$; $\hat{d}_{\varphi_{ry}}$ is the estimation of $d_{\varphi_{ry}}$, that is, the output of the subsequently designed nonlinear disturbance observer (NDO). Since $g_2{}' = (qSc_y^\alpha + P)\dot{R}_y/(mV_{uy}R_y) \neq 0$, $x_{3c}{}'$ is always nonsingular.

Similar to $x_{2c}{}'$, $x_{3c}{}'$ is transmitted through the following first-order filter:

$$\tau_3{}'\dot{x}_{3d}{}' + x_{3d}{}' = x_{3c}{}', x_{3d}{}'(0) = x_{3c}{}'(0), \tag{30}$$

where $\tau_3{}'$ is the time constant of the filter.

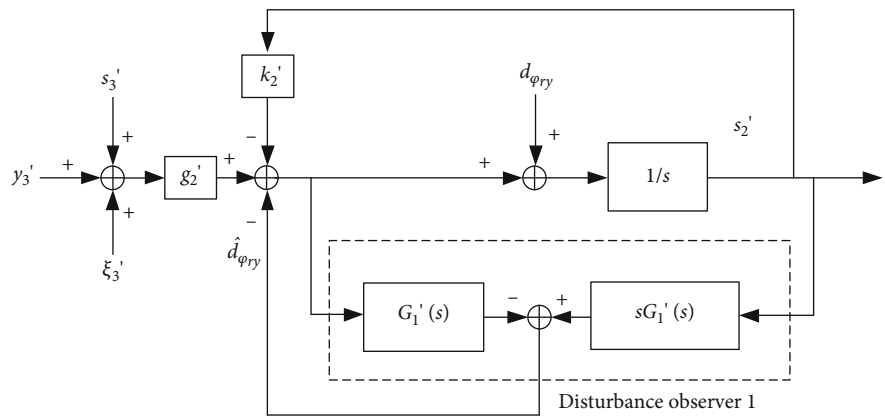

Figure 2: Disturbance observer for estimating $d_{\varphi_{ry}}$.

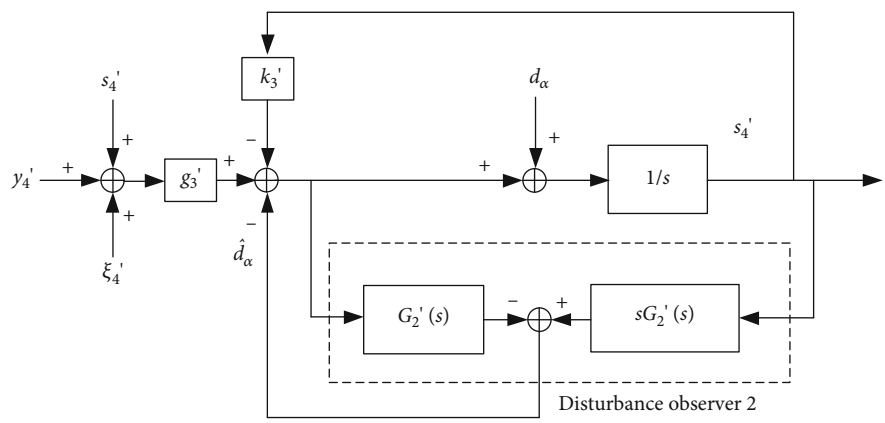

Figure 3: Disturbance observer for estimating d_α.

Step 3. Define the second dynamic face as

$$s_3' = x_3' - x_{3d}' - \xi_3'. \tag{31}$$

By deriving from both sides of equation (31) and combining the third equation in equation (20), the following can be obtained:

$$\dot{s}_3' = f_3' + g_3' x_4' + d_\alpha - \dot{x}_{3d}' + h_3' \xi_3' - \xi_4', \tag{32}$$

where x_4' is selected as the virtual control variable and designed as

$$x_{4c}' = \frac{-f_3' - k_3' s_3' - \hat{d}_\alpha + \dot{x}_{3d}' - h_3' \xi_3' + \xi_4'}{g_3'}, \tag{33}$$

where k_3' is the constant to be set, and it meets that $k_3' > 0$; similar to $\hat{d}_{\varphi_{ry}}$, $\hat{d}_\alpha$ is the estimation of d_α, that is, the output of the subsequently designed nonlinear disturbance observer (NDO). Since $g_3' = 1 \neq 0$, x_{4c}' is always nonsingular.

Similar to x_{2c}' and x_{3c}', x_{4c}' is transmitted through the following first-order filter:

$$\tau_4' \dot{x}_{4d}' + x_{4d}' = x_{4c}', x_{4d}'(0) = x_{4c}'(0), \tag{34}$$

where τ_4' is the time constant of the filter.

Step 4. Define the second dynamic face as

$$s_4' = x_4' - x_{4d}' - \xi_4'. \tag{35}$$

By deriving from both sides of equation (35) and combining the fourth equation in equation (20), the following can be obtained:

$$\begin{aligned} \dot{s}_4' &= f_4' + g_4'(\mathrm{real}(\delta_z) - \Delta\delta_z) + d_{\omega_z} - \dot{x}_{4d}' + h_4' \xi_4' \\ &= f_4' + g_4' \delta_z + d_{\omega_z} - \dot{x}_{4d}' + h_4' \xi_4'. \end{aligned} \tag{36}$$

Then, the actual control input is designed as

$$\delta_z = \frac{-f_4' - k_4' s_4' - \hat{d}_{\omega_z} + \dot{x}_{4d}' - h_4' \xi_4'}{g_4'}, \tag{37}$$

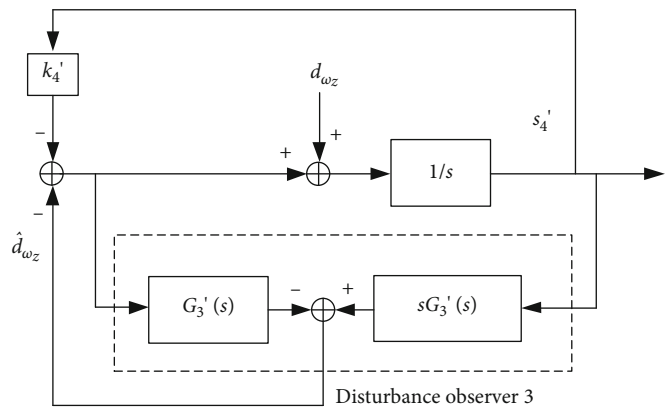

Figure 4: Disturbance observer for estimating d_{ω_z}.

1: For the IGC system mode by Equation (20), define auxiliary subsystems by Equation (22);
2: Design the first dynamic surface by Equation (23);
3: Design the second dynamic surface by Equation (27);
4: Design the third dynamic surface by Equation (31);
5: Design the fourth dynamic surface by Equation (35);
6: Design the first NDO to estimate $d_{\varphi_{ry}}$ by Figure 2;
7: Design the second NDO to estimate d_α by Figure 3;
8: Design the third NDO to estimate d_{ω_z} by Figure 4;
9: The controller work steps are completed.

Pseudocode 1: Controller work steps: robust integrated guidance and control design.

where $k_4{}'$ is the constant to be set, and it meets that $k_4{}' > 0$; similar to $\hat{d}_{\varphi_{ry}}$ and $\hat{d}_\alpha$, $\hat{d}_{\omega_z}$ is the estimation of d_{ω_z}, that is, the output of the subsequently designed nonlinear disturbance observer (NDO). Since $g_4{}' = qSLm_z^{\delta_z}/J_z \neq 0$, δ_z is always nonsingular.

3.2. Nonlinear Disturbance Observer to Dealing with Uncertainty. In this section, three disturbance observers are designed to estimate the uncertainty $d_{\varphi_{ry}}, d_\alpha, d_{\omega_z}$, respectively, in order to enhance robustness of the IGC system.

According to equation (30), the error between filter output and input is defined as

$$y_3{}' = x_{3d}{}' - x_{3c}{}'. \tag{38}$$

Combining equations (31), (38), and (29), we can obtain

$$x_3{}' = s_3{}' + x_{3d}{}' + \xi_3{}' = s_3{}' + y_3{}' + x_{3c}{}' + \xi_3{}' = s_3{}' + y_3{}' + \frac{-f_2{}' - k_2{}'s_2{}' - \hat{d}_{\varphi_{ry}} + \dot{x}_{2d}{}' - h_2\xi_2{}' + \xi_3{}'}{g_2{}'} + \xi_3{}'. \tag{39}$$

Substituting equation (39) into (27), we get

$$\dot{s}_2{}' = -k_2{}'s_2{}' + g_2{}'s_3{}' + g_2{}'y_3{}' + g_2{}'\xi_3{}' - \hat{d}_{\varphi_{ry}} + d_{\varphi_{ry}}. \tag{40}$$

Therefore, according to the design steps of nonlinear disturbance observer in Ref. [18], the observer designed in this section for estimating $d_{\varphi_{ry}}$ is shown in Figure 2.

In Figure 2, the expression of low-pass filter $G_1{}'(s)$ is

$$G_1{}'(s) = \frac{1}{\pi_1{}'s + 1}, \tag{41}$$

where $\pi_1{}'$ is the time constant of the filter. In order to ensure the estimation effect of $d_{\varphi_{ry}}$, the time constant $\pi_1{}'$ should be set small enough.

Similarly, according to equation (34), the error between the filter output and input is defined as

$$y_4{}' = x_{4d}{}' - x_{4c}{}'. \tag{42}$$

Combining equations (35), (42), and (33), we can obtain

$$x_4{}' = s_4{}' + x_{4d}{}' + \xi_4{}' = s_4{}' + y_4{}' + x_{4c}{}' + \xi_4{}' = s_4{}' + y_4{}' + \frac{-f_3{}' - k_3{}'s_3{}' - \hat{d}_\alpha + \dot{x}_{3d}{}' - h_3{}'\xi_3{}' + \xi_4{}'}{g_3{}'} + \xi_4{}'. \tag{43}$$

Table 1: Initial state of missiles and the target.

Object	Position (m)	Velocity (m/s)	Acceleration (m/s^2)	Attack angle (°)	Elevator deflection (°)
Missile A	[020000]	200	0	1.0124	5.6
Missile B	[03000500]	250	0	0.8566	3.7
Missile C	[03000 − 500]	250	0	0.8566	3.7
Target	[500000]	/	/	/	/

Table 2: Desired impact LOS angle and attack angle of missiles.

Object	φ_{ry}^d (°)	φ_{rz}^d (°)	α^d (°)
Missile A	60	0	0.5
Missile B	90	0	0.5
Missile C	90	0	0.5

Table 3: Actual LOS angle, attack angle, and miss distance results at missile impact points.

Object	φ_{ry} (°)	φ_{rz} (°)	α (°)	Miss distance (m)
Missile A	59.07	0.10	0.48	0.0410
Missile B	86.77	0.32	0.56	0.0424
Missile C	87.42	-0.49	0.45	0.0451

Substituting equation (43) into (31), we get

$$\dot{s}_3{}' = -k_3{}' s_3{}' + g_3{}' s_4{}' + g_3{}' y_4{}' + g_3{}' \xi_4{}' - \hat{d}_\alpha + d_\alpha. \quad (44)$$

Therefore, the observer designed in this section for estimating d_α is shown in Figure 3.

In Figure 3, the expression of low-pass filter $G_2{}'(s)$ is:

$$G_2{}'(s) = \frac{1}{\pi_2{}' s + 1} \quad (45)$$

where $\pi_2{}'$ is the time constant of the filter. In order to ensure the estimation effect of d_α, the time constant $\pi_2{}'$ should be set small enough.

Similarly, substituting equation (37) into (35), we can obtain

$$\dot{s}_4{}' = -k_4{}' s_4{}' - \hat{d}_{\omega_z} + d_{\omega_z}. \quad (46)$$

Therefore, the observer designed in this section for estimating d_{ω_z} is shown in Figure 4.

In Figure 4, the expression of low-pass filter $G_3{}'(s)$ is

$$G_3{}'(s) = \frac{1}{\pi_3{}' s + 1}, \quad (47)$$

where $\pi_3{}'$ is the time constant of the filter. In order to ensure the estimation effect of d_{ω_z}, the time constant $\pi_3{}'$ should be set small enough.

To sum up, $\hat{d}_{\varphi_{ry}}$, $\hat{d}_\alpha$, and $\hat{d}_{\omega_z}$ in equations (29), (33), and (37) are obtained by the disturbance observers shown in Figures 2–4, respectively.

The controller work steps are presented in Pseudocode 1.

3.3. Stability Analysis of the Proposed Robust IGC Control Method. The robust IGC control method is designed by using dynamic surface control and nonlinear disturbance observer; then, we analyze the stability of the IGC control method.

The estimation errors of the above three disturbance observers are defined as

$$\begin{aligned} e_1 &= d_{\varphi_{ry}} - \hat{d}_{\varphi_{ry}}, \\ e_2 &= d_\alpha - \hat{d}_\alpha, \\ e_3 &= d_{\omega_z} - \hat{d}_{\omega_z}. \end{aligned} \quad (48)$$

Then, equations (40), (44), and (46) can be written as

$$\dot{s}_2{}' = -k_2{}' s_2{}' + g_2{}' s_3{}' + g_2{}' y_3{}' + g_2{}' \xi_3{}' + e_1, \quad (49)$$

$$\dot{s}_3{}' = -k_3{}' s_3{}' + g_3{}' s_4{}' + g_3{}' y_4{}' + g_3{}' \xi_4{}' + e_2, \quad (50)$$

$$\dot{s}_4{}' = -k_4{}' s_4{}' + e_3. \quad (51)$$

Taking the derivatives on both sides of equations (38) and (42), respectively, and combining equations (30) and (34), the following can be obtained:

$$\dot{y}_3{}' = -\frac{y_3{}'}{\tau_3{}'} + b_3{}', \quad (52)$$

$$\dot{y}_4{}' = -\frac{y_4{}'}{\tau_4{}'} + b_4{}', \quad (53)$$

where $b_i{}' = -\dot{x}_{ic}{}' (i = 3, 4)$ is a continuous function, and its boundedness can be obtained from Assumption 1. Therefore, it can be seen that $|b_i{}'| \le \eta_i{}' (i = 3, 4)$, where $\eta_i{}' (i = 3, 4)$ is the normal number.

The Lyapunov function is defined as

$$L = \frac{s_2{}'^2 + s_3{}'^2 + s_4{}'^2 + y_3{}'^2 + y_4{}'^2 + \xi_2{}'^2 + \xi_3{}'^2 + \xi_4{}'^2}{2}. \quad (54)$$

Taking the derivatives on both sides of equation (54) and

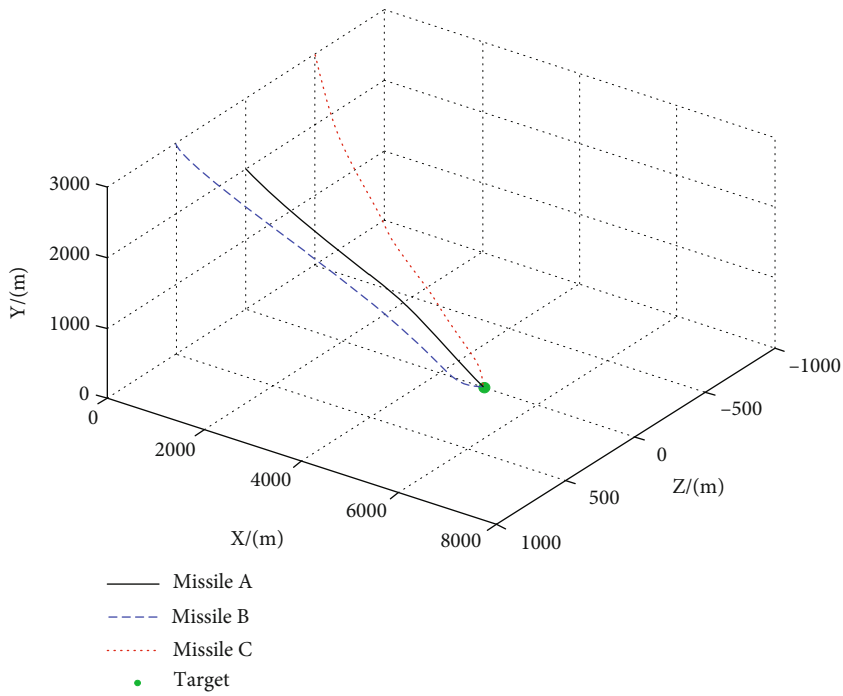

Figure 5: Three-dimensional trajectory of missiles A, B, and C and the target in angle penetration attack.

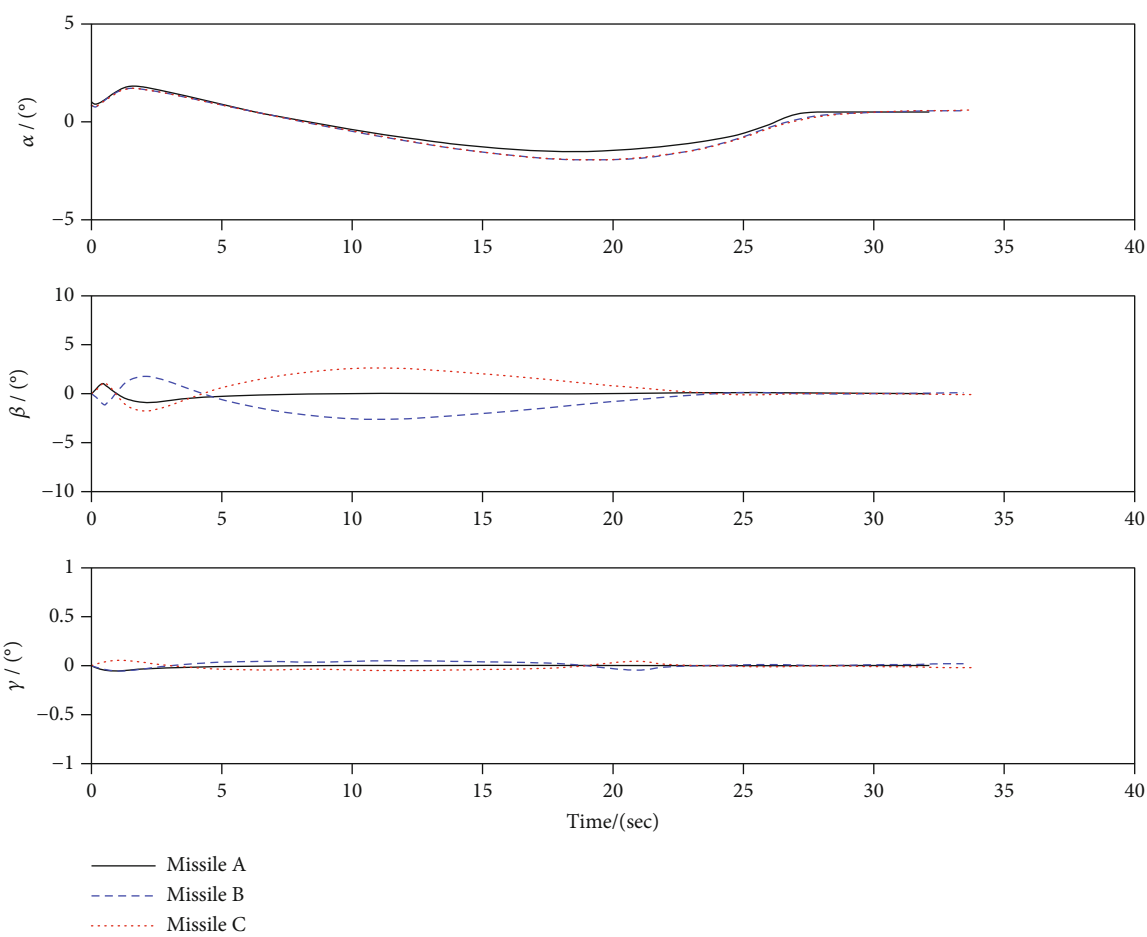

Figure 6: Response curves of the attack angle, sideslip angle, and roll angle of three missiles.

combining equations (49)–(53), the following can be obtained:

$$\begin{aligned}\dot{L} &= s_2'\left(-k_2's_2' + g_2's_3' + g_2'y_3' + g_2'\xi_3' + e_1\right)\\ &\quad + s_3'\left(-k_3's_3' + g_3's_4' + g_3'y_4' + g_3'\xi_4' + e_2\right)\\ &\quad + s_4'\left(-k_4's_4' + e_3\right) + y_3'\left(-\frac{y_3'}{\tau_3'} + b_3'\right)\\ &\quad + y_4'\left(-\frac{y_4'}{\tau_4'} + b_4'\right) + \xi_2'\left(-h_2'\xi_2' + \xi_3'\right)\\ &\quad + \xi_3'\left(-h_3'\xi_3' + \xi_3\right) + \xi_3(-h_3\xi_3 + g_3\Delta\delta_z)\\ &= -k_2's_2'^2 - k_3's_3'^2 - k_4's_4'^2 - \frac{y_3'^2}{\tau_3'} - \frac{y_4'^2}{\tau_4'} - h_2'\xi_2'^2\\ &\quad - h_3'\xi_3'^2 - h_4'\xi_4'^2 + g_2's_2's_3' + g_2's_2'y_3' + g_2's_2'\xi_3'\\ &\quad + s_2'e_1 + g_3's_3's_4' + g_3's_3'y_4' + g_3's_3'\xi_4' + s_3'e_2\\ &\quad + s_4'e_3 + y_3'b_3' + y_4'b_4' + \xi_2'\xi_3' + \xi_3'\xi_4' + g_2'\xi_3'\Delta\delta_z.\end{aligned} \tag{55}$$

According to Young's inequality and $|b_i'| \le \eta_i'\,(i = 3, 4)$, it can be deduced that

$$\begin{aligned}\dot{L} &\le -k_2's_2'^2 - k_3's_3'^2 - k_4's_4'^2 - \frac{y_3'^2}{\tau_3'} - \frac{y_4'^2}{\tau_4'} - h_2'\xi_2'^2\\ &\quad - h_3'\xi_3'^2 - h_4'\xi_4'^2 + \frac{g_2'^2s_2'^2}{4} + s_3'^2 + \frac{g_2'^2s_2'^2}{4} + y_3'^2\\ &\quad + \frac{g_2'^2s_2'^2}{4} + \xi_3'^2 + s_2'^2 + \frac{e_1^2}{4} + \frac{g_3'^2s_3'^2}{4} + s_4'^2\\ &\quad + \frac{g_3'^2s_3'^2}{4} + y_4'^2 + \frac{g_3'^2s_3'^2}{4} + \xi_4'^2 + s_3'^2 + \frac{e_2^2}{4} + s_4'^2\\ &\quad + \frac{e_3^2}{4} + y_3'^2 + \frac{b_3'^2}{4} + y_4'^2 + \frac{b_4'^2}{4} + \frac{\xi_2'^2}{2} + \frac{\xi_3'^2}{2}\\ &\quad + \frac{\xi_3'^2}{2} + \frac{\xi_4'^2}{2} + \frac{\xi_4'^2}{2} + \frac{\left(g_4'\Delta\delta_z\right)^2}{2}.\end{aligned} \tag{56}$$

Further, the following inequality holds:

$$\begin{aligned}\dot{L} &\le -\left(k_2' - \frac{3g_2'^2}{4} - 1\right)s_2'^2 - \left(k_3' - \frac{3g_3'^2}{4} - 2\right)s_3'^2\\ &\quad - \left(k_4' - 2\right)s_4'^2 - \left(h_2' - 0.5\right)\xi_2'^2 - \left(h_3' - 2\right)\xi_3'^2\\ &\quad - \left(h_4' - 2\right)\xi_4'^2 - \left(\frac{1}{\tau_3'} - 2\right)y_3'^2 - \left(\frac{1}{\tau_4'} - 2\right)y_4'^2\\ &\quad + \frac{e_1^2 + e_2^2 + e_3^2}{4} + \frac{\eta_3'^2 + \eta_4'^2}{4} + \frac{g_4'^2\Delta\delta_z^2}{2}.\end{aligned} \tag{57}$$

If the parameters $k_i'\,(i = 2, 3, 4)$ and $\tau_i'\,(i = 3, 4)$ to be set meet the following inequalities,

$$\begin{cases} k_2' - \dfrac{3g_2'^2}{4} - 1 \ge \dfrac{\varsigma}{2}, k_3' - \dfrac{3g_3'^2}{4} - 2 \ge \dfrac{\varsigma}{2}, k_4' - 2 \ge \dfrac{\varsigma}{2},\\ h_2' - 0.5 \ge \dfrac{\varsigma}{2}, h_3' - 2 \ge \dfrac{\varsigma}{2}, h_4' - 2 \ge \dfrac{\varsigma}{2},\\ \dfrac{1}{\tau_3'} - 2 \ge \dfrac{\varsigma}{2}, \dfrac{1}{\tau_4'} - 2 \ge \dfrac{\varsigma}{2},\end{cases} \tag{58}$$

where ς is the normal number.

Combining equations (57) and (58), we can obtain

$$\dot{L} \le \zeta - \varsigma L, \tag{59}$$

where $\zeta = (\eta_3'^2 + \eta_4'^2 + e_1^2 + e_2^2 + e_3^2/4) + (g_4'^2\Delta\delta_z^2/2)$..

From equation (59), we can get

$$\lim_{t\longrightarrow\infty} L \le \frac{\zeta}{\varsigma}. \tag{60}$$

Assuming that the designed disturbance observer can better estimate the uncertainty, it can be seen that

$$\lim_{t\longrightarrow\infty} e_i = 0, \quad i = 1, 2, 3. \tag{61}$$

In the later flight stage of missiles attacking the target, it can be assumed that there is no input saturation; that is, when $t \longrightarrow \infty$, $\Delta\delta_z = 0$ holds. At this time, equation (60) becomes

$$\lim_{t\longrightarrow\infty} L \le \frac{\eta_2^2 + \eta_3^2}{4\varsigma}. \tag{62}$$

From equation (62), it can be seen that the upper bound of L depends on $\eta_i'\,(i = 3, 4)$ and ς. If ς is large enough, L can become arbitrarily small, and s_2', s_3', s_4' and y_3', y_4' are ultimately uniformly bounded.

Since $x_1' = 0$ is one of the control objectives, in order to analyze its transient tracking error, we define

$$L_\xi = \frac{\xi_2'^2 + \xi_3'^2 + \xi_4'^2}{2}. \tag{63}$$

By taking the derivatives on both sides of equation (63), according to Young's inequality, the following can be obtained:

$$\begin{aligned}\dot{L}_\xi &= \sum_{i=2}^{4}\xi_i'\dot{\xi}_i' = -h_2'\xi_2'^2 + \xi_2'\xi_3' - h_3'\xi_3'^2 + \xi_3'\xi_4'\\ &\quad - h_4'\xi_4'^2 + g_4'\xi_4'\Delta\delta_z \le -\left(h_2' - 0.5\right)\xi_2'^2\\ &\quad - \left(h_3' - 1\right)\xi_3'^2 - \left(h_4' - 2\right)\xi_4'^2 + \frac{g_4'^2\Delta\delta_z^2}{2}.\end{aligned} \tag{64}$$

Let $h = \min(h_2' - 0.5, h_3' - 1, h_4' - 2)$; then, equation (64) becomes

$$\dot{L}_\xi \le -h\left(\xi_1^2 + \xi_2^2 + \xi_3^2\right) + \frac{g_3^2 \Delta\delta_z^2}{2}. \tag{65}$$

Taking the derivatives on both sides of equation (65) within $[0, \infty]$, we can obtain

$$L_\xi(\infty) - L_\xi(0) \le -h\int_0^\infty \left(\xi_2'^2 + \xi_3'^2 + \xi_4'^2\right)dt + \frac{1}{2}\int_0^\infty \left(g_4'^2 \Delta\delta_z^2\right)dt. \tag{66}$$

According to equation (66), the following inequality can be obtained:

$$\begin{aligned}\|\xi_2'\|_2^2 &\le -\int_0^\infty \left(\xi_3'^2 + \xi_4'^2\right)dt + \frac{\left(1/2\int_0^\infty \left(g_4'^2 \Delta\delta_z^2\right)dt - L_\xi(\infty) + L_\xi(0)\right)}{h} \\ &\le \frac{\left(1/2\int_0^\infty \left(g_4'^2 \Delta\delta_z^2\right)dt + L_\xi(0)\right)}{h} = \frac{\|g_4' \Delta\delta_z\|_2^2}{2h} + \frac{L_\xi(0)}{h}.\end{aligned} \tag{67}$$

Then, the upper bound of $\|\xi_2'\|_2$ can be expressed as

$$\|\xi_2'\|_2 \le \frac{\|g_4' \Delta\delta_z\|_2}{\sqrt{2h}} + \frac{\sqrt{L_\xi(0)}}{\sqrt{h}}. \tag{68}$$

Similarly, taking the derivatives on both sides of equation (59) within $[0, \infty]$, we can obtain

$$\begin{aligned}L(\infty) - L(0) \le &-\varsigma\int_0^\infty \left(s_2'^2 + s_3'^2 + s_4'^2 + L_\xi + y_3'^2 + y_4'\right)dt \\ &+ \frac{1}{2}\int_0^\infty \left(g_4'^2 \Delta\delta_z^2\right)dt + \frac{1}{4}\int_0^\infty \left(\eta_3'^2 + \eta_4'^2 + s_2'^2 + s_3'^2 + s_4'^2\right)dt.\end{aligned} \tag{69}$$

According to equation (69), the following inequality can be obtained:

$$\begin{aligned}\|s_2'\|_2^2 \le &-\int_0^\infty \left(s_3'^2 + s_4'^2 + L_\xi + y_3'^2 + y_4'^2\right)dt \\ &+ \frac{\left(1/2\int_0^\infty \left(g_4'^2 \Delta\delta_z^2\right)dt - L(\infty) + L(0)\right)}{\varsigma} \\ &+ \frac{1}{4\varsigma}\int_0^\infty \left(\eta_3'^2 + \eta_4'^2 + e_1^2 + e_2^2 + e_3^2\right)dt \\ \le &\frac{\|\eta_3'\|_2^2 + \|\eta_4'\|_2^2 + \|e_1\|_2^2 + \|e_2\|_2^2 + \|e_3\|_2^2}{4\varsigma} \\ &+ \frac{\|g_4' \Delta\delta_z\|_2^2}{2\varsigma} + \frac{L(0)}{\varsigma} \\ \le &\frac{\left(\left(\|\eta_3'\|_2 + \|\eta_4'\|_2 + \|e_1\|_2 + \|e_2\|_2 + \|e_3\|_2\right)/2 + \|g_4' \Delta\delta_z\|_2/\sqrt{2}\right)^2}{\varsigma} \\ &+ \frac{L(0)}{\varsigma}.\end{aligned} \tag{70}$$

Therefore, the following can be obtained:

$$\begin{aligned}\|x_1' - \xi_2'\|_2 &= \|s_2'\|_2 \\ &\le \frac{\left(\left(\|\eta_3'\|_2 + \|\eta_4'\|_2 + \|e_1\|_2 + \|e_2\|_2 + \|e_3\|_2\right)/2 + \|g_4' \Delta\delta_z\|_2/\sqrt{2} + \sqrt{L(0)}\right)}{\sqrt{\varsigma}}.\end{aligned} \tag{71}$$

Combining equations (68) and (71) and making $\xi_i'(0) = 0, (i = 2, 3, 4)$ so that $L_\xi(0) = 0$, we get

$$\begin{aligned}\|x_1'\|_2 \le &\frac{\|\eta_3'\|_2 + \|\eta_4'\|_2 + \|e_1\|_2 + \|e_2\|_2 + \|e_3\|_2}{2\sqrt{\varsigma}} \\ &+ \frac{\|g_4' \Delta\delta_z\|_2}{\sqrt{2\varsigma}} + \frac{\|g_4' \Delta\delta_z\|_2}{\sqrt{2h}}.\end{aligned} \tag{72}$$

Equation (72) gives the explicit expression of the transient tracking error of the desired line-of-sight angle in the longitudinal plane.

According to equations (62) and (72), the following conclusions can be drawn.

Conclusion 2. For the decoupling IGC nonlinear system model of angle penetration attack shown in equation (20) satisfying Assumption 1, the uncertain performance in the system model is effectively estimated by the disturbance observers shown in Figures 2–4. When the dynamic surface (DSC) control method shown in equation (37) is established, and all states s_1', s_2', s_3', s_4' and y_2', y_3', y_4' of the closed-loop system will be ultimately uniformly bounded by setting appropriate parameters. Meanwhile, by increasing the parameter $k_1', k_2', k_3', k_4', h_1', h_2', h_3', h_4'$ and decreasing the parameter $\tau_2', \tau_3', \tau_4'$, the above states will be arbitrarily small. In conclusion, the proposed cooperative IGC design method is stable.

Note 3. In this section, an IGC design method based on the adaptive dynamic surface and nonlinear disturbance observer is designed for the subsystem model of the IGC pitch channel of the missile in the longitudinal plane. For the subsystem model of the IGC yaw channel and roll channel shown in equations (16) and (17), respectively, which contain unknown uncertainties and have input constraints on control inputs δ_z, δ_y and δ_x, the control goal of the yaw channel is to design the controller to make the terminal line-of-sight angle of missile and target meet the requirements of desired impact angle and to ensure that the line-of-sight rate tends to zero and to meet the requirements of low miss distance. The control goal of the roll channel is to minimize the rolling. The controller design still adopts the IGC design method of the adaptive dynamic surface and disturbance observer proposed in this section.

4. Simulation and Analysis

In order to verify the effectiveness and practicability of the IGC design method based on adaptive dynamic surface for

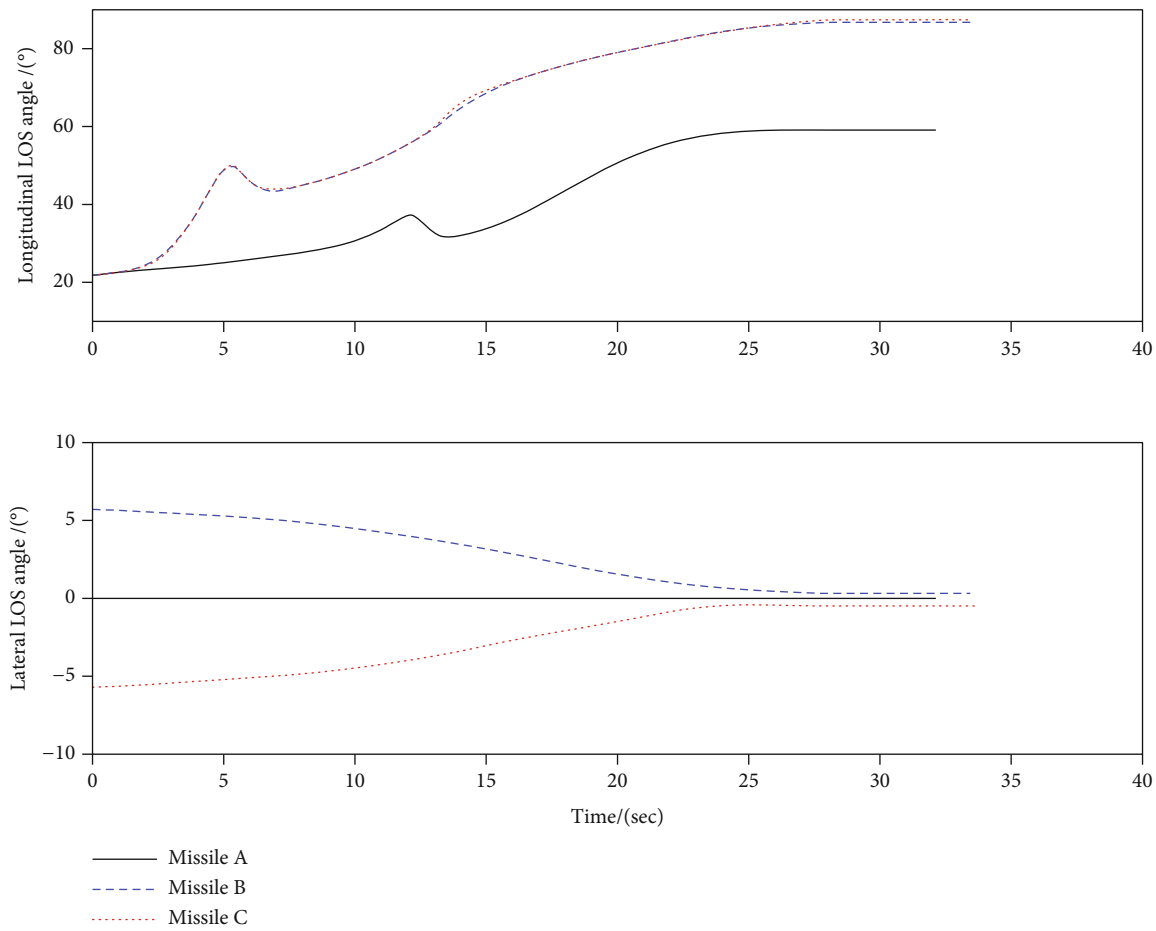

Figure 7: LOS angle curves in the longitudinal plane and lateral plane of three missiles.

multimissiles cooperative attack on battlefield targets, the computer simulation experiments of multimissile angle penetration attack mission are carried out. During the experiment, all simulations use MATLAB R2021a software, and the PC parameters used are Intel i7, 4-Core, 2.40 GHz, 64 bit, and 8 GB RAM.

The simulation scenario is set as that three missiles (missiles A, B, and C) perform the task of attacking ground stationary targets. The initial state and relevant control parameters of each missile and target are set in Table 1.

Except that the initial pitch angle is equal to the attack angle, the attitude angle and angle rate of three missiles are zero, and the initial aileron deflection angle and rudder deflection angle are also zero. Generally, the velocity and mass of three missiles can be regarded as invariants in the whole attack process. There is a fixed perturbation deviation +20% in the aerodynamic parameters of missiles and +20% fixed noise interference in the measurement. The input limits of elevator deflection angle, rudder deflection angle, and aileron deflection angle are ±10°, ±10°, and ±10°, respectively.

The desired terminal impact angle constraints set in the simulation are shown in Table 2. $\varphi_{ry}^{d}, \varphi_{rz}^{d}$ represent the desired impact LOS angle of missiles in the longitudinal plane and lateral plane, respectively; α^{d} is the desired impact attack angle of missiles.

In equation (35), the parameter $h_i{}'$ of the auxiliary subsystem is set as $h_i{}' = 2.5, (i = 1, 2, 3, 4)$, respectively; in equations (25), (29), (33), and (37), the virtual control parameters of the dynamic surface are set as $k_i{}' = 2.5, (i = 1, 2, 3, 4)$, respectively; in equations (26), (30), and (34), the filtering time constants of the first-order filter are, respectively, set as $\tau_i{}' = 0.2\text{s}(i = 2, 3, 4)$; in equations (41), (45), and (47), the filtering time constants of the disturbance observer are, respectively, set as $\pi_i{}' = 0.004\text{s}(i = 1, 2, 3)$.

Table 3 shows the actual impact angle and miss distance of missiles A, B, and C. The curves shown in Figure 5 are the three-dimensional motion trajectories of three missiles and targets, respectively, and three groups of curves shown in Figure 6 are the changes of attack angle, sideslip angle, and roll angle of three missiles, respectively. Two groups of curves shown in Figure 7 represent the change of actual LOS angle in the longitudinal plane and lateral plane of three missiles, respectively, and two groups of curves shown in Figure 8 are the change of LOS angle rate in the longitudinal plane and lateral plane of three missiles, respectively.

According to the simulation results in Table 3 and Figure 5, missiles A, B, and C can intercept the target with

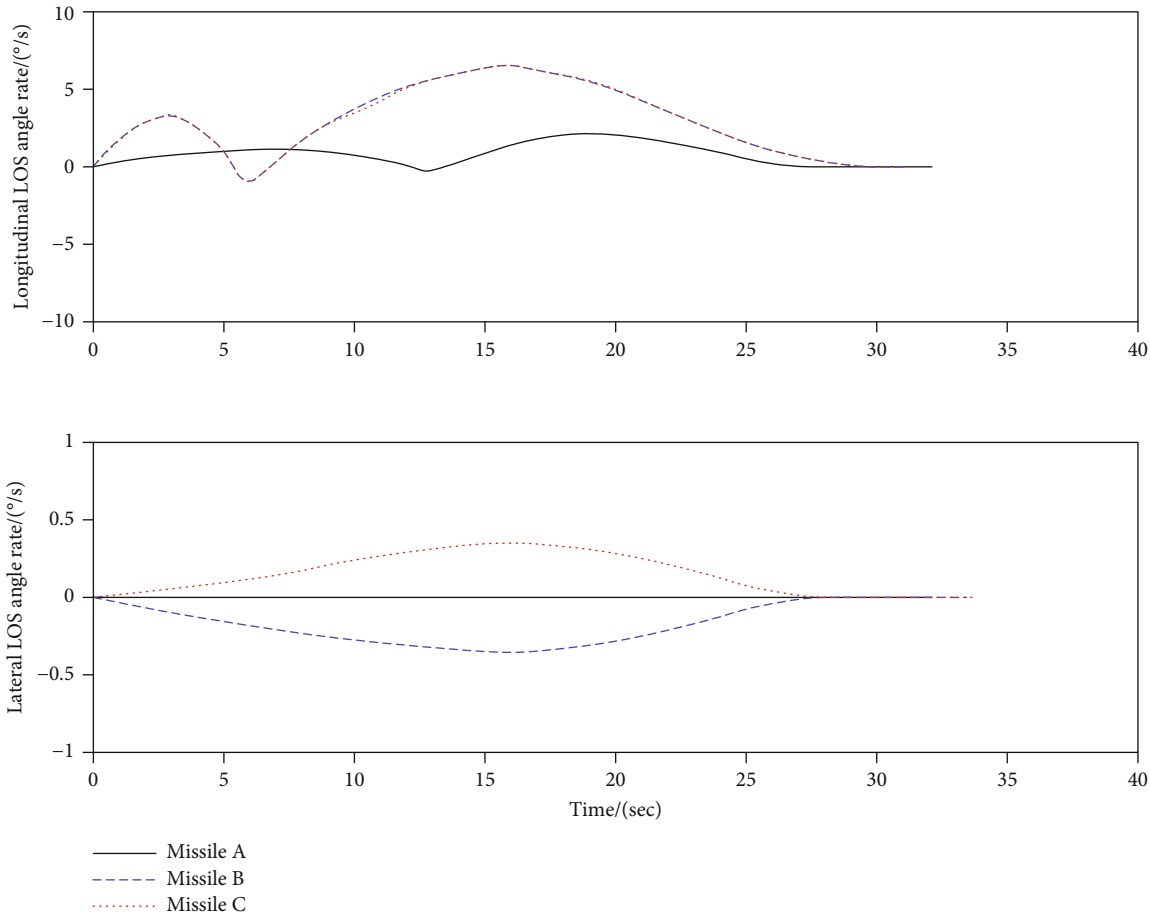

Figure 8: LOS angle rate curves in the longitudinal plane and lateral plane of three missiles.

Table 4: Performance comparison of three algorithms.

Algorithm	Mean miss distance (m)			φ_{ry} (°)		
	Missile A	Missile B	Missile C	Missile A	Missile B	Missile C
Traditional method	1.7322	1.8106	1.8545	45.82	62.19	66.56
SMC method	1.0057	1.0213	1.0388	62.11	84.54	85.71
Proposed method	0.0416	0.0429	0.0462	59.12	86.94	87.63

a small miss distance to achieve accurate attack on the target. Among them, the actual terminal LOS angle in the longitudinal plane of missile A is 59.07°, which differs little from the desired impact angle constraint 60°. The actual terminal LOS angle in the longitudinal plane of missiles B and C are 87.42° and 87.42°, respectively, which is equivalent to reaching the desired impact angle constraint 90° and means that the vertical attack on the target is realized.

According to the simulation results in Figures 5–8, while meeting the constraints of terminal line-of-sight angle, the three missiles can also ensure that each missile can complete the target attack at a sufficiently small attack angle, and the impact attack angles of missiles A, B, and C are 0.48°, 0.56° and 0.45°, respectively, which meets the requirements of angle penetration attack. At the same time, the three missiles maintain a relatively gentle flight state during the flight, which can ensure that the angle rate changes of missiles A, B, and C are maintained in a small range and bear small overload changes.

To compare with existing methods, such as the traditional guidance and control method (traditional method) [12] and sliding mode control method (SMC method) [15], Monte Carlo simulation is used to conduct 100 robustness experiments in the same simulation conditions. The mean miss distance and LOS angle are shown in Table 4.

According to the simulation results in Table 4, missiles A, B, and C can attack the target with small mean miss distance; meanwhile, they can meet with the desired impact angle requirements by using the proposed method in this paper. Both the traditional method and SMC method make big mean miss distance compared with the proposed method. The SMC method can meet with the desired impact

angle requirements, while the traditional method has big error in the desired impact angle. The reason is that the traditional method separates the guidance and control system, which will make a bad impact on the control accuracy and coordination performance. And the SMC method can achieve coordination control with the nonlinear control ability, but it cannot deal with the unknown uncertainty which will deduce some control errors.

5. Conclusions

This paper mainly studies the integrated guidance and control (IGC) design method for multimissile angle penetration attack. According to the requirements of multimissile angle penetration attack, the IGC system model with impact angle constraint is established. Considering the dynamic constraints, nonlinear input saturation, terminal line-of-sight, and attack angle constraints, a robust IGC control method for angle penetration attack is designed based on the adaptive dynamic surface and nonlinear disturbance observer, and the stability of the IGC design method is proven by the Lyapunov theorem. The simulation results show that the method proposed in this paper can not only ensure the accurate attack of each missile on the target but also ensure the coordination of multimissile flight states, meet the terminal impact angle requirement of each missile, and finally realize the multimissile angle penetration attack mission. The paper makes a contribution to the cooperative integrated guidance and control system design, and the research results will benefit practical missions of high-speed UAVs and missiles in the future. The processing of nonlinear uncertainties such as hysteresis and dead time in the control system is the focus of the next research.

Data Availability

The data used to support the findings of this study are included within the article.

Conflicts of Interest

The authors declare no conflict of interest.

Acknowledgments

The authors acknowledge the funding received from the following science foundations: the National Natural Science Foundation of China (Nos. 62101590 and 62176214) and the Natural Science Foundation of Shaanxi Province, China (2020JQ-481, 2019JQ-014).

References

[1] H. Yu, K. Dai, H. Li et al., "Distributed cooperative guidance law for multiple missiles with input delay and topology switching," *Journal of Franklin Institute*, vol. 358, no. 17, pp. 9061–9085, 2021.

[2] P. Zhang and X. Zhang, "Multiple missiles fixed-time cooperative guidance without measuring radial velocity for maneuvering targets interception," *ISA Transations*, 2021, In Press, Available online 17 July 2021.

[3] J. Yu, X. Dong, Q. Li, and Z. Ren, "Cooperative integrated practical time-varying formation tracking and control for multiple missiles system," *Aerospace Science and Technology*, vol. 93, article 105300, 2019.

[4] K. Chen, "Full state constrained stochastic adaptive integrated guidance and control for STT missiles with non-affine aerodynamic characteristics," *Information Sciences*, vol. 529, pp. 42–58, 2020.

[5] I. S. Jeon, J. I. Lee, and M. J. Tahk, "Impact-time-control guidance law for anti-ship missiles," *IEEE Transactitons on Control System Technology*, vol. 14, no. 2, pp. 260–266, 2006.

[6] S. R. Kumar and D. Ghose, "Sliding mode control based guidance law with impact time constrains," in *2013 American Control Conference*, pp. 5760–5765, Washington, DC, USA, June 2013.

[7] I. S. Jeon, J. I. Lee, and M. J. Tahk, "Homing guidance law for cooperative attack of multiple missiles," *Journal of Guidance, Control and Dynamics*, vol. 33, no. 1, pp. 275–280, 2010.

[8] Y. Wang, S. Fan, J. Wang, and G. Wu, "Quick identification of guidance law for an incoming missile using multiple-model mechanism," *Chinese Journal of Aeronautics*, 2021, In Press, Available online 24 November 2021.

[9] N. Harl and S. N. Balakrishnan, "Impact time and angle guidance with sliding mode control," *IEEE Transactions on Control System and Technology*, vol. 20, no. 6, pp. 1436–1449, 2012.

[10] B. Jung and Y. Kim, "Guidance laws for anti-ship missiles using impact angle and impact time," in *AIAA Guidance, Navigation, and Control Conference and Exhibit*, pp. 1–13, Keystone, Colorado, USA, August 2006.

[11] M. Hou, X. Liang, and G. Duan, "Adaptive block dynamic surface control for integrated missile guidance and autopilot," *Chinese Journal of Aeronautics*, vol. 26, no. 3, pp. 741–750, 2013.

[12] C. Ming, X. Wang, and R. Sun, "A novel non-singular terminal sliding mode control-based integrated missile guidance and control with impact angle constraint," *Aerospace Science and Technology*, vol. 94, article 105368, 2019.

[13] J. Zhao and S. Yang, "Integrated cooperative guidance framework and cooperative guidance law for multi-missile," *Chinese Journal of Aeronautics*, vol. 31, no. 3, pp. 546–555, 2018.

[14] X. Shao and H. Wang, "Back-stepping active disturbance rejection control design for integrated missile guidance and control system via reduced-order ESO," *ISA Transacitons*, vol. 57, pp. 10–22, 2015.

[15] T. Shima, M. Idan, and O. M. Golan, "Sliding-mode control for integrated missile autopilot guidance," *Journal of Guidance, Control and Dynamics*, vol. 29, no. 2, pp. 250–260, 2006.

[16] X. Shao and H. Wang, "Active disturbance rejection based trajectory linearization control for hypersonic reentry vehicle with bounded uncertainties," *ISA Transactions*, vol. 54, pp. 27–38, 2015.

[17] D. Swaroop, J. K. Hedrick, P. P. Yip, and J. C. Gerdes, "Dynamic surface control for a class of nonlinear systems," *IEEE Transactions on Automatic Control*, vol. 45, no. 10, pp. 1893–1899, 2000.

[18] W. Bu and Q. Qi, "Fuzzy optimal tracking control of hypersonic flight vehicles via single-network adaptive critic design," *IEEE Transactions on Fuzzy Systems*, vol. 30, no. 1, pp. 270–278, 2022.

[19] Z. Peng, Y. Jiang, and J. Wang, "Event-triggered dynamic surface control of an underactuated autonomous surface vehicle for target enclosing," *IEEE Transactions on Industrial Electronics*, vol. 68, no. 4, pp. 3402–3412, 2021.

[20] X. Bu, Q. Qi, and B. Jiang, "A simplified finite-Time fuzzy neural controller with prescribed performance applied to waverider aircraft," *IEEE Transactions on Fuzzy systems*, vol. 99, pp. 1–9, 2021.

[21] H. Zhou, H. Zhao, H. Huang, and X. Zhao, "Integrated guidance and control design of the suicide UCAV for terminal attack," *Journal of Systems Engineering and Electronics*, vol. 28, no. 3, pp. 546–555, 2017.

[22] H. Huang, X. Zhao, and X. Zhang, "Intelligent guidance and control methods for missile swarm," *Computational Intelligence and Neuroscience*, vol. 2022, Article ID 8235148, 9 pages, 2022.

Hindawi
International Journal of Aerospace Engineering
Volume 2022, Article ID 2486561, 13 pages
https://doi.org/10.1155/2022/2486561

Research Article

Transportation of Payload Using Multiple Quadrotors via Rigid Connection

Ti Chen,[1,2,3] **Jinjun Shan**,[2] **and Hugh H. T. Liu**[3]

[1]*State Key Laboratory of Mechanics and Control of Mechanical Structures, Nanjing University of Aeronautics and Astronautics, 29 Yudao Street, Nanjing, Jiangsu, China 210016*
[2]*Department of Earth and Space Science and Engineering, York University, 4700 Keele Street, Toronto, Ontario, Canada M3J 1P3*
[3]*Institute for Aerospace Studies, University of Toronto, 4925 Dufferin Street, Toronto, Ontario, Canada M3H 5T6*

Correspondence should be addressed to Ti Chen; chenti@nuaa.edu.cn

Received 2 September 2021; Revised 11 February 2022; Accepted 17 March 2022; Published 22 April 2022

Academic Editor: Adel Ghenaiet

Due to the limited payload capability of an aerial robot, multiple quadrotors can be used to manipulate payloads in aerial transportation, construction, and assembly tasks. This paper focuses on the cooperative transportation of a payload rigidly attached to multiple quadrotor bodies. These quadrotors may have different orientations. The dynamics equation of a rigid body in 3-D space is derived to describe the motion of such a transportation system. Robust position and attitude controllers are designed to drive the system to the desired pose. To assign control signals for each quadrotor, the control command allocation method compatible with the case that partial or all quadrotors are in parallel planes is developed. Finally, experimental results are presented to validate the effectiveness of the proposed controllers and control command allocation methods. Different from classical works in this field, this paper can solve the dynamics modeling, controller design, and control command allocation problems for the transportation of a rigidly connected payload using a team of quadrotors with different orientations.

1. Introduction

Due to the advancement in unmanned aerial vehicles and the capabilities of vertical take-off and landing, quadrotors have been implemented in various applications, such as wildfire mapping, search and rescue, payload delivery, and agricultural surveys [1, 2]. As stated in Ref. [3], the market size of the global UAV-assisted logistics and transportation will grow from 5.3 billion dollars in 2019 to about 11 billion dollars by 2026. Several research groups have developed notable algorithms and presented experimental results to prove the quadrotor's ability in payload transportation [4–9]. However, an individual quadrotor usually has limited payload capability. One promising method to address this limitation is to transport a heavy payload using a team of quadrotors. Compared with transportation using a single quadrotor, cooperative transportation has to consider the collaboration and synchronization among quadrotors and the stability of the entire system [4, 10, 11]. Generally, there are mainly two carrying strategies, i.e., connecting the payload to the quadrotor bodies using cables or rigid fixtures. The cooperative transportation of a cable-suspended payload has been studied extensively [12–18]. For example, Sanalitro et al. designed a controller for aerial transportation using the minimum number of quadrotors and cables considering some system uncertainties [14]. Geng and Langelaan presented a centralized load-leading control method for the transportation of a slung payload using multiple rotorcraft to drive the payload to track the desired trajectory [15]. Jiang and Kumar focused on transportation using three aerial robots and proposed an analytic algorithm to solve the possible solution to the kinematics problem based on dialytic elimination [16]. Qian and Liu adopted Kane's method to build the dynamics equation for multiple quadrotors carrying a slung payload and designed a cascade controller to drive the payload to follow the desired path [18]. Generally, it is convenient to attach payload using cables, and the long distances from quadrotors to the payload result in a

negligible influence on the vehicles' aerodynamics. However, the cable-suspended payload introduces additional dynamics. It is usually not possible to add more sensors and actuators to control the oscillations of the payload. Hence, the number of underactuated degrees of freedom increases, and the possible cable slackness will introduce system uncertainties, both of which pose a great challenge in its dynamics modeling and controller design.

To enable direct control of the payload's position and attitude, some rigidly attached methods, such as the manipulators [19–21], graspers [22], and permanent electromagnets [23], have been proposed, and the resulting dynamics, navigation, and control problems have been studied by some scholars. For example, Lee et al. proposed a framework with estimation, control, and path planning for payload transportation using several aerial manipulators based on decentralized dynamics [19]. Mellinger et al. developed control algorithms for a team of quadrotors to grasp and transport a payload in 3-D space based on a dynamics model for the entire system [22]. Loianno and Kumar presented the basic dynamics models, estimation algorithms, and control methods of carrying a payload using multiple quadrotors via permanent electromagnets [23]. To reduce the system complexity, this work mainly focuses on the case with a simple rigidly attached method, such as the permanent magnets. In [22, 23], all n quadrotors are placed in parallel planes, i.e., they are in a special configuration. Essentially, the entire system in such a case can be considered a classical multirotor aircraft with $4n$ propellers. The relative positions of these 4 n propellers vary with different placements of n quadrotors. Hence, the dynamics model of such a transportation system is the same as that of the classical quadrotor, but the command allocation method is different.

However, if the payload surface to be attached is not planar, all propellers of quadrotors may not be in parallel planes, such as the payloads with triangular and quadrangle crosssections shown in Figure 1. In such cases, the orientations of quadrotors are different, i.e., the quadrotors are in a more general configuration than those in [22, 23]. Furthermore, for quadrotors with different orientations, their thrust forces may have some horizontal components, i.e., the horizontal movement of the entire system can be achieved by just increasing or decreasing the thrusts of some quadrotors, which may provide a fast response in the horizontal movement of the entire system. In [24], Ritz and D'Andrea studied the cooperative transportation of a flexible ring using multiple quadrotors with different orientations and some assumptions, such as each quadrotor only providing two control inputs: a force in z direction and a torque in roll direction in its body frame, to simplify the transportation problem. The physical coupling between quadrotors caused by the flexible payload is smaller than that in the case of the transportation of rigid bodies. Hence, essentially, the quadrotors are just considered actuators in [24]. A general framework for the dynamics analysis, controller design, and control command allocation method for the transportation of a rigid payload using multiple quadrotors in different configurations has not been studied yet. This work is aimed at providing a solution to such an open problem. Note that

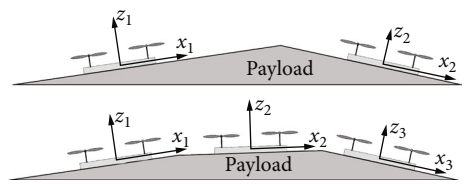

Figure 1: Payload examples.

the relative orientations of the quadrotors in a general configuration are arbitrary under the condition that the lift force generated by quadrotors is larger than the gravity of the entire system. That is, the possible quadrotor configurations of the transportation system in this study have a wider range than those in [22, 23], and the systems in [22, 23] can be called a trivial case. In summary, the main contributions of this study are the following:

(i) The transportation system with quadrotors in various configurations is studied for the first time

(ii) A new dynamics modeling method and the corresponding control algorithm are presented in this work

(iii) A control command allocation method compatible with the case that some or all propellers are in parallel planes is developed

The remainder of this paper is organized as follows. Section 2 presents the dynamics model of the entire transportation system. The designed control law and control command allocation method are given in Section 3. Some experimental results are shown in Section 4. Conclusions are drawn in Section 5.

2. Transportation System Modeling

Suppose that, as shown in Figure 2, there are n identical quadrotors attached to the payload rigidly. Assume that the payload will not affect the aerodynamic forces generated by quadrotors' propellers. $n+2$ frames, i.e., the inertial frame XYZ, the body frame xyz of the entire system, and the body frame $x_iy_iz_i$ of quadrotor i for $i = 1, 2, \cdots, n$, are built to describe the system. The inertial frame is the Earth-fixed West-South-Up frame. The origin of the frame xyz is at the mass center C of the whole system consisting of the payload and the n quadrotors and the frame xyz is parallel with the inertial frame at the initial time. The position vector of C is denoted as $\mathbf{r}_c = [x_c, y_c, z_c]^T$ in the inertial frame. The attitude of the entire system is described by the rotation matrix $\mathbf{R} \in SO(3)$ from the frame xyz to the inertial frame and $\mathbf{R}(0) = \mathbf{I}_3$ holds. Note that the Lie group $SO(3) = \{\mathbf{R} \in \mathbb{R}^{3\times3} | \mathbf{R}^T\mathbf{R} = \mathbf{R}\mathbf{R}^T = \mathbf{I}_3, \det(\mathbf{R}) = 1\}$ represents the group of 3×3 orthogonal matrices with a determinant of one. In the body frame of the entire system, the position of the mass center of the ith quadrotor is represented by $\mathbf{r}_i = [x_i, y_i, z_i]^T$. The rotation matrix from the body frame of the ith quadrotor to the frame xyz is denoted by $\mathbf{R}_i \in SO(3)$.

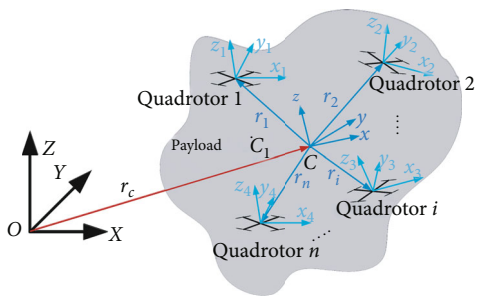

Figure 2: The cooperative transportation system.

Since n quadrotors are attached to the payload rigidly, both $\mathbf{r}_i$ and $\mathbf{R}_i$ are constant.

Essentially, the entire system shown in Figure 2 can be considered an unmanned aerial vehicle driven by $4n$ propellers. Since all quadrotors are in a wide-range configuration, i.e., all propellers may not be in a plane, a three-dimensional control force vector may be generated. Therefore, the dynamics equations of the payload together with these n quadrotors can be written as follows:

$$\dot{\mathbf{r}}_c = \mathbf{v}_c, \tag{1}$$

$$m\dot{\mathbf{v}}_c = -mg\mathbf{z}_I + \mathbf{R}\mathbf{f} + \mathbf{d}_1, \tag{2}$$

$$\dot{\mathbf{R}} = \mathbf{R}\boldsymbol{\Omega}^{\times}, \tag{3}$$

$$\mathbf{J}\dot{\boldsymbol{\Omega}} = -\boldsymbol{\Omega}^{\times}\mathbf{J}\boldsymbol{\Omega} + \tau + \mathbf{d}_2, \tag{4}$$

where $m = m_p + n \times m_q$ is the total mass of the whole system, in which m_p is the payload mass and m_q is the quadrotor mass. $\mathbf{J}$ is the total inertia matrix of the entire system, whose calculation method based on the inertia matrices of the payload and quadrotor and the relative poses of quadrotors with respect to the frame xyz can be found in Appendix A. $\mathbf{v}_c$ is the velocity vector of point C in the inertial frame. g is the constant gravitational acceleration. $\mathbf{z}_I = [0, 0, 1]^T$. $\boldsymbol{\Omega} = [\omega_1, \omega_2, \omega_3]^T$ is the angular velocity in the body frame xyz. Note that for any 3-dimensional vector $\mathbf{z} = [z_1 \quad -z_2 \quad z_3]^T \in \mathbb{R}^3, \mathbf{z}^{\times}$ is defined as the skew-symmetric matrix $[0 \quad -z_3 \quad z_2; z_3 \quad 0 \quad -z_1; -z_2 \quad z_1 \quad 0]$. $\mathbf{d}_1$ and $\mathbf{d}_2$ are unmodeled terms. $\mathbf{f}$ and τ are the total force and torque vectors provided by these n quadrotors expressed in the system body frame xyz. Their detailed definitions are

$$\begin{bmatrix} \mathbf{f} \\ \tau \end{bmatrix} = \sum_{i=1}^{n} \mathbf{A}_i \mathbf{u}_i = \mathbf{A}\mathbf{u}, \tag{5}$$

where

$$\mathbf{A}_i = \begin{bmatrix} \mathbf{R}_i \mathbf{z}_{bi} & \mathbf{0}_{3\times 3} \\ \mathbf{r}_i^{\times} \mathbf{R}_i \mathbf{z}_{bi} & \mathbf{R}_i \end{bmatrix} \in \mathbb{R}^{6\times 4}, \tag{6}$$

$\mathbf{u}_i = [f_i, \tau_i^T]^T \in \mathbb{R}^4$ is the vector consisting of the thrust force and the 3-dimensional control torques of the ith quadrotor, $\mathbf{A} = [\mathbf{A}_1 \quad \mathbf{A}_2 \quad \cdots \quad \mathbf{A}_n] \in \mathbb{R}^{6\times 4n}$ and $\mathbf{u} = [\mathbf{u}_1^T, \mathbf{u}_2^T, \cdots, \mathbf{u}_n^T]^T \in \mathbb{R}^{4n}$. Note that $\mathbf{z}_{bi} = [0, 0, 1]^T$ and $\mathbf{u}_i$ is described in the body frame of the ith quadrotor.

In [22, 23], it is assumed that all quadrotors are in parallel planes for the transportation system consisting of n quadrotors carrying a payload rigidly. Consequently, the dynamics equations are the same as those of the classical quadrotor. The only difference from the classical quadrotor is that more propellers are included to generate the desired control command. It should be noted that the dynamics equations in [22, 23] is still underactuated; hence, the motion in X and Y directions is realized based on the attitude maneuver in roll and pitch directions. However, the quadrotors in the cooperative transportation system considered in this paper can be in any feasible configuration, i.e., all quadrotors may not be in a parallel plane. Consequently, the dynamics equation in Equation (2) is different from the classical quadrotor. The accelerations in X and Y directions may be generated by changing thrust forces of some quadrotors, which implies that maneuvers in X and Y directions are more agile than the classical quadrotor-like system.

The three-dimensional force in the frame xyz provided by the ith quadrotor can be expressed as $\mathbf{R}_i \mathbf{z}_{bi} f_i$. Hence, the total force vector from these n quadrotors expressed in the inertial frame is $\mathbf{R} \cdot \sum_{i=1}^{n} \mathbf{R}_i \mathbf{z}_{bi} f_i$. Essentially, $\mathbf{R} \cdot \mathbf{R}_i$, the rotation matrix from the body frame of the ith quadrotor to the inertial frame, can be written as follows:

$$\mathbf{R} \cdot \mathbf{R}_i = \begin{bmatrix} c_{\bar{\psi}_i} c_{\bar{\theta}_i} & -s_{\bar{\psi}_i} c_{\bar{\phi}_i} + c_{\bar{\psi}_i} s_{\bar{\theta}_i} s_{\bar{\phi}_i} & s_{\bar{\psi}_i} s_{\bar{\phi}_i} + c_{\bar{\psi}_i} s_{\bar{\theta}_i} c_{\bar{\phi}_i} \\ s_{\bar{\psi}_i} c_{\bar{\theta}_i} & c_{\bar{\psi}_i} c_{\bar{\phi}_i} + s_{\bar{\psi}_i} s_{\bar{\theta}_i} s_{\bar{\phi}_i} & -c_{\bar{\psi}_i} s_{\bar{\phi}_i} + s_{\bar{\psi}_i} s_{\bar{\theta}_i} c_{\bar{\phi}_i} \\ -s_{\bar{\theta}_i} & c_{\bar{\theta}_i} s_{\bar{\phi}_i} & c_{\bar{\theta}_i} c_{\bar{\phi}_i} \end{bmatrix}, \tag{7}$$

where s_p and c_p represent sin p and cos p with $p = \bar{\phi}_i, \bar{\theta}_i, \bar{\psi}_i$. Note that $\bar{\phi}_i$, $\bar{\theta}_i$, and $\bar{\psi}_i$ are the roll, pitch, and yaw angles associated with the rotation described by $\mathbf{R} \cdot \mathbf{R}_i$.

Hence, the lift provided by these n quadrotors can be written as $\sum_{i=1}^{n} c_{\bar{\theta}_i} c_{\bar{\phi}_i} f_i$. The forces acting on the system along X and Y axes are $\sum_{i=1}^{n} (s_{\bar{\psi}_i} s_{\bar{\phi}_i} + c_{\bar{\psi}_i} s_{\bar{\theta}_i} c_{\bar{\phi}_i}) f_i$ and $\sum_{i=1}^{n} (-c_{\bar{\psi}_i} s_{\bar{\phi}_i} + s_{\bar{\psi}_i} s_{\bar{\theta}_i} c_{\bar{\phi}_i}) f_i$. One easy way to check whether the whole system can take off successfully is to ensure that $\sum_{i=1}^{n} c_{\bar{\theta}_i} c_{\bar{\phi}_i} f_i^{\max}$ is larger than the system gravity with the roll angle $\bar{\phi}_i$ and pitch angle $\bar{\theta}_i$ in the initial configuration and the maximum thrust $f_i^{\max}$ of each quadrotor. Another important conclusion is that $\bar{\phi}_i$ and $\bar{\theta}_i$ closer to zero will provide a larger lift force. However, in such a case, the forces acting on the system along X and Y axes will tend to zero.

3. Control System Design

This section is aimed at designing a controller with the following assumptions for the system governed by Equations (1)–(4) and presents a command allocation method to realize the desired control command using n quadrotors.

Assumption 1. The time derivative of the possible unmodeled terms $\mathbf{d}_1$ and $\mathbf{d}_2$ is bounded.

The unmodeled terms $\mathbf{d}_1$ and $\mathbf{d}_2$ are mainly from the uncertainty of the actuator model and the modeling error from the measuring errors of inertial parameters and relative pose between quadrotors. For a practical quadrotor transportation system, these modeling errors cannot change with an infinite speed. Hence, it is reasonable to make Assumption 1.

Assumption 2. The control of the payload's position and yaw angle is more significant in the transportation system. Suppose that the desired position vector and yaw angle of the entire system are $\mathbf{r}_d = [x_d, y_d, z_d]$ and ψ_d.

3.1. Position Control. Rewrite dynamics Equation (2) as

$$m\dot{\mathbf{v}}_c = -mg\mathbf{z}_I + \mathbf{f}_d + \mathbf{d}_1, \tag{8}$$

where $\mathbf{f}_d = \mathbf{R}\mathbf{f}$ represents the reference control force command in the inertial frame, i.e., the control command for the system in Equation (2) can be written as $\mathbf{f} = \mathbf{R}^T\mathbf{f}_d$. Consider the following linear extended state observer to estimate unmodeled terms $\mathbf{d}_1$:

$$\begin{aligned}
\dot{\hat{\mathbf{q}}}_1 &= \hat{\mathbf{q}}_2 + 3w_0(\mathbf{r}_c - \hat{\mathbf{q}}_1),\\
\dot{\hat{\mathbf{q}}}_2 &= \hat{\mathbf{q}}_3 + 3w_0^2(\mathbf{r}_c - \hat{\mathbf{q}}_1) + \frac{\mathbf{f}_d}{m} - g\mathbf{z}_I,\\
\dot{\hat{\mathbf{q}}}_3 &= w_0^3(\mathbf{r}_c - \hat{\mathbf{q}}_1),
\end{aligned} \tag{9}$$

where w_0 is a positive observer gain. Letting $\tilde{\mathbf{q}}_1 = \mathbf{r}_c - \hat{\mathbf{q}}_1$, $\tilde{\mathbf{q}}_2 = \dot{\mathbf{r}}_c - \hat{\mathbf{q}}_2$, and $\tilde{\mathbf{q}}_3 = \mathbf{d}_1/m - \hat{\mathbf{q}}_3$ yields

$$\begin{aligned}
\dot{\tilde{\mathbf{q}}}_1 &= \tilde{\mathbf{q}}_2 - 3w_0\tilde{\mathbf{q}}_1,\\
\dot{\tilde{\mathbf{q}}}_2 &= \tilde{\mathbf{q}}_3 - 3w_0^2\tilde{\mathbf{q}}_1,\\
\dot{\tilde{\mathbf{q}}}_3 &= -w_0^3\tilde{\mathbf{q}}_1 + \frac{\dot{\mathbf{d}}_1}{m}.
\end{aligned} \tag{10}$$

The above equation can be rewritten as

$$\dot{\tilde{\mathbf{q}}} = \bar{\mathbf{A}}\tilde{\mathbf{q}} + \bar{\mathbf{d}}, \tag{11}$$

where

$$\begin{aligned}
\tilde{\mathbf{q}} &= \left[\tilde{\mathbf{q}}_1^T, \tilde{\mathbf{q}}_2^T, \tilde{\mathbf{q}}_3^T\right]^T,\\
\bar{\mathbf{d}} &= \left[\mathbf{0}^T, \mathbf{0}^T, \dot{\mathbf{d}}_1^T/m\right],\\
\bar{\mathbf{A}} &= \begin{bmatrix} -3w_0\mathbf{I}_3 & \mathbf{I}_3 & \mathbf{0}\\ -3w_0^2\mathbf{I}_3 & \mathbf{0} & \mathbf{I}_3\\ -w_0^3\mathbf{I}_3 & \mathbf{0} & \mathbf{0}\end{bmatrix}.
\end{aligned} \tag{12}$$

It is easy to verify all eigenvalues of $\mathbf{A}$ are negative with a positive constant w_0, which implies that $\dot{\tilde{\mathbf{q}}} = \bar{\mathbf{A}}\tilde{\mathbf{q}}$ is asymptotically stable. Therefore, with a finite $\bar{\mathbf{d}}$, $\tilde{\mathbf{q}}$ is bounded.

According to [25, 26], one has the following lemma.

Lemma 3 (see [25, 26]). *With Assumption 1 and $w_0 > 0$, $\tilde{\mathbf{q}}_1$, $\tilde{\mathbf{q}}_2$, and $\tilde{\mathbf{q}}_3$ are bounded and there are a constant $\sigma_{i,j} > 0$ and a finite time T_1 such that $|\tilde{q}_{i,j}| \le \sigma_{i,j}$ for any $t > T_1$, where $\tilde{q}_{i,j}$ represents the jth element of $\tilde{\mathbf{q}}_i$ for $i = 1, 2, 3$ and $j = 1, 2, 3$ and $\sigma_{i,j} = O(1/w_0^k)$ for some positive integer k.*

Essentially, $\hat{\mathbf{q}}_1$, $\hat{\mathbf{q}}_2$, and $\hat{\mathbf{q}}_3$ are the estimates of $\mathbf{r}_c$, $\dot{\mathbf{r}}_c$, and $\mathbf{d}_1/m$. Based on the extended state observer, the position controller can be designed as

$$\begin{aligned}
\mathbf{f}_d = {} & mg\mathbf{z}_I - (\mathbf{K}_p + \mathbf{K}_i)(\mathbf{r}_c - \mathbf{r}_d) - \mathbf{K}_i\int_0^t(\mathbf{r}_c - \mathbf{r}_d)dt\\
& - \mathbf{K}_d(\mathbf{v}_c - \dot{\mathbf{r}}_d) + m\ddot{\mathbf{r}}_d - m\hat{\mathbf{q}}_3,
\end{aligned} \tag{13}$$

where $\mathbf{K}_p$, $\mathbf{K}_i$, and $\mathbf{K}_d$ are three diagonal positive definite matrices and $\int_0^t \mathbf{a}dt$ is defined as $\left[\int_0^t a_1 dt, \int_0^t a_2 dt, \int_0^t a_3 dt\right]^T$ for a vector $\mathbf{a} = [a_1, a_2, a_3]^T$.

Theorem 4. *Under the controller $\mathbf{f}_d$ in Equation (13), if these diagonal positive definite matrices $\mathbf{K}_p$, $\mathbf{K}_i$, and $\mathbf{K}_d$ are chosen such that all eigenvalues of*

$$\begin{bmatrix} 0 & \mathbf{I}_3 & 0\\ 0 & 0 & \mathbf{I}_3\\ -\dfrac{\mathbf{K}_i}{m} & -\dfrac{\mathbf{K}_p + \mathbf{K}_i}{m} & -\dfrac{\mathbf{K}_d}{m}\end{bmatrix} \tag{14}$$

have negative real parts, the position tracking error is bounded.

Proof. See Appendix B. □

Remark 5. As shown in the proof of Theorem 4, a large ω_0 will result in a smaller tracking error. However, a too large ω_0 will make the observer sensitive to noise [27]. Hence, ω_0 should be chosen to balance the tracking performance and the noise tolerance.

Remark 6. Theorem 4 presents the stability of the designed position controller, but beyond that, different control gains may result in different system behaviors. This remark is aimed at presenting some tips on how to choose the gains in the designed controller (13). As shown in Equation (B.1), the designed controller can be considered a classical PID controller for a double-integrator system with $(\mathbf{K}_\mathrm{p} + \mathbf{K}_\mathrm{i})$, $\mathbf{K}_\mathrm{d}$, and $\mathbf{K}_\mathrm{i}$ as the proportional, derivative, and integral gains. Hence, the control gains $(\mathbf{K}_\mathrm{p} + \mathbf{K}_\mathrm{i})$, $\mathbf{K}_\mathrm{d}$, and $\mathbf{K}_\mathrm{i}$ can be adjusted according to the PID controller tuning methods.

3.2. Attitude Control. In the last section, to realize the desired control force $\mathbf{f}_\mathrm{d}$, the control force $\mathbf{f}$ can be simply chosen as $\mathbf{f} = \mathbf{R}^T\mathbf{f}_\mathrm{d}$. On the one hand, according to Assumption 2, the attitude maneuver, especially in roll and pitch directions,

in aerial payload transportation is usually not significant. On the other hand, to improve the maneuverability in X and Y directions, the reference rotation matrix can be set as

$$\mathbf{R}_d = \begin{bmatrix} c_{\psi_d}c_{\theta_d} & -s_{\psi_d}c_{\phi_d} + c_{\psi_d}s_{\theta_d}s_{\phi_d} & s_{\psi_d}s_{\phi_d} + c_{\psi_d}s_{\theta_d}c_{\phi_d} \\ s_{\psi_d}c_{\theta_d} & c_{\psi_d}c_{\phi_d} + s_{\psi_d}s_{\theta_d}s_{\phi_d} & -c_{\psi_d}s_{\phi_d} + s_{\psi_d}s_{\theta_d}c_{\phi_d} \\ -s_{\theta_d} & c_{\theta_d}s_{\phi_d} & c_{\theta_d}c_{\phi_d} \end{bmatrix}, \tag{15}$$

where ϕ_d, θ_d, and ψ_d are the desired roll, pitch, and yaw angles satisfying $s_{\phi_d} = f_{d,1}s_{\psi_d} - f_{d,2}c_{\psi_d}/\|\mathbf{f}_d\|$ and $\tan\theta_d = f_{d,1}c_{\psi_d} + f_{d,2}s_{\psi_d}/f_{d,3}$. Note that $f_{d,i}$ represents the ith element of $\mathbf{f}_d$. For such a transportation system, it is reasonable to assume that both roll and pitch angles belong to $(-\pi/2, \pi/2)$. Hence, ϕ_d and θ_d can be set as $\phi_d = \arcsin\left(f_{d,1}s_{\psi_d} - f_{d,2}c_{\psi_d}/\|\mathbf{f}_d\|\right)$ and $\theta_d = \arctan\left(f_{d,1}c_{\psi_d} + f_{d,2}s_{\psi_d}/f_{d,3}\right)$, respectively. It should be noted that ψ_d is the desired yaw angle defined according to the mission requirement. The method to define the desired attitude is the same as the one for a classical quadrotor. Hence, based on such a desired attitude, the proposed control method is compatible with the transportation mission with partial or all quadrotors in parallel planes.

To estimate the unmodeled attitude dynamics, the following observer is designed as

$$\begin{aligned} \dot{\widehat{\mathbf{\Omega}}} &= 2\Gamma\left(\mathbf{\Omega} - \widehat{\mathbf{\Omega}}\right) - \mathbf{J}^{-1}\mathbf{\Omega}\times\mathbf{J}\mathbf{\Omega} + \mathbf{J}^{-1}\tau + \widehat{\mathbf{d}}_2, \\ \dot{\widehat{\mathbf{d}}}_2 &= \Gamma^2\left(\mathbf{\Omega} - \widehat{\mathbf{\Omega}}\right), \end{aligned} \tag{16}$$

where Γ is a positive constant. Letting $\mathbf{e}_\Omega = \mathbf{\Omega} - \widehat{\mathbf{\Omega}}$ and $\mathbf{e}_{d2} = \mathbf{J}^{-1}\mathbf{d}_2 - \widehat{\mathbf{d}}_2$ yields

$$\dot{\mathbf{e}}_\Omega = -2\Gamma\mathbf{e}_\Omega + \mathbf{e}_{d2}, \tag{17}$$

$$\dot{\mathbf{e}}_{d2} = \mathbf{J}^{-1}\dot{\mathbf{d}}_2 - \Gamma^2\mathbf{e}_\Omega. \tag{18}$$

According to Theorem 2.2 in [28], one can have the following lemma.

Lemma 7. *With Assumption 1 and $\Gamma > 0$, $\mathbf{e}_\Omega$ and $\mathbf{e}_{d2}$ are convergent in the sense that for any $\sigma_\omega \in (0, 1)$, there exists $\varepsilon_\sigma \in (0, 1)$ such that $|e_{\Omega,i}| < \sigma_\omega$ and $|e_{d2,i}| < \sigma_\omega$ hold for any $\varepsilon_1 \in (0, \varepsilon_\sigma)$ and any $t \in (T_\varepsilon, \infty)$, where $T_\varepsilon > 0$ depends on ε_1 and $e_{\Omega,i}$, where $e_{\Omega,i}$ and $e_{d2,i}$ are the ith elements of $\mathbf{e}_\Omega$ and $\mathbf{e}_{d2}$, respectively.*

To track the desired attitude $\mathbf{R}_d$, a robust controller is designed as follows:

$$\tau = \mathbf{\Omega}^\times\mathbf{J}\mathbf{\Omega} - k_R\mathbf{e}_R - k_\Omega\mathbf{E}_\Omega + \mathbf{J}\dot{\mathbf{\Omega}}_d - \mathbf{J}\widehat{\mathbf{d}}_2, \tag{19}$$

where $\mathbf{e}_R = \left(\mathbf{R}_d^T\mathbf{R} - \mathbf{R}^T\mathbf{R}_d\right)^\vee$ and $\mathbf{E}_\Omega = \mathbf{\Omega} - \mathbf{\Omega}_d$. Note that $\dot{\mathbf{e}}_R = \left(-\mathbf{\Omega}_d^\times\mathbf{R}_d^T\mathbf{R} + \mathbf{R}_d^T\mathbf{R}\mathbf{\Omega}^\times + \mathbf{\Omega}^\times\mathbf{R}^T\mathbf{R}_d - \mathbf{R}^T\mathbf{R}_d\mathbf{\Omega}_d^\times\right)^\vee = (\mathrm{trace}(\mathbf{R}^T\mathbf{R}_d)\mathbf{I} - \mathbf{R}^T\mathbf{R}_d)\mathbf{\Omega} - (\mathrm{trace}(\mathbf{R}_d^T\mathbf{R})\mathbf{I} - \mathbf{R}_d^T\mathbf{R})\mathbf{\Omega}_d = (\mathrm{trace}(\mathbf{R}^T\mathbf{R}_d)\mathbf{I} - \mathbf{R}^T\mathbf{R}_d)\mathbf{E}_\Omega + \mathbf{e}_R^\times\mathbf{E}_\Omega$. $\widehat{\mathbf{d}}_2$ is the estimate of the unknown term $\mathbf{J}^{-1}\mathbf{d}_2$ and updated according to the law in Equation (17).

Theorem 8. *If $0 < \mu < \sqrt{k_R\lambda_{\min}(\mathbf{J})/2}$ holds and*

$$\begin{bmatrix} k_R\mu\lambda_{\min}\left(\mathbf{J}^{-1}\right) & -\dfrac{k_\Omega\mu\lambda_{\max}\left(\mathbf{J}^{-1}\right)}{2} \\ -\dfrac{k_\Omega\mu\lambda_{\max}\left(\mathbf{J}^{-1}\right)}{2} & (k_\Omega - 2\mu) \end{bmatrix} \tag{20}$$

is positive definite, the attitude tracking error is bounded with the designed controller exponentially almost globally.

Proof. See Appendix C. □

Remark 9. As shown in the proof of Theorem 8, the bounded stability of the system governed by Equation (C.2) is almost globally exponential, i.e., there may exist some undesired equilibria satisfying $\cos\Theta = -1$. According to [29], these undesired critical points are unstable. In a practical system, the ubiquitous noise can drive the system to leave these unstable equilibria.

3.3. Control Command Allocation. Suppose that the desired six-dimensional control command for the rigid body governed by Equations (1)–(4) is $\left[\mathbf{f}, \tau^T\right]^T$. The rotation matrix $\mathbf{R}_i$ from the ith quadrotor's body frame to the body frame of the entire system can be written as

$$\mathbf{R}_i = \begin{bmatrix} c_{\psi_i}c_{\theta_i} & -s_{\psi_i}c_{\phi_i} + c_{\psi_i}s_{\theta_i}s_{\phi_i} & s_{\psi_i}s_{\phi_i} + c_{\psi_i}s_{\theta_i}c_{\phi_i} \\ s_{\psi_i}c_{\theta_i} & c_{\psi_i}c_{\phi_i} + s_{\psi_i}s_{\theta_i}s_{\phi_i} & -c_{\psi_i}s_{\phi_i} + s_{\psi_i}s_{\theta_i}c_{\phi_i} \\ -s_{\theta_i} & c_{\theta_i}s_{\phi_i} & c_{\theta_i}c_{\phi_i} \end{bmatrix}, \tag{21}$$

where ϕ_i, θ_i, and ψ_i are the roll, pitch, and yaw angles associated with the rotation $\mathbf{R}_i$.

To determine the control inputs for each quadrotor, one can minimize the following cost function

$$J_c = \mathbf{u}^T\mathbf{W}\mathbf{u} \tag{22}$$

with the following equation constraint

$$\mathbf{A}\mathbf{u} = \left[\mathbf{f}, \tau^T\right]^T, \tag{23}$$

where $\mathbf{W} = \mathrm{diag}\{\mathbf{w}_i\} \in \mathbb{R}^{4n\times 4n}$ is the weight matrix, in which $\mathbf{w}_i = \mathrm{diag}\{w_{i,j}\}$ with $w_{i,j} > 0$ for $i = 1, 2, \cdots, n$ and $j = 1, 2, 3, 4$. Essentially, this is a constrained quadratic problem, whose solution is

$$\mathbf{u} = \mathbf{K}^+\left[f, \tau^T\right]^T, \tag{24}$$

where $\mathbf{K}^{+} = \mathbf{W}^{-1}\mathbf{A}^{T}\left(\mathbf{A}\mathbf{W}^{-1}\mathbf{A}^{T}\right)^{-1}$. Note that $\mathbf{A}\mathbf{W}^{-1}\mathbf{A}^{T}$ can be written as $\sum_{i=1}^{n}\mathbf{A}_i\mathbf{w}_i^{-1}\mathbf{A}_i^{T}$. Some special cases are discussed below.

Case 1. The weight matrix $\mathbf{w}_i$ is chosen the same for each quadrotor, and the weights in roll, pitch, and yaw directions are equal. Hence, $\mathbf{w}_i$ can be rewritten as diag $\{w_1, w_2, w_2, w_2\}$. Since each quadrotor's payload capability is limited, to improve the payload capability of the quadrotor group in a transportation mission, it is desirable that both ϕ_i and θ_i are small enough such that $\cos\phi_i \approx 1$, $\cos\theta_i \approx 1$, $\sin\phi_i \approx \phi_i$, $\sin\theta_i \approx \theta_i$, $\phi_i^2 \approx 0$, $\theta_i^2 \approx 0$, and $\phi_i\theta_i \approx 0$ hold. Hence, $\mathbf{A}_i\mathbf{w}_i^{-1}\mathbf{A}_i^{T}$ can be written as

$$\mathbf{A}_i\mathbf{w}_i^{-1}\mathbf{A}_i^{T} = \begin{bmatrix} \mathbf{0}_{2\times2} & \mathbf{h}_1 & \mathbf{0}_{2\times1} \\ \mathbf{h}_1^{T} & \mathbf{h}_2 & \mathbf{h}_3 \\ \mathbf{0}_{1\times2} & \mathbf{h}_3^{T} & h_4 \end{bmatrix}, \tag{25}$$

where

$$\mathbf{h}_1 = \begin{bmatrix} \dfrac{c_{\psi_i}\theta_i + s_{\psi_i}\phi_i}{w_1} & \dfrac{y_i\left(c_{\psi_i}\theta_i + s_{\psi_i}\phi_i\right)}{w_1} & -\dfrac{x_i\left(c_{\psi_i}\theta_i + s_{\psi_i}\phi_i\right)}{w_1} \\ -\dfrac{c_{\psi_i}\phi_i - s_{\psi_i}\theta_i}{w_1} & -\dfrac{y_i\left(c_{\psi_i}\phi_i - s_{\psi_i}\theta_i\right)}{w_1} & \dfrac{x_i\left(c_{\psi_i}\phi_i - s_{\psi_i}\theta_i\right)}{w_1} \end{bmatrix},$$

$$\mathbf{h}_2 = \begin{bmatrix} w_1^{-1} & \dfrac{c_{\psi_i}\phi_i z_i - s_{\psi_i}\theta_i z_i + y_i}{w_1} & \dfrac{c_{\psi_i}\theta_i z_i + s_{\psi_i}\phi_i z_i - x_i}{w_1} \\ \dfrac{c_{\psi_i}\phi_i z_i - s_{\psi_i}\theta_i z_i + y_i}{w_1} & \dfrac{2\,c_{\psi_i}\phi_i w_2 y_i z_i - 2\,s_{\psi_i}\theta_i w_2 y_i z_i + w_2 y_i^{2} + w_1}{w_1 w_2} & -\dfrac{c_{\psi_i}\phi_i x_i z_i - c_{\psi_i}\theta_i y_i z_i - s_{\psi_i}\phi_i y_i z_i - s_{\psi_i}\theta_i x_i z_i + x_i y_i}{w_1} \\ \dfrac{c_{\psi_i}\theta_i z_i + s_{\psi_i}\phi_i z_i - x_i}{w_1} & -\dfrac{c_{\psi_i}\phi_i x_i z_i - c_{\psi_i}\theta_i y_i z_i - s_{\psi_i}\phi_i y_i z_i - s_{\psi_i}\theta_i x_i z_i + x_i y_i}{w_1} & -\dfrac{2\,c_{\psi_i}\theta_i w_2 x_i z_i + 2\,s_{\psi_i}\phi_i w_2 x_i z_i - w_2 x_i^{2} - w_1}{w_1 w_2} \end{bmatrix},$$

$$\mathbf{h}_3 = \begin{bmatrix} -\dfrac{c_{\psi_i}\phi_i x_i + c_{\psi_i}\theta_i y_i + s_{\psi_i}\phi_i y_i - s_{\psi_i}\theta_i x_i}{w_1} \\ -\dfrac{y_i\left(c_{\psi_i}\phi_i x_i + c_{\psi_i}\theta_i y_i + s_{\psi_i}\phi_i y_i - s_{\psi_i}\theta_i x_i\right)}{w_1} \\ \dfrac{x_i\left(c_{\psi_i}\phi_i x_i + c_{\psi_i}\theta_i y_i + s_{\psi_i}\phi_i y_i - s_{\psi_i}\theta_i x_i\right)}{w_1} \end{bmatrix},$$

$$h_4 = w_2^{-1}. \tag{26}$$

It should be noted that the determinant of $\mathbf{A}_i\mathbf{w}_i^{-1}\mathbf{A}_i^{T}$ is equal to zero, which implies that only one quadrotor cannot generate the six-dimensional control command based on the equipped four propellers. If there are four quadrotors in the team with $\phi_1 = 0.1$ rad, $\phi_2 = -0.05$ rad, $\phi_3 = \phi_4 = 0$, $\theta_1 = \theta_2 = 0$, $\theta_3 = 0.1$ rad, $\theta_4 = -0.05$ rad, $\psi_1 = \psi_2 = \psi_3 = \psi_4 = 0$, $x_1 = -x_2 = 1$, $x_3 = x_4 = 0$, $y_1 = y_2 = 0$, $y_3 = -y_4 = 1$, $z_1 = z_2 = z_3 = z_4 = 0$, and $w_1 = w_2 = 1$, the determinant of $\sum_{i=1}^{4}\mathbf{A}_i\mathbf{w}_i^{-1}\mathbf{A}_i^{T}$ is 0.01, which implies that these four quadrotors can provide both three-dimensional forces and three-dimensional torques. However, if letting $\theta_3 = \theta_4 = 0$ and keeping all remaining parameters the same as those in the previous sentence, $\sum_{i=1}^{4}\mathbf{A}_i\mathbf{w}_i^{-1}\mathbf{A}_i^{T}$ will be irreversible, i.e., the six-dimensional control command cannot be provided if two quadrotors are in a parallel plane for such a four-quadrotor team. Hence, to improve the compatibility of Equation (24), a new control command allocation method is defined as follows:

$$\mathbf{u} = \begin{cases} \mathbf{W}^{-1}\mathbf{A}^{T}\left(\mathbf{A}\mathbf{W}^{-1}\mathbf{A}^{T}\right)^{-1}\left[\mathbf{f}^{T}, \tau^{T}\right]^{T}, & \text{if } \mathrm{Det}\left(\mathbf{A}\mathbf{W}^{-1}\mathbf{A}^{T}\right) > \varepsilon, \\ \mathbf{W}^{-1}\mathbf{A}^{T}\left(\mathbf{A}\mathbf{W}^{-1}\mathbf{A}^{T} + \delta\mathbf{I}_6\right)^{-1}\left[\mathbf{f}^{T}, \tau^{T}\right]^{T}, & \text{otherwise}, \end{cases} \tag{27}$$

where ε and δ are small positive constants.

Case 2. If the x_iy_i plane in the body frame $x_iy_iz_i$ is parallel to xy plane in the frame xyz, $\phi_i = 0$ and $\theta_i = 0$ hold for each quadrotor and

$$\mathbf{A}_i = \begin{bmatrix} \mathbf{0}_{2\times 4} \\ \widehat{\mathbf{A}}_i \end{bmatrix}, \tag{28}$$

where $\widehat{\mathbf{A}}_i$ is

$$\widehat{\mathbf{A}}_i = \begin{bmatrix} 1 & 0 & 0 & 0 \\ y_i & c_{\psi_i} & -s_{\psi_i} & 0 \\ -x_i & s_{\psi_i} & c_{\psi_i} & 0 \\ 0 & 0 & 0 & 1 \end{bmatrix}. \tag{29}$$

Hence, $\mathbf{A}_i \mathbf{w}_i^{-1} \mathbf{A}_i^T$ is

$$\mathbf{A}_i \mathbf{w}_i^{-1} \mathbf{A}_i^T = \begin{bmatrix} 0 & 0 & 0 & 0 & 0 & 0 \\ 0 & 0 & 0 & 0 & 0 & 0 \\ 0 & 0 & w_1^{-1} & \frac{y_i}{w_1} & -\frac{x_i}{w_1} & 0 \\ 0 & 0 & \frac{y_i}{w_1} & \frac{w_2 y_i^2 + w_1}{w_1 w_2} & -\frac{x_i y_i}{w_1} & 0 \\ 0 & 0 & -\frac{x_i}{w_1} & -\frac{x_i y_i}{w_1} & \frac{w_2 x_i^2 + w_1}{w_1 w_2} & 0 \\ 0 & 0 & 0 & 0 & 0 & w_2^{-1} \end{bmatrix}. \tag{30}$$

The nonzero block matrix in the bottom right corner agrees with the matrix format in [22], where the aerial transportation using quadrotors in parallel planes is studied. In fact, the case in [22] is a special case of the general transportation configuration in Figure 2. If the assumption that the quadrotors are much heavier than the payload in [22] holds, $\mathbf{A}\mathbf{W}^{-1}\mathbf{A}^T$ would be

$$\mathbf{A}\mathbf{W}^{-1}\mathbf{A}^T = \begin{bmatrix} 0 & 0 & 0 & 0 & 0 & 0 \\ 0 & 0 & 0 & 0 & 0 & 0 \\ 0 & 0 & \frac{n}{w_1} & 0 & 0 & 0 \\ 0 & 0 & 0 & \sum_{i=1}^{n} \frac{w_2 y_i^2 + w_1}{w_1 w_2} & 0 & 0 \\ 0 & 0 & 0 & 0 & \sum_{i=1}^{n} \frac{w_2 x_i^2 + w_1}{w_1 w_2} & 0 \\ 0 & 0 & 0 & 0 & 0 & \frac{n}{w_2} \end{bmatrix}. \tag{31}$$

It is clear that the matrix in the above equation is singular. Based on Equation (27), $\mathbf{A}^T(\mathbf{A}\mathbf{W}^{-1}\mathbf{A}^T + \delta\mathbf{I}_6)^{-1}$ can be written as

$$\begin{bmatrix} \mathbf{A}_1 \left(\mathbf{A}\mathbf{W}^{-1}\mathbf{A}^T + \delta\mathbf{I}_6\right)^{-1} \\ \cdots \\ \mathbf{A}_n \left(\mathbf{A}\mathbf{W}^{-1}\mathbf{A}^T + \delta\mathbf{I}_6\right)^{-1} \end{bmatrix}, \tag{32}$$

where

$$\begin{aligned} \mathbf{A}_i \left(\mathbf{A}\mathbf{W}^{-1}\mathbf{A}^T + \delta\mathbf{I}_6\right)^{-1} &= \begin{bmatrix} \mathbf{0}_{4\times 2} & \widehat{\mathbf{A}}_i^T \end{bmatrix} \left(\operatorname{diag}\left\{ 0, 0, \frac{n}{w_1}, \sum_{i=1}^{n} \frac{w_2 y_i^2 + w_1}{w_1 w_2}, \sum_{i=1}^{n} \frac{w_2 x_i^2 + w_1}{w_1 w_2}, \frac{n}{w_2} \right\} + \delta\mathbf{I}_6 \right)^{-1} \\ &\approx \begin{bmatrix} \mathbf{0}_{4\times 2} & \widehat{\mathbf{A}}_i^T \left(\operatorname{diag}\left\{ \frac{n}{w_1}, \sum_{i=1}^{n} \frac{w_2 y_i^2 + w_1}{w_1 w_2}, \sum_{i=1}^{n} \frac{w_2 x_i^2 + w_1}{w_1 w_2}, \frac{n}{w_2} \right\} \right)^{-1} \end{bmatrix}. \end{aligned} \tag{33}$$

Let f_3 be the third element of $\mathbf{f}$. $\mathbf{A}_i(\mathbf{A}\mathbf{W}^{-1}\mathbf{A}^T + \delta\mathbf{I}_6)^{-1} [\mathbf{f}^T, \tau^T]^T$ can be written as

$$\widehat{\mathbf{A}}_i^T \left(\operatorname{diag}\left\{ \frac{n}{w_1}, \sum_{i=1}^{n} \frac{w_2 y_i^2 + w_1}{w_1 w_2}, \sum_{i=1}^{n} \frac{w_2 x_i^2 + w_1}{w_1 w_2}, \frac{n}{w_2} \right\} \right)^{-1} \left[f_3, \tau^T \right]^T, \tag{34}$$

which agrees with the result from the method in [22].

Another interesting point is that both $\mathbf{W}^{-1}\mathbf{A}^T(\mathbf{A}\mathbf{W}^{-1}\mathbf{A}^T)^{-1}$ and $\mathbf{W}^{-1}\mathbf{A}^T(\mathbf{A}\mathbf{W}^{-1}\mathbf{A}^T + \delta\mathbf{I}_6)^{-1}$ are only determined by the relative pose of quadrotors with respect to the payload. Hence, it can be calculated in advance in a transportation task. In other words, the control command for each quadrotor is obtained just from the product of a constant matrix and a six-dimensional control input vector.

In conclusion, the method to calculate the control command for each quadrotor presented in this study is illustrated by Figure 3. With the position vector of the mass center of the entire system and the desired transportation destination, Equation (13) will provide the value of $\mathbf{f}_d$, based on which the reference attitude of the entire system and the control force in Equation (2) can be obtained. With the attitude command from Equation (19), the control command allocation algorithm in Equation (27) provides a 4-

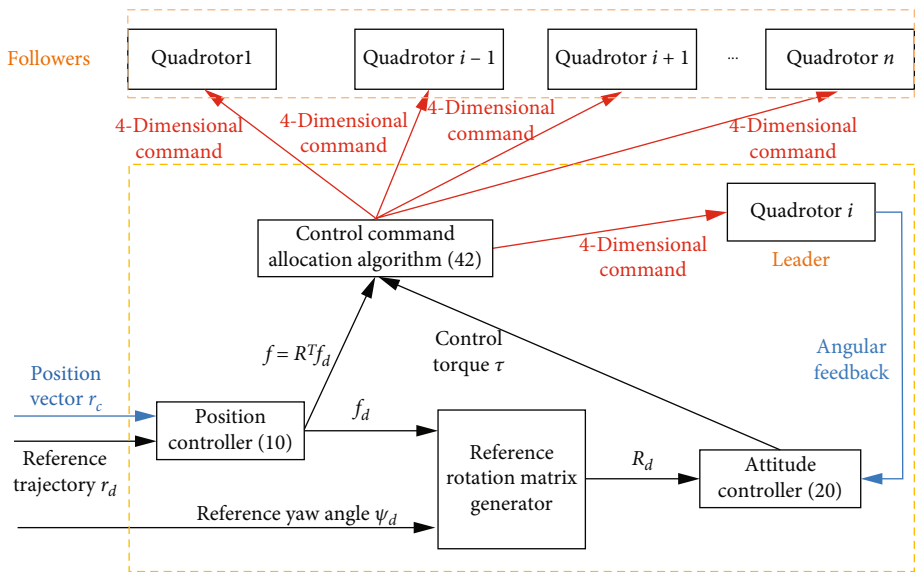

Figure 3: Control system diagram.

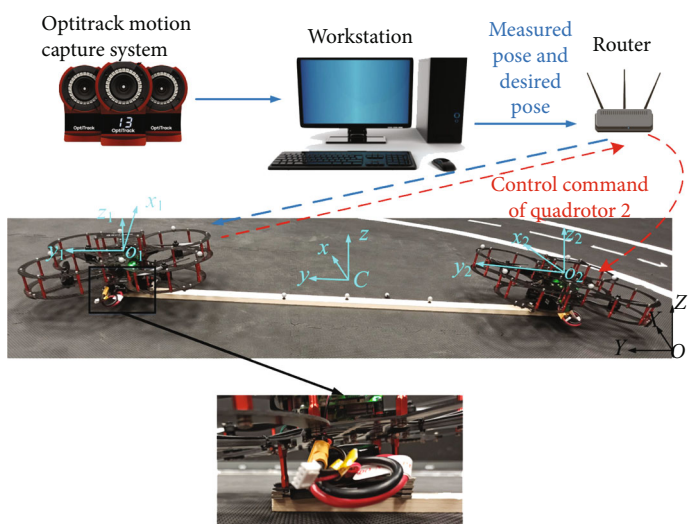

Figure 4: Experimental system.

dimensional control command for each quadrotor. It should be noted that one quadrotor can be set as a leader to run the controller and control command allocation algorithm and then send other control commands to the remaining quadrotors (followers).

4. Experimental Verification

As shown in Figure 4, the indoor test rig mainly consists of the OptiTrack motion capture system with 16 Flex 13 cameras, a work station, a router, two Quanser® QDrone quadrotors, and a payload to be transported. The QDrone quadrotor is a midsize quadrotor equipped with a powerful onboard Intel® Aero Compute Board, multiple high-resolution cameras, a BMI160 IMU, and the built-in WiFi. The motion capture system can measure the position and attitude of an object at 100 Hz. The real-time control of quadrotors is realized using Simulink from MathWorks and QUARC software [30] from Quanser Consulting Inc.

Magnets are used to connect the quadrotors and the board. As shown in the subfigure at the bottom of Figure 4, the right attachment point of quadrotor 1 has more magnets. Hence, the propeller plane of the first quadrotor is not parallel to the top surface of the board. Similarly, for quadrotor 2, the left connection point has more magnets than the right one. Mathematically, quadrotors 1 and 2 rotate −0.102 rad and 0.107 rad along the x axis in the frame of the entire system, respectively. Hence, the thrust forces of both quadrotors contribute to the movement in y direction. However, the movement along x axis can only be realized by the attitude maneuver in the pitch direction. In the body frame of the entire system, the position vectors of these two quadrotors are $\mathbf{r}_1 = [0.022, 0.56, -0.001]^T$ m and $\mathbf{r}_2 = [-0.022, -0.56, 0.001]^T$ m, respectively. Therefore, the system

Table 1: System parameters.

Parameter	Value
Quadrotor mass	1.121 kg
Inertia matrix of each quadrotor	diag $\{0.01, 0.0082, 0.0148\}$ kg·m^2
Maximum payload capability of each quadrotor	~ 0.3 kg
Payload mass	0.453 kg
Payload dimensions in x, y, and z directions	0.038 m × 1.219 m × 0.013 m
Inertia matrix of payload	diag $\{0.0561, 0.00006, 0.0561\}$ kg·m^2
Constant gravitational acceleration	9.81 m/s^2

Table 2: Parameters in controller and control command allocation algorithm.

Parameter	Value
w_0	1.5
$\mathbf{K}_p$	diag $\{6.9, 5.56, 35\}$
$\mathbf{K}_i$	diag $\{0.492, 0.588, 2.8\}$
$\mathbf{K}_d$	diag $\{10.8, 7.87, 23.3\}$
Γ	0.0005
k_R	3.9
k_Ω	1.3
ε	10^{-6}
δ	10^{-9}
$\mathbf{w}_1$	diag $\{0.5, 10, 1, 1\}$
$\mathbf{w}_2$	diag $\{0.5, 10, 1, 1\}$

in Figure 4 can well verify the effectiveness of the proposed controller and control command allocation method since the movement in x direction can be considered a special case with $\theta_i = 0$ for $i = 1, 2$.

The detailed physical parameters of quadrotor and payload are given in Table 1. Since the payload mass is larger than the maximum payload capability of a single quadrotor, at least two quadrotors have to be used to transport such a payload. In tests, the mass center of the entire system is defined as the middle point of two quadrotors approximately because these two quadrotors are much heavier than the payload. Therefore, the workstation will send the measured and desired position and yaw angles of the entire system to the first quadrotor via WiFi at 100 Hz, and then, its onboard compute board will calculate the control command for both quadrotors based on the designed controllers (13) and (19) with roll and pitch angles measured by IMU and the control command allocation law (27) at a rate of 1 kHz. The last four elements of $\mathbf{u}$ from Equation (27) will be sent to quadrotor 2 using WiFi, which implies that the onboard compute board of the second quadrotor will just implement the received four-dimensional control command without calculating the control command by itself. In essence, a centralized leader-follower architecture is adopted here. Note that some markers are attached to the payload to record the payload position only. The parameters in position and attitude controllers and control command allocation algorithm are given in Table 2.

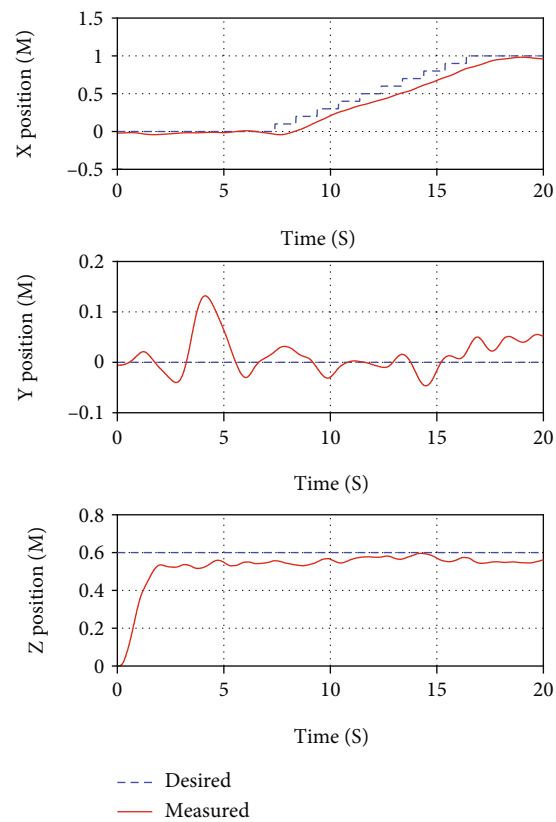

Figure 5: The position of the mass center of the entire system in the test in X direction.

Two experimental tests are performed with different desired trajectories. The experiment video can be seen here: http://youtu.be/Dv1wOyhUnlE. In the first test, the system is expected to move 1 m along X axis and keep the positions in Y and Z directions at 0 and 0.6 m. The desired yaw angle is set as 0 rad. To avoid large overshoot, the desired trajectory in X direction is set as a stair-step signal shown as the blue dashed curve in the first subfigure in Figure 5, i.e., the system is expected to keep moving 0.1 m per second for 10 seconds in X direction. As shown in Figure 5, the transportation system starts taking off at $t = 0$. The entire system

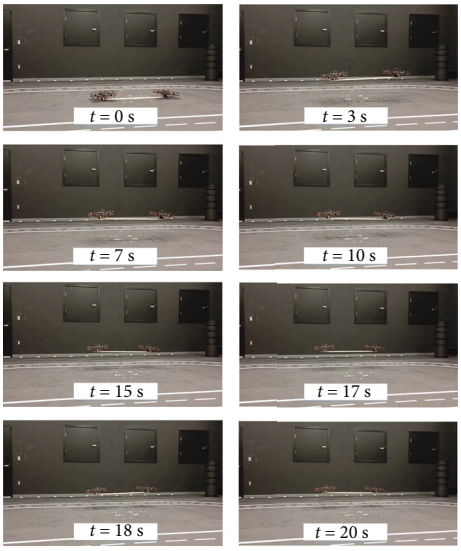

Figure 6: The snapshots of the test in X direction.

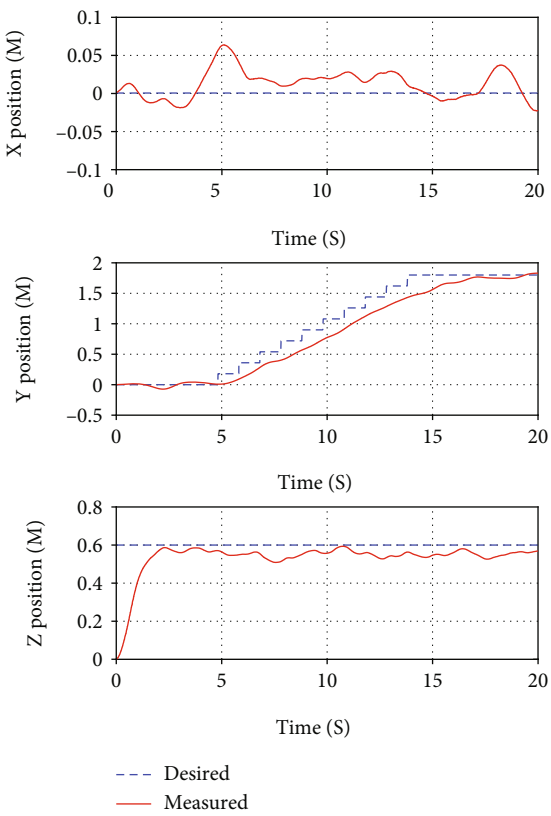

Figure 7: The position of the mass center of the entire system in the test in Y direction.

arrives at the hover status at 5 s. Due to the time delay of sending control command from the first quadrotor to the second one, and other unknown disturbances and uncertainties, a disturbance torque in roll direction is introduced in the take-off stage. Such a disturbance torque causes the system to move 13.2 cm in Y direction. As shown in the second subfigure in Figure 5, the designed control method is

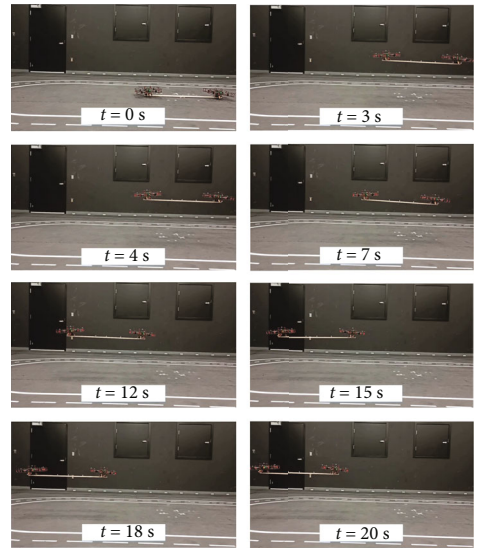

Figure 8: The snapshots of the test in Y direction.

able to drive the system back to the hover state. At about 7.4 s, the reference trajectory is sent to the first quadrotor. Finally, all tracking errors in X, Y, and Z directions are within 5 cm, which validates the effectiveness of the proposed control method. Figure 6 gives the snapshots of this test.

In the second test, the system will only move 1.8 m in 10 seconds in Y direction with the desired height 0.6 m and the desired zero yaw angle. Note that both thrust force and attitude maneuver of these two quadrotors can help finish the movement along Y axis. As shown in Figure 7, the designed control and command allocation methods can complete the transportation task with a tracking error of 5 cm. The snapshots of the test in Y direction are given in Figure 8.

In some sense, the simulation with 4 drones with different orientations is the easiest case for the designed controller because the matrix $(\mathbf{A}\mathbf{W}^{-1}\mathbf{A}^{T})$ is nonsingular, which implies that the thrust forces of four quadrotors are sufficient to contribute to the movement in both x and y directions. However, two quadrotors are used to verify the developed methods in this work. In our experimental testbed, the thrust forces of both quadrotors contribute to the movement in y direction. However, the movement along x axis can only be realized by the attitude maneuver in the pitch direction. That is, the presented experimental result in y direction can verify the effectiveness of the developed method for the case where the thrust forces can contribute to the translational movement and the result in x direction can be used to verify the trivial case.

5. Conclusions

In this study, a general framework of the dynamics modeling, controller design, and control command allocation method is presented for the transportation of a payload attached to quadrotors rigidly. Since quadrotors may have different orientations, horizontal control forces can be obtained by adjusting the thrust forces of some quadrotors.

Hence, different from the case for the classical quadrotors that the movement in the horizontal plane can only be realized based on attitude maneuvers in roll and pitch directions, the transportation system in this study can move in the horizontal plane by regulating some quadrotors' thrust forces. To get a universal control system, a hierarchical controller and a modified control command allocation algorithm is adopted. Experimental results show the effectiveness of the proposed control system. This work is the first trial to solve the dynamics modeling, controller design, and control command allocation problems for the transportation of a rigidly connected payload using a team of quadrotors with different orientations. In the future, the dynamics and control of such a transportation system can be studied with the uncertainties and communication delays between quadrotors.

Appendix

A. Detailed Expressions of the Total Inertia Matrix

Suppose that a new frame $x'y'z'$ is obtained by translating the origin of xyz to the point C_1 in Figure 2, where C_1 is the mass center of the payload. Hence, $x'y'z'$ can be called the payload body frame. Denote the inertia matrices of the payload and quadrotors with respect to their body frames as $\mathbf{J}_p$, $\mathbf{J}_1$, $\cdots$, $\mathbf{J}_n$. According to [31], the inertia matrix of the quadrotor i can be expressed in the frame xyz as

$$\mathbf{J}'_i = \mathbf{R}_i \mathbf{J}_i \mathbf{R}_i^T - m_q \mathbf{r}_i^\times \mathbf{r}_i^\times. \tag{A.1}$$

Similarly, in the frame xyz, the payload inertia matrix is

$$\mathbf{J}'_p = \mathbf{J}_p - m_p \mathbf{r}_p^\times \mathbf{r}_p^\times, \tag{A.2}$$

where $\mathbf{r}_p$ represents the vector from C to C_1 in the frame xyz. Hence, the total inertia matrix of the entire system in the frame xyz is

$$\mathbf{J} = \mathbf{J}'_p + \sum_{i=1}^{n} \mathbf{J}'_i. \tag{A.3}$$

B. Proof of Theorem 4

With the controller in Equation (13), the closed-loop system can be written as

$$m\ddot{\mathbf{e}}_c = -\left(\mathbf{K}_p + \mathbf{K}_i\right)\mathbf{e}_c - \mathbf{K}_i \int_0^t \mathbf{e}_c dt - \mathbf{K}_d \dot{\mathbf{e}}_c + m\tilde{\mathbf{q}}_3, \tag{B.1}$$

where $\mathbf{e}_c = \mathbf{r}_c - \mathbf{r}_d$. According to Lemma 3, $\tilde{\mathbf{q}}_3$ is bounded by a small constant c_Δ with a large w_0. Equation (B.1) can be rewritten as follows:

$$\dot{\mathbf{q}} = \mathscr{A}\mathbf{q} + \mathbf{\Delta}, \tag{B.2}$$

where

$$\begin{aligned} \mathbf{q} &= \left[\left(\int_0^t \mathbf{e}_c dt\right)^T, \mathbf{e}_c^T, \dot{\mathbf{e}}_c^T\right]^T, \\ \mathscr{A} &= \begin{bmatrix} \mathbf{0} & \mathbf{I}_3 & \mathbf{0} \\ \mathbf{0} & \mathbf{0} & \mathbf{I}_3 \\ -\dfrac{\mathbf{K}_i}{m} & -\dfrac{\mathbf{K}_p + \mathbf{K}_i}{m} & -\dfrac{\mathbf{K}_d}{m} \end{bmatrix}, \\ \mathbf{\Delta} &= \left[\mathbf{0}^T, \mathbf{0}^T, \tilde{\mathbf{q}}_3^T\right]^T. \end{aligned} \tag{B.3}$$

Since all eigenvalues of $\mathscr{A}$ have negative real parts, the following Lyapunov equation holds:

$$\mathscr{P}\mathscr{A} + \mathscr{A}^T\mathscr{P} = -\mathbf{I}, \tag{B.4}$$

where the matrix $\mathscr{P}$ is positive definite. Choose the following Lyapunov function:

$$V_p = \mathbf{q}^T \mathscr{P} \mathbf{q}, \tag{B.5}$$

whose time derivative is

$$\begin{aligned} \dot{V}_p &= \dot{\mathbf{q}}^T \mathscr{P}\mathbf{q} + \mathbf{q}^T \mathscr{P}\dot{\mathbf{q}} = -\boldsymbol{q}^T \boldsymbol{q} + \boldsymbol{\Delta}^T \mathscr{P}\boldsymbol{q} + \boldsymbol{q}^T \mathscr{P}\boldsymbol{\Delta} \\ &\le -\|\boldsymbol{q}\|_2^2 + 2\|\boldsymbol{\Delta}\|_2 \|\mathscr{P}\|_2 \|\boldsymbol{q}\|_2. \end{aligned} \tag{B.6}$$

In the case of $\|\mathbf{q}\|_2 > 2\|\mathbf{\Delta}\|_2\|\mathscr{P}\|_2$, $\dot{V}_p < 0$ holds. Hence, $\mathbf{q}$ will converge to the set $\{\mathbf{q} | \|\mathbf{q}\|_2 \le 2\|\mathbf{\Delta}\|_2\|\mathscr{P}\|_2\}$. According to Lemma 3, by increasing w_0, one can get a smaller tracking error.

C. Proof of Theorem 8

The closed-loop attitude dynamics is

$$\mathbf{J}\dot{\mathbf{E}}_\Omega = -k_R \mathbf{e}_R - k_\Omega \mathbf{E}_\Omega - \mathbf{J}\hat{\mathbf{d}}_2 + \mathbf{d}_2. \tag{C.1}$$

Consider the system governed by the following equation:

$$\mathbf{J}\dot{\mathbf{E}}_\Omega = -k_R \mathbf{e}_R - k_\Omega \mathbf{E}_\Omega. \tag{C.2}$$

Choose the following Lyapunov function:

$$V_a = \frac{k_R}{2}\|\mathbf{E}_R\|_F^2 + \frac{1}{2}\mathbf{E}_\Omega^T \mathbf{J}\mathbf{E}_\Omega + \mu \mathbf{e}_R^T \mathbf{E}_\Omega, \tag{C.3}$$

where $\mathbf{E}_R = \mathbf{R} - \mathbf{R}_d$, μ is a constant satisfying $0 < \mu < \sqrt{k_R \lambda_{\min}(\mathbf{J})/2}$, and $\|\cdot\|_F$ represents the Frobenius norm of a matrix. $\|\mathbf{E}_R\|_F$ has the following property:

$$\begin{aligned} \|\mathbf{E}_R\|_F^2 &= \|\mathbf{R} - \mathbf{R}_d\|_F^2 = \operatorname{trace}\left((\mathbf{R} - \mathbf{R}_d)^T (\mathbf{R} - \mathbf{R}_d)\right) \\ &= \operatorname{trace}\left((\mathbf{R} - \mathbf{R}_d)^T \mathbf{R}\mathbf{R}^T (\mathbf{R} - \mathbf{R}_d)\right) = \|\mathbf{I} - \mathbf{R}^T \mathbf{R}_d\|_F^2, \end{aligned}$$

$$\begin{aligned}\frac{d}{dt}\left(\|\mathbf{E}_R\|_F^2\right) &= \frac{d}{dt}\left(\operatorname{trace}\left(2\mathbf{I}-\mathbf{R}^T\mathbf{R}_d-\mathbf{R}_d^T\mathbf{R}\right)\right)\\ &= 2\operatorname{trace}\left(\boldsymbol{\Omega}^{\times}\mathbf{R}^T\mathbf{R}_d+\boldsymbol{\Omega}_d^{\times}\mathbf{R}_d^T\mathbf{R}\right)\\ &= -2\boldsymbol{\Omega}^T\left(\mathbf{R}^T\mathbf{R}_d-\mathbf{R}_d^T\mathbf{R}\right)^{\vee}-2\boldsymbol{\Omega}_d^T\left(\mathbf{R}_d^T\mathbf{R}-\mathbf{R}^T\mathbf{R}_d\right)^{\vee}\\ &= 2\boldsymbol{\Omega}^T\mathbf{e}_R-2\boldsymbol{\Omega}_d^T\mathbf{e}_R=2\mathbf{E}_{\Omega}^T\mathbf{e}_R.\end{aligned} \tag{C.4}$$

Using Rodrigues' rotation formula, one has

$$\begin{aligned}\|\mathbf{E}_R\|_F^2 &= 4(1-\cos\Theta),\\ \|\mathbf{e}_R\|_2 &= 2\sin\Theta,\end{aligned} \tag{C.5}$$

where Θ is the rotation angle in Rodrigues' rotation formula associated with the attitude motion described by $\mathbf{R}^T\mathbf{R}_d$. Hence, the following statement holds with the assumption that $\cos\Theta > -1$:

$$\|\mathbf{E}_R\|_F^2 \le \alpha\|\mathbf{e}_R\|_2^2, \tag{C.6}$$

where the constant $\alpha > 1$ is large enough. Furthermore, it is straightforward to show that

$$\|\mathbf{e}_R\|_2^2 \le 2\|\mathbf{E}_R\|_F^2. \tag{C.7}$$

Hence, $V_a \ge k_R/4\|\mathbf{e}_R\|_2^2 + 1/2\mathbf{E}_{\Omega}^T\mathbf{J}\mathbf{E}_{\Omega} + \mu\mathbf{e}_R^T\mathbf{E}_{\Omega} \ge k_R/4\|\mathbf{e}_R\|_2^2 + 1/2\lambda_{\min}(\mathbf{J})\|\mathbf{E}_{\Omega}\|_2^2 - \mu\|\mathbf{e}_R\|_2\|\mathbf{E}_{\Omega}\|_2 = \mathbf{z}^T\mathbf{W}_0\mathbf{z}$ holds, where

$$\begin{aligned}\mathbf{W}_0 &= \begin{bmatrix}\frac{k_R}{4} & -\frac{\mu}{2}\\ -\frac{\mu}{2} & \frac{1}{2}\lambda_{\min}(\mathbf{J})\end{bmatrix},\\ \mathbf{z} &= \left[\|\mathbf{e}_R\|_2, \|\mathbf{E}_{\Omega}\|_2\right]^T.\end{aligned} \tag{C.8}$$

With $0 < \mu < \sqrt{k_R\lambda_{\min}(\mathbf{J})/2}$, $\mathbf{W}_0$ is positive definite and $V_a \ge 0$ holds. If and only if $\|\mathbf{e}_R\|_2 = 0$, $\|\mathbf{E}_{\Omega}\|_2 = 0$, and $\|\mathbf{E}_R\|_F = 0$, V_a equals to 0. Furthermore, $V_a \le k_R/2\alpha\|\mathbf{e}_R\|_2^2 + 1/2\lambda_{\max}(\mathbf{J})\|\mathbf{E}_{\Omega}\|_2 + \mu\|\mathbf{e}_R\|_2\|\mathbf{E}_{\Omega}\|_2 = \mathbf{z}^T\mathbf{W}_1\mathbf{z}$ with

$$\mathbf{W}_1 = \begin{bmatrix}\frac{k_R\alpha}{2} & \frac{\mu}{2}\\ \frac{\mu}{2} & \frac{1}{2}\lambda_{\max}(\mathbf{J})\end{bmatrix}. \tag{C.9}$$

If $0 < \mu < \sqrt{k_R\lambda_{\min}(\mathbf{J})/2}$ holds, it is obvious that $\mathbf{W}_1$ is positive definite.

$\dot{V}_a$ can be expressed as

$$\begin{aligned}\dot{V}_a &= k_R\mathbf{E}_{\Omega}^T\mathbf{e}_R + \mathbf{E}_{\Omega}^T(-k_R\mathbf{e}_R - k_{\Omega}\mathbf{E}_{\Omega})\\ &\quad + \mu\left(\left(\operatorname{trace}\left(\mathbf{R}^T\mathbf{R}_d\right)\mathbf{I}-\mathbf{R}^T\mathbf{R}_d\right)\mathbf{E}_{\Omega}+\mathbf{e}_R\times\mathbf{E}_{\Omega}\right)^T\mathbf{E}_{\Omega}\\ &\quad + \mu\mathbf{e}_R^T\dot{\mathbf{E}}_{\Omega} = -k_{\Omega}\boldsymbol{E}_{\Omega}^T\boldsymbol{E}_{\Omega}\\ &\quad + \mu\left(\left(\operatorname{trace}\left(\boldsymbol{R}^T\boldsymbol{R}_d\right)\boldsymbol{I}-\boldsymbol{R}^T\boldsymbol{R}_d\right)\boldsymbol{E}_{\Omega}\right)^T\boldsymbol{E}_{\Omega}\\ &\quad + \mu\boldsymbol{e}_R^T\boldsymbol{J}^{-1}(-k_R\boldsymbol{e}_R - k_{\Omega}\boldsymbol{E}_{\Omega}).\end{aligned} \tag{C.10}$$

It is straightforward from Rodrigues' rotation formula to show that $\|\operatorname{trace}(\mathbf{R}^T\mathbf{R}_d)\mathbf{I} - \mathbf{R}^T\mathbf{R}_d\|_F = 2$. Hence, one has $\|\operatorname{trace}(\mathbf{R}^T\mathbf{R}_d)\mathbf{I} - \mathbf{R}^T\mathbf{R}_d\|_2 \le \|\operatorname{trace}(\mathbf{R}^T\mathbf{R}_d)\mathbf{I} - \mathbf{R}^T\mathbf{R}_d\|_F = 2$. $\dot{V}_a$ satisfies the following inequality:

$$\begin{aligned}\dot{V}_a &\le -k_{\Omega}\|\mathbf{E}_{\Omega}\|_2^2 + 2\mu\|\mathbf{E}_{\Omega}\|_2^2 - k_R\mu\mathbf{e}_R^T\mathbf{J}^{-1}\mathbf{e}_R - k_{\Omega}\mu\mathbf{e}_R^T\mathbf{J}^{-1}\mathbf{E}_{\Omega}\\ &\le -(k_{\Omega}-2\mu)\|\boldsymbol{E}_{\Omega}\|_2^2 - k_R\mu\lambda_{\min}\left(\boldsymbol{J}^{-1}\right)\|\boldsymbol{e}_R\|_2^2\\ &\quad + k_{\Omega}\mu\lambda_{\max}\left(\boldsymbol{J}^{-1}\right)\|\boldsymbol{e}_R\|_2\boldsymbol{J}^{-1}\|\boldsymbol{E}_{\Omega}\|_2 = -\boldsymbol{z}^T\boldsymbol{W}_2\boldsymbol{z},\end{aligned} \tag{C.11}$$

where

$$\mathbf{W}_2 = \begin{bmatrix}k_R\mu\lambda_{\min}\left(\mathbf{J}^{-1}\right) & -\frac{k_{\Omega}\mu\lambda_{\max}\left(\mathbf{J}^{-1}\right)}{2}\\ -\frac{k_{\Omega}\mu\lambda_{\max}\left(\mathbf{J}^{-1}\right)}{2} & (k_{\Omega}-2\mu)\end{bmatrix}. \tag{C.12}$$

There must exist a positive constant $0 < \sigma \le \lambda_{\min}(\mathbf{W}_2)/\lambda_{\max}(\mathbf{W}_1)$ such that $\mathbf{W}_2 - \sigma\mathbf{W}_1 \ge 0$ holds. Therefore, one has

$$\dot{V}_a \le -\sigma V_a. \tag{C.13}$$

Therefore, the closed-loop system in Equation (B.3) is exponentially stable except at some points with $\cos\Theta = -1$.

As shown in Lemma 7, $-\mathbf{J}\hat{\mathbf{d}}_2 + \mathbf{d}_2$ is ultimately bounded. According to [32], the designed controller can drive the system to a small neighborhood of the desired attitude almost globally.

Data Availability

The data used to support the findings of this study are available from the corresponding author upon request.

Conflicts of Interest

The authors declare that they have no conflicts of interest.

Acknowledgments

This work was supported by the Science and Technology on Space Intelligent Control Laboratory (Grant No. 2021-JCJQ-LB-010-17) and the National Natural Science Foundation of China under Grant 12102174.

References

[1] J. Euchi, "Do drones have a realistic place in a pandemic fight for delivering medical supplies in healthcare systems problems?," *Chinese Journal of Aeronautics*, vol. 34, no. 2, pp. 182–190, 2021.

[2] D. Xilun, G. Pin, X. Kun, and Y. Yushu, "A review of aerial manipulation of small-scale rotorcraft unmanned robotic systems," *Chinese Journal of Aeronautics*, vol. 32, no. 1, pp. 200–214, 2019.

[3] A. Gupta, T. Afrin, E. Scully, and N. Yodo, "Advances of UAVs toward future transportation: The State-of-the-Art, challenges, and Opportunities," *Transportation*, vol. 1, no. 2, pp. 326–350, 2021.

[4] D. K. Villa, A. S. Brandao, and M. Sarcinelli-Filho, "A survey on load transportation using multirotor UAVs," *Journal of Intelligent and Robotic Systems*, vol. 98, no. 2, pp. 267–296, 2020.

[5] I. Palunko, P. Cruz, and R. Fierro, "Agile load transportation: safe and efficient load manipulation with aerial robots," *IEEE Robotics and Automation Magazine*, vol. 19, no. 3, pp. 69–79, 2012.

[6] F. Ruggiero, V. Lippiello, and A. Ollero, "Aerial manipulation: a literature review," *IEEE Robotics and Automation Letters*, vol. 3, no. 3, pp. 1957–1964, 2018.

[7] T. Chen and J. Shan, "A novel cable-suspended quadrotor transportation system: from theory to experiment," *Aerospace Science and Technology*, vol. 104, article 105974, 2020.

[8] L. Qian and H. H. Liu, "Path-following control of a quadrotor UAV with a cable-suspended payload under wind disturbances," *IEEE Transactions on Industrial Electronics*, vol. 67, no. 3, pp. 2021–2029, 2020.

[9] P. J. Cruz and R. Fierro, "Cable-suspended load lifting by a quadrotor UAV: hybrid model, trajectory generation, and control," *Autonomous Robots*, vol. 41, no. 8, pp. 1629–1643, 2017.

[10] A. Tagliabue, M. Kamel, R. Siegwart, and J. Nieto, "Robust collaborative object transportation using multiple MAVs," *The International Journal of Robotics Research*, vol. 38, no. 9, pp. 1020–1044, 2019.

[11] T. Chen, J. Shan, and H. H. Liu, "Cooperative transportation of a flexible payload using two quadrotors," *Journal of Guidance, Control, and Dynamics*, vol. 44, no. 11, pp. 2099–2107, 2021.

[12] T. Chen and J. Shan, "Cooperative transportation of cable-suspended slender payload using two quadrotors," in *2019 IEEE International Conference on Unmanned Systems (ICUS)*, pp. 432–437, IEEE, 2019.

[13] N. Michael, J. Fink, and V. Kumar, "Cooperative manipulation and transportation with aerial robots," *Autonomous Robots*, vol. 30, no. 1, pp. 73–86, 2011.

[14] D. Sanalitro, H. J. Savino, M. Tognon, J. Cort'es, and A. Franchi, "Full-pose manipulation control of a cable-suspended load with multiple UAVs under uncertainties," *IEEE Robotics and Automation Letters*, vol. 5, no. 2, pp. 2185–2191, 2020.

[15] J. Geng and J. W. Langelaan, "Cooperative transport of a slung load using load-leading control," *Journal of Guidance, Control, and Dynamics*, vol. 43, no. 7, pp. 1313–1331, 2020.

[16] Q. Jiang and V. Kumar, "The inverse kinematics of cooperative transport with multiple aerial robots," *IEEE Transactions on Robotics*, vol. 29, pp. 136–145, 2013.

[17] F. A. Goodarzi and T. Lee, "Stabilization of a Rigid Body Payload With Multiple Cooperative Quadrotors," *Journal of Dynamic Systems, Measurement, and Control*, vol. 138, no. 12, article 121001, 2016.

[18] L. Qian and H. H. Liu, "Path following control of multiple quadrotors carrying a rigid-body slung payload," *AIAA Scitech 2019 Forum*, p. 1172, 2019.

[19] H. Lee, H. Kim, W. Kim, and H. J. Kim, "An integrated framework for cooperative aerial manipulators in unknown environments," *IEEE Robotics and Automation Letters*, vol. 3, no. 3, pp. 2307–2314, 2018.

[20] Y. Qi, J. Wang, and J. Shan, "Aerial cooperative transporting and assembling control using multiple quadrotor–manipulator systems," *International Journal of Systems Science*, vol. 49, no. 3, pp. 662–676, 2018.

[21] H. Lee, H. Kim, and H. J. Kim, "Planning and control for collision-free cooperative aerial transportation," *IEEE Transactions on Automation Science and Engineering*, vol. 15, no. 1, pp. 189–201, 2018.

[22] D. Mellinger, M. Shomin, N. Michael, and V. Kumar, "Cooperative grasping and transport using multiple quadrotors," in *Distributed autonomous robotic systems*, pp. 545–558, Springer, 2013.

[23] G. Loianno and V. Kumar, "Cooperative transportation using small quadrotors using monocular vision and inertial sensing," *IEEE Robotics and Automation Letters*, vol. 3, pp. 680–687, 2018.

[24] R. Ritz and R. D'Andrea, "Carrying a flexible payload with multiple flying vehicles," in *2013 IEEE/RSJ International Conference on Intelligent Robots and Systems*, pp. 3465–3471, IEEE, 2013.

[25] Q. Zheng, L. Q. Gaol, and Z. Gao, "On stability analysis of active disturbance rejection control for nonlinear time-varying plants with unknown dynamics," in *2007 46th IEEE conference on decision and control*, pp. 3501–3506, IEEE, 2007.

[26] J. Yao, Z. Jiao, and D. Ma, "Adaptive robust control of DC motors with extended state observer," *IEEE Transactions on Industrial Electronics*, vol. 61, pp. 3630–3637, 2014.

[27] T. Chen, J. Shan, and H. Wen, "Distributed adaptive attitude control for networked underactuated flexible spacecraft," *IEEE Transactions on Aerospace and Electronic Systems*, vol. 55, pp. 215–225, 2019.

[28] B.-Z. Guo and Z. L. Zhao, "On the convergence of an extended state observer for nonlinear systems with uncertainty," *Systems & Control Letters*, vol. 60, no. 6, pp. 420–430, 2011.

[29] Z. Zheng and M. Shen, "Inertial vector measurements based attitude synchronization control for multiple spacecraft formation," *Aerospace Science and Technology*, vol. 93, article 105309, 2019.

[30] QUARC, "real-time control software," 2021, https://www.quanser.com/products/quarc-real-time-control-software/ Accessed November 16, 2021.

[31] F. P. Beer and E. R. Johnston, *Vector Mechanics for Engineers*, McGraw-Hill New York, 7th Edition edition, 2004.

[32] D. Angeli and L. Praly, "Stability robustness in the presence of exponentially unstable isolated equilibria," *IEEE Transactions on Automatic Control*, vol. 56, no. 7, pp. 1582–1592, 2011.

Hindawi
International Journal of Aerospace Engineering
Volume 2022, Article ID 4840814, 14 pages
https://doi.org/10.1155/2022/4840814

Research Article

The Reduced-Order Model for Droplet Drift of Aerial Spraying under Random Lateral Wind

Wencheng Li,[1,2] **Wenyun Wang**,[3] **Xiaomao Huang**,[1,2] **and Chenyang Li**[1]

[1]*College of Engineering, Huazhong Agricultural University, Wuhan 430070, China*
[2]*Key Laboratory of Agricultural Equipment in Mid-Lower Yangtze River, Ministry of Agriculture and Rural Affairs, Wuhan 430070, China*
[3]*The 9Th Designing of China Aerospace Science and Industry Corporation, Wuhan 430040, China*

Correspondence should be addressed to Wencheng Li; li_wch@hzau.edu.cn

Received 7 January 2022; Revised 7 March 2022; Accepted 21 March 2022; Published 12 April 2022

Academic Editor: Ti Chen

The droplet drift during aerial spraying process of oilseed rape, which is induced by complex flow field including random lateral wind, is difficult to predict and suppress. In this study, the high-fidelity computational fluid dynamics (CFD) technique is employed to simulate the two-phase flow of droplets in the rotor flow field, and the influence of main operation parameters on spraying effect is investigated numerically. Furthermore, the mechanism of droplet deposition in various operation conditions is discussed according to the analysis of unsteady flow field characteristics. However, the simulation via CFD technique is time-consuming, and it is not suitable for multidisciplinary work and optimization design. To address such issue, a filter white Gaussian noise signal is used to mimic the random lateral wind, and the droplet drift distance is obtained numerically. Based on the input and output dataset of CFD, the recursive algorithm including nonlinear autoregressive exogenous model and surrogate-based recurrence framework and the deep learning method for time-series prediction called long short-term memory neural network are used to build the efficient reduced-order model, respectively. Numerical simulations show that the droplet drift distance can be predicted by measurable lateral wind speed via the reduced-order model approach, which agreed well with the results obtained via the CFD method. In addition, the reduced-order model could decrease computation cost by 6 orders of magnitude with an acceptable accuracy, which indicates that the proposed method could be used for the design of off-line closed-loop controller of a variable spraying system.

1. Introduction

As a most important source of edible oil, oilseed rape is widely planted in mid-lower Yangtze River of China. In addition, different growth stages and various parts of oilseed rape can be processed as vegetable, forage, fertilizer, flower, and honey in an economical way [1, 2]. However, the growth of oilseed rape is seriously affected by pests and diseases, for instance, sclerotia can reduce the yield of oilseed rape crop up to 70% during the blooming period. Considering the limitations of a complex terrain in China, the inefficient traditional ground plant protection machinery cannot satisfy the requirement of plant protection of modern agriculture.

The near-ground aerial spraying based on unmanned aerial vehicle (UAV) flight control and navigation technology, which can operate at high flight speed without the direct touch of crops, provides a feasible and efficient approach [3–6]. Compared with traditional ground plant protection operation, aerial spraying could increase operating efficiency and reduce pesticide consumption. However, the aerial spraying process is a complex gas-liquid-solid interaction system, and the spraying effect is significantly influenced by different operation conditions and environment parameters, such as flight altitude, free-stream velocity, environmental wind field, and nozzle performance [7]. For instance, increasing the flight speed can improve the spraying efficiency but weaken the ability of the downwash to forcing droplets to deposit on the crop surface, making the droplet drift along the downstream direction especially when lateral wind exists [8, 9]. A high flight speed will strengthen

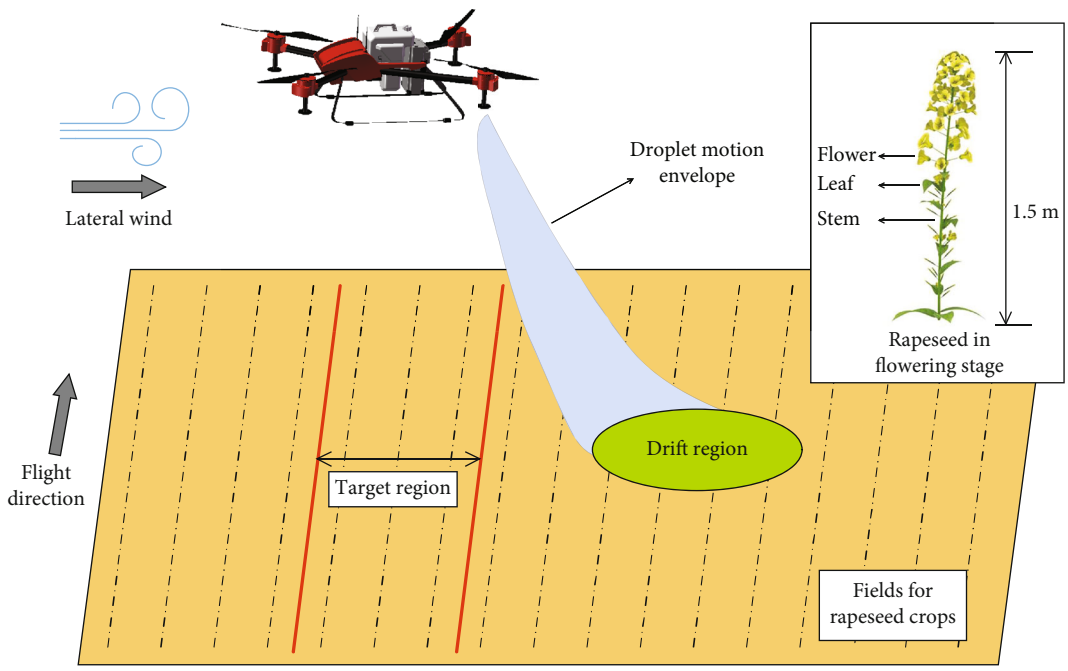

Figure 1: The schematic diagram of oilseed rape aerial spraying.

the coupling effect of vortex and turbulence effect of rotor, leading to the decrease of uniformity, effective range, and density of droplet deposition significantly [10]. Furthermore, the flow field characteristics of downwash near the crop canopy and the droplet spraying uniformity are sensitive to the flight altitude. Based on the computational fluid dynamics (CFD) simulation results for different flight altitudes, it is indicated that as the UAV is far away from the crops, velocity amplitude distribution of the flow field will be more concentrated and the longitudinal velocity gradient of the downwash will be reduced; thus, the wall reflection effect between the downwash flow and crops would be weakened [11]. Wang et al. [8] analyzed the effects of operation altitude and flight speed of UAV on droplet deposition and distribution characteristics; the results indicate that appropriately increasing flight altitude and reducing flight speed had a significant impact on the improvement of spraying effect. Qin et al. [12] investigated the influence of flight parameters of plant protection UAV on droplet drift via experimental method; it is found that the droplet deposition in corn crop canopy could get the ideal operation state when the flight altitude is 7 meters, while the spraying effect is easily affected by downwash flow field and lateral wind at other flight altitudes, which makes a lower penetration and deposition efficiency. In addition, based on the numerical simulation results and wind tunnel experiments, it has been pointed out that the initial velocity direction and droplet trajectory will be changed for various nozzle angles, making a significantly difference in the droplet drift distance along the direction of lateral wind. For instance, the droplet drift distance could be reduced 60% by choosing the proper angle of spraying nozzle when the lateral wind speed reaches 5 m/s [13]. Furthermore, the droplet drift induced by the uncontrollable random lateral wind coupled with the strong periodic downwash flow field of rotor aircraft is difficult to suppress, leading to the waste of pesticide and environmental pollution, which is the most concerned issue to be solved in aerial spraying field. When considering the influence of lateral wind alone, the droplet drift distance and drift rate are linearly related to the amplitude of wind speed. However, when the coupling effect of downwash is taken into account, the lateral wind with small amplitude has limited influence on the droplet drift while a strong lateral wind will significantly increase the droplet drift distance due to the coupled aerodynamic effect of the lateral wind shear and rotor vortex [14].

It can be seen from the above research that the random lateral wind plays an important role in improving the effectiveness and efficiency of aerial spraying. It should be noted that once the desired variable spraying feedback control system is established, the variable-spraying actuator could be automatically operated based on the measured random lateral wind signal to ensure the uniformity of spraying and suppress the droplet drift. However, the construction of control system relies on the high-fidelity CFD method, which is time-consuming especially for the multi-parameter simulation of three-dimensional two-phase flow; thus, it cannot be used in controller design directly [15–17]. To address such issue, the reduced-order model (ROM) technique, which could transform the high-order finite element model into an approximation low-order model, can be used to design the off-line controller in an efficient and accurate way. For instance, based on the system identification theory, Glaz et al. [18] developed the efficient ROM of the rotor to predict the unsteady aerodynamics response via the Kriging surrogate model and surrogate-based recurrence framework. Zhang et al. [19] built the nonlinear ROM of the aeroelastic system in transonic regime by employing the RBF neural

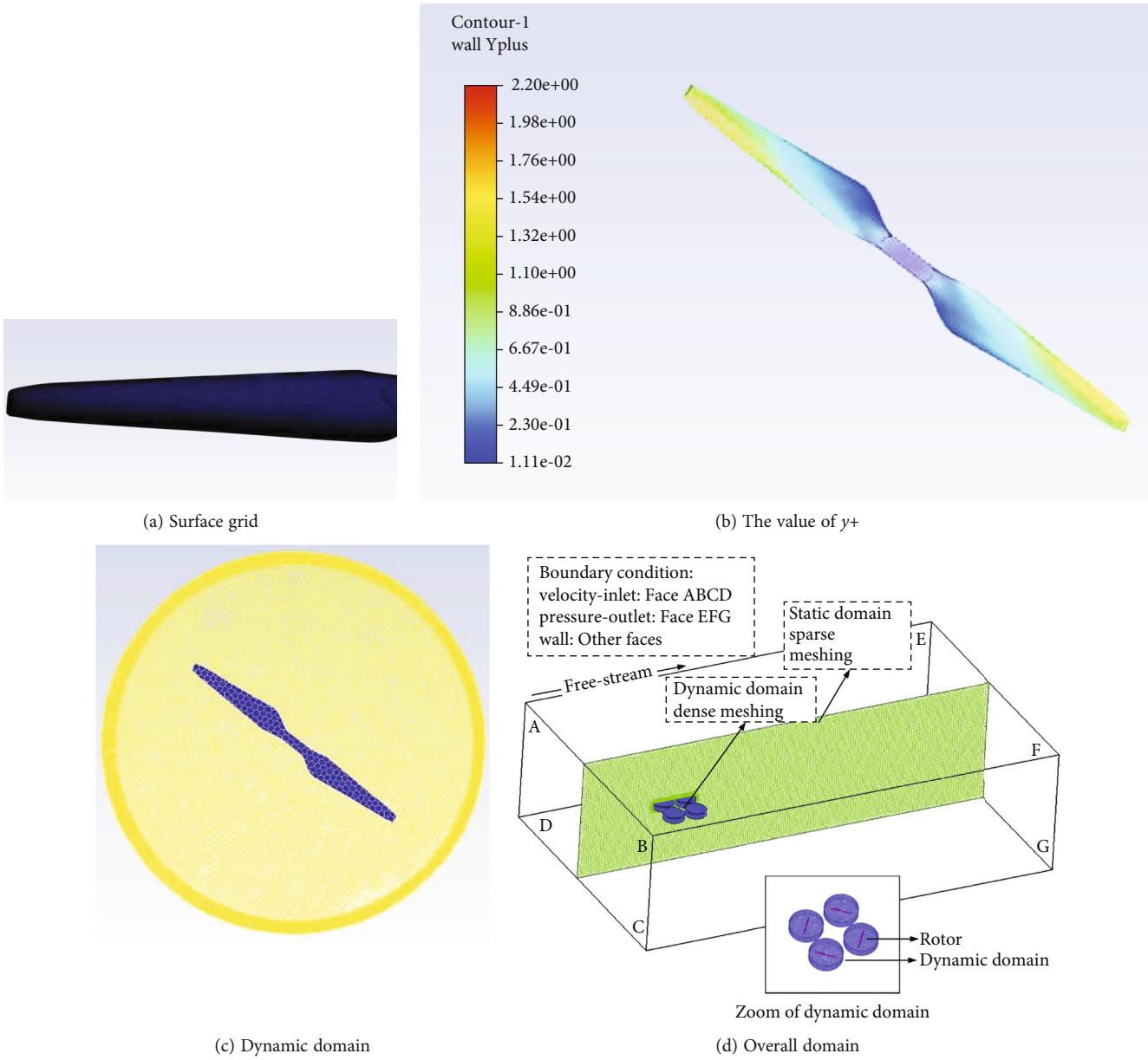

(a) Surface grid

(b) The value of $y+$

(c) Dynamic domain

(d) Overall domain

Figure 2: The mesh grid of computational domain.

network, and the nonlinear dynamics behaviors including limited cycle oscillation and flutter boundary are predicted accurately. Recently, the deep learning method involving long short-term memory (LSTM) neural network has been used to build the ROM of multiple-input-multiple-output fluid-structure interaction system [20, 21]. Based on the integration of the control algorithm and efficient ROM technique, Huang et al. [22] developed the control method for flutter suppression to expand flight envelope via a numerical and experimental technique.

In the process of time-consuming CFD unsteady simulation, the target current output (i.e., droplet deposition) depends mainly on the current input (i.e., the random lateral wind) and previous output. The motivation of this paper is based on the basic principle of CFD unsteady calculation, the reduced-order models are built by employing surrogate-based recurrence framework and deep learning method, respectively, which could predict the current output by the known external input and previous predicted output; thus, the droplet drift response under random lateral wind can be obtained in an efficient way. In what follows, with the consideration of the computational efficiency of multiparameter analysis, a single-rotor model is used to perform the high-fidelity CFD simulation numerically. In particular, the ground is modeled as a conveyor belt, and the droplet deposition characteristics on the ground in forward flight could be presented more accurately and intuitively. Finally, two efficient ROMs are built based on data-driven theory to predict the response of droplet drift. The contributions of this study are as follows: (i) Based on the data obtained via the

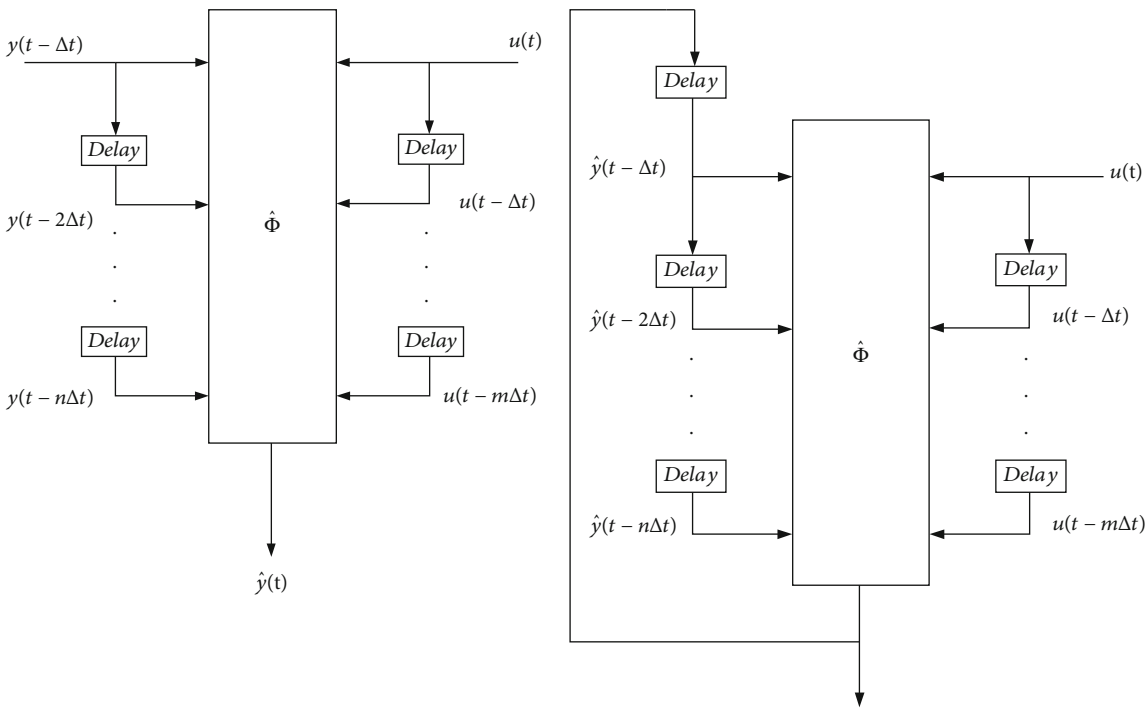

(a) Nonlinear autoregressive exogenous model (b) Surrogate-based recurrence framework

Figure 3: The recurrence scheme for time-series prediction of ROM.

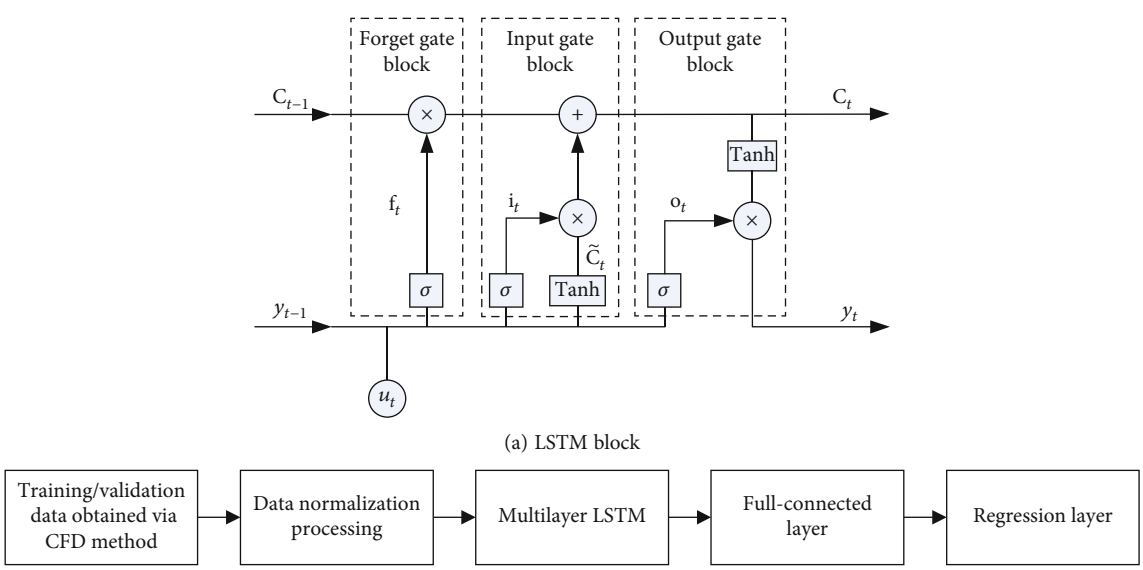

(a) LSTM block

(b) The LSTM-based network architecture for time-series prediction

Figure 4: The LSTM scheme for time-series prediction of ROM.

CFD method, the ground is modeled as a conveyor belt to perform the temporal and spatial distribution characteristic of droplets. (ii) The efficient ROMs are established via the deep learning method and surrogate-based recurrence framework, respectively, to predict the behavior of droplet drift.

The remainder of this study is organized as follows. In Section 2, the simplified finite element model and time-dependent ROM technique based on the recursive algorithm and the LSTM theory are introduced. In Section 3, various simulation cases under different operation conditions are investigated, involving steady and transient situation. In

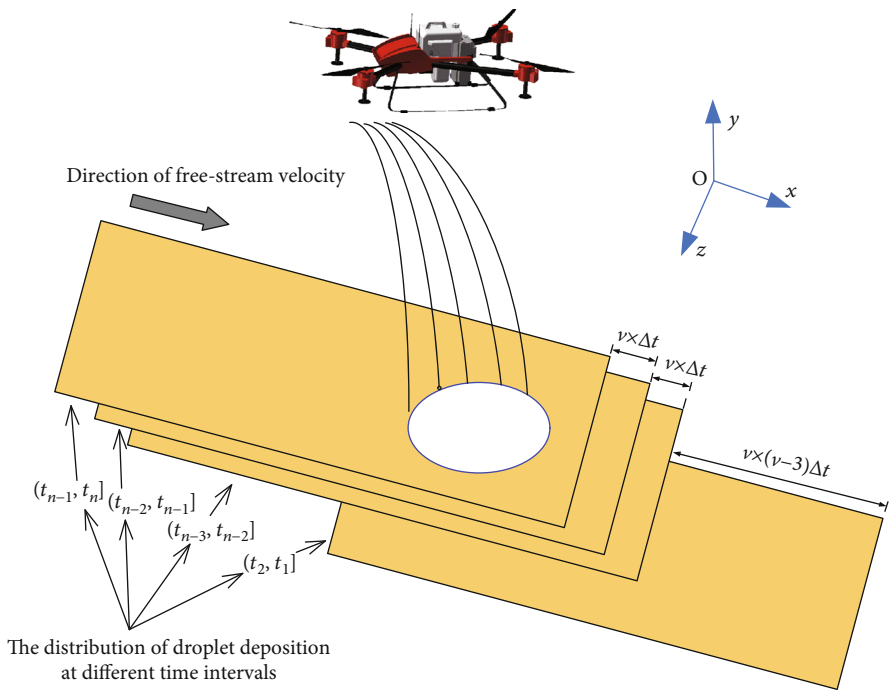

Figure 5: The schematic diagram of conveyor belt model for droplet deposition.

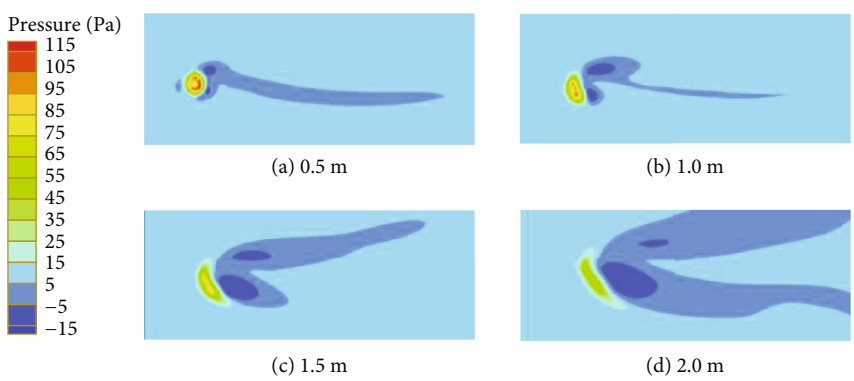

Figure 6: Pressure distribution below the rotor when free stream velocity is 3 m/s.

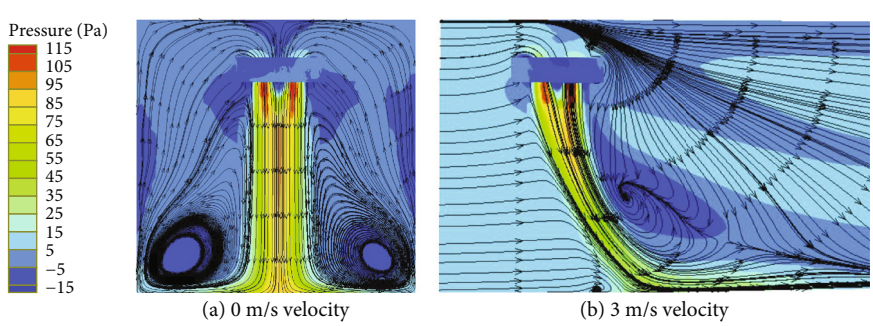

Figure 7: The streamlines of flow field at different free stream velocities.

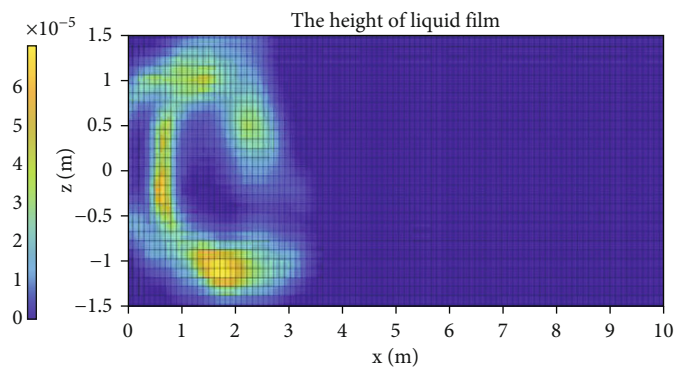

(a) hover state

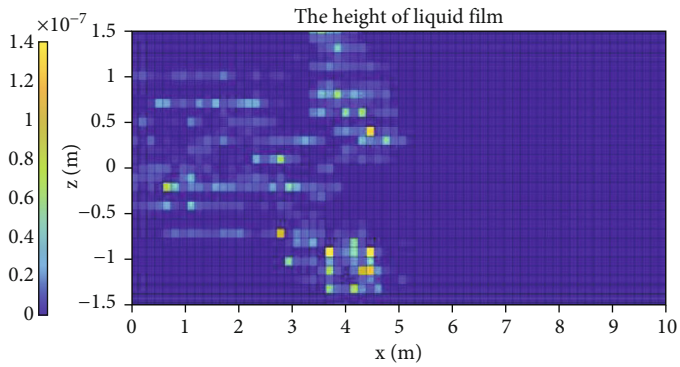

(b) forward flight

Figure 8: The height of deposited liquid film on the ground when velocity is 1 m/s.

addition, the prediction results of ROMs are performed to assess the validity of proposed method. Finally, Section 4 concludes this paper.

2. Background and Theory

2.1. Governing Equation and Simplified Model. The schematic diagram of the oilseed rape aerial spraying system considering the influence of lateral wind is shown in Figure 1, which performs the droplet drift to the nontarget region due to unpredictable meteorological condition. In this study, ignoring the influence of fuselage, the commercial software Fluent is used to analyze the two-phase flow interaction dynamics, and the sliding mesh method is employed to simulate the high-speed rotational motion of the rotor wing. As shown in Equation (1), the governing Navier-Stokes equation can be discretely solved by the second order upwind scheme.

$$\rho \frac{dV}{dt} = f - \nabla p + \mu \nabla^2 V, \tag{1}$$

where ρ is the density of fluid and V, f, and p are the vectors of velocity, external force per unit volume, and pressure, respectively.

To accurately capture the details of the flow field, Euler method and shear stress transfer k-ω turbulence model expressed are chosen to calculate the steady and transient aerodynamic response of the fluid phase. The discrete phase model described via dynamics equation Equation (2) is used to mimic the motion of a discrete phase in the Lagrangian reference frame, where m_p is the mass of particle, u and u_p are the velocity of fluid phase and discrete phase, and ρ and ρ_p denote the density of fluid phase and discrete phase, respectively [23]. $m_p((u - u_p)/\tau_r)$ and F are the drag force and additional force term, respectively, where τ_r is the relaxation time of droplet. It can be seen that the transport of droplet is mainly governed by the initial state of the droplet leaving the nozzle and the aerodynamic load around the rotor.

$$m_p \frac{du_p}{dt} = m_p \frac{(u - u_p)}{\tau_r} + m_p \frac{g(\rho_p - \rho)}{\rho_p} + F. \tag{2}$$

The speed of the rotor and the corresponding time step of transient simulation after steady calculation are set as 2500 rpm and 0.0025 seconds, respectively. Furthermore, a wall-film boundary condition is chosen to capture the deposition and distribution of the droplet on the ground. The surface mesh of rotor wing is presented in Figure 2(a), the hybrid grid is employed to divide the volume mesh, and the total number of grids is about 3.35×10^6, where the diameter and the chord length at 3/4-span location of rotor are 400 mm and 42 mm. The height of the first boundary

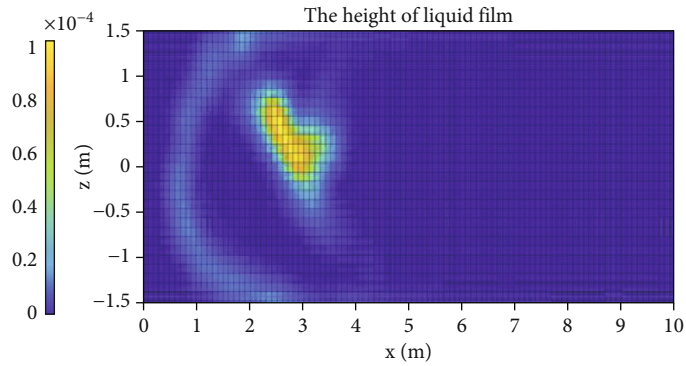

(a) hover state

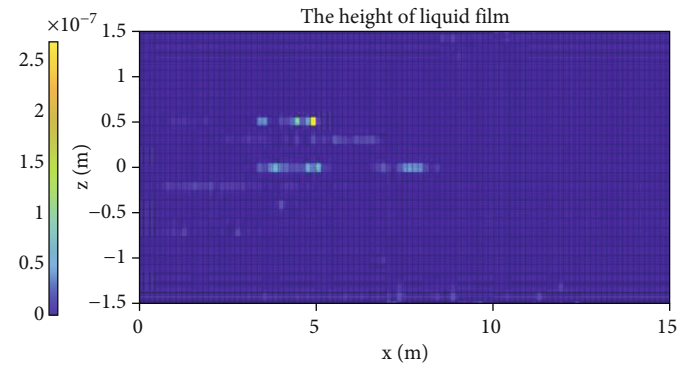

(b) forward flight

Figure 9: The height of deposited liquid film on the ground when velocity is 2 m/s.

layer is 5×10^{-6} m and the corresponding $y+$ contour is shown in Figure 2(b), which indicates that the volume meshing and boundary layer satisfy the requirement of the chosen turbulence model. The dynamic domain and overall domain are presented in Figures 2(c) and 2(d), respectively, where the diameter and height of dynamic domain are 1032 mm and 400 mm; the size of the overall computation domain is about 26 m × 8 m × 16 m. In order to perform the droplet drift behavior well, the computation domain downstream is larger than the upstream one. The sliding grid method and multiple reference frame (MRF) are employed to model dynamic process of the high-speed rotation of rotor, where the static domain with sparse meshing and dynamic domain with dense meshing are adopted. In addition, a pressure-swirl atomizing hollow cone nozzle is used to generate 200 μm droplets with 0.08 kg/s total flow rate, where the initial velocity of droplets is 35 m/s and the con angle of nozzle is 55 degrees.

2.2. ROMs Based on Recursive Algorithm and LSTM Neural Network

2.2.1. Recursive Algorithm. Based on the time-series prediction method, such as nonlinear autoregressive exogenous model with exogenous inputs Tsungnan et al., [24] and surrogate-based recurrence framework [18] presented in Figure 3, the response of the following multiple-input and multiple-output dynamic system can be predicted, which yields

$$\hat{y}(t) = \hat{\Phi}(y(t-1),\cdots,y(t-n), u(t),\cdots,u(t-m)), \tag{3}$$

$$\hat{y}(t) = \hat{\Phi}(\hat{y}(t-1),\cdots,\hat{y}(t-n), u(t),\cdots,u(t-m)), \tag{4}$$

where Φ is the nonlinear map between the input u and output y and m and n are the time-delay order of input and output, respectively. Superscript $\wedge$ denotes the approximation of corresponding accurate term.

Equations (3) and (4) are black box models based on data-driven of the nonlinear autoregressive exogenous model and surrogate-based recurrence framework, respectively, which can convert a complicated high-order nonlinear system into an approximate low-order model by using the dataset of input and output. It should be noted that the prediction of current output value $\hat{y}(t)$ via the nonlinear autoregressive exogenous model depends the true value of past output $(y(t-1),\cdots,y(t-n))$, while the prediction of surrogate-based recurrence framework is based on the prediction value of past output dataset $(\hat{y}(t-1),\cdots,\hat{y}(t-n))$. However, the true value of output may be difficult or time-consuming to obtain in some situations; thus, the ROM based on surrogate-based recurrence framework provides a feasible approach for such case. In other words, the prediction via surrogate-based recurrence framework-based ROM just needs a well-trained surrogate model $\hat{\Phi}$ and a real-time measurable input dataset $(u(t),\cdots,u(t-m))$.

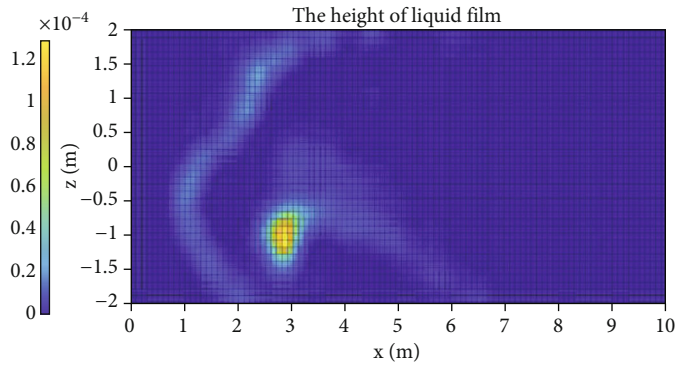

(a) hover state

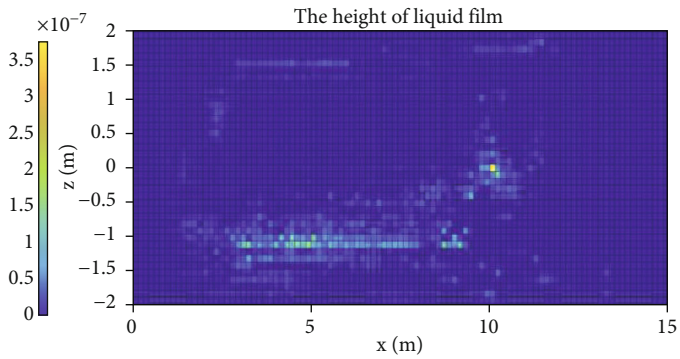

(b) forward flight

Figure 10: The height of deposited liquid film on the ground when velocity is 3 m/s.

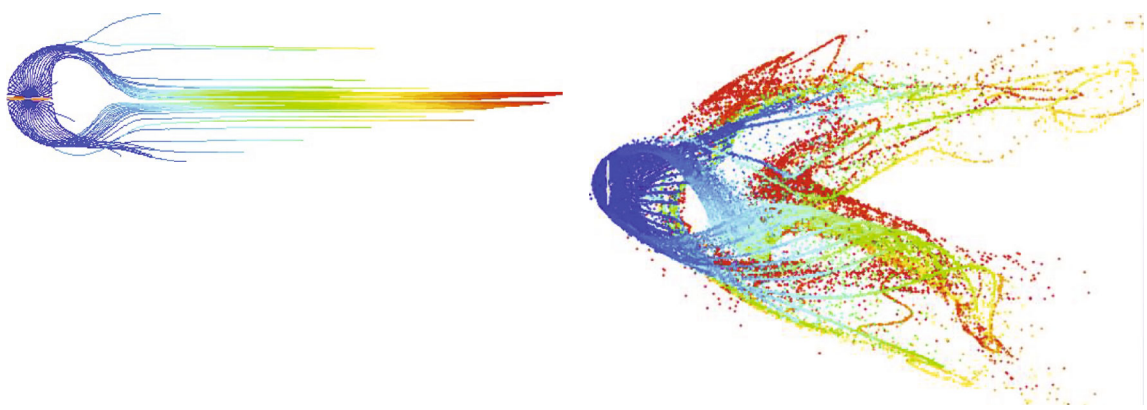

(a) steady state (b) transient state

Figure 11: Droplets trajectory of single-rotor when the free-stream velocity is 3 m/s.

2.2.2. LSTM Neural Network. The LSTM network architecture is presented in Figure 4(a), which consists of three different gates block, namely, forget gate f_t, input gate i_t, and output gate o_t, where the gate function is a Sigmoid function as shown in Equation (5), where W and b are the weight vector and offset term, respectively [25].

$$g(x) = \sigma(Wx + b). \tag{5}$$

When the current input u_t and the previous output storing in state h_{t-1} pass the forget gate, the Sigmoid function in Equation (6) decides whether the signal can pass through the gate. For instance, when the output of the gate function is zero, it is indicated that no information is reserved, whereas the output is 1 represents all signals could pass without barriers. In other words, the gate function suggests the probability of the data passing the block. Similarly, the input gate and output gate are read in Equations (7) and (8), respectively, where W^* and b^* are the corresponding weight vector and offset, respectively.

$$f_t = \sigma\left(W_f \times [y_{t-1}, u_t] + b_f\right), \tag{6}$$

$$i_t = \sigma(W_i \cdot [y_{t-1}, u_t] + b_i), \tag{7}$$

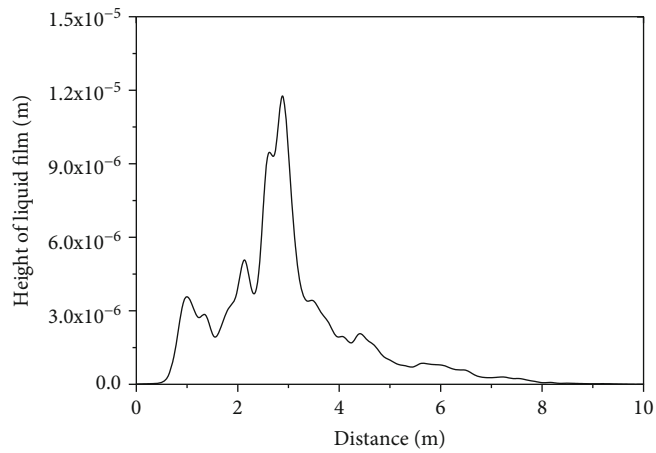

Figure 12: The droplet distribution of a single-rotor model when free stream velocity is 3 m/s.

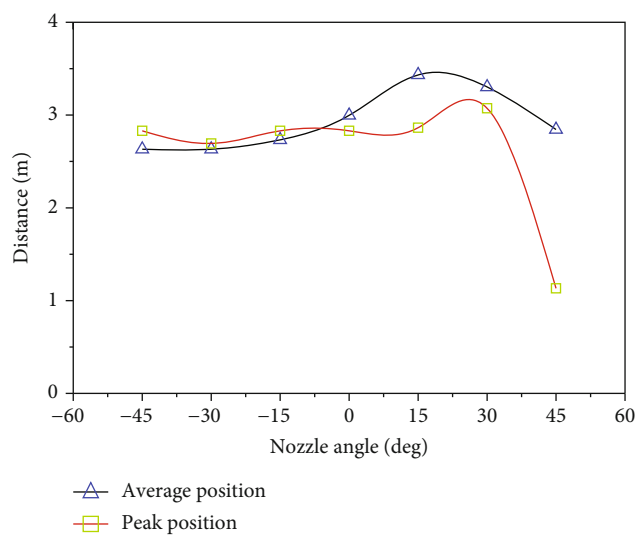

Figure 13: The drift distance for different nozzle angles in hover state when velocity is 3 m/s.

$$o_t = \sigma(W_o \cdot [y_{t-1}, u_t] + b_o). \tag{8}$$

In addition, the candidate memory cell $\tilde{C}_t$ with a tanh function is used to map the input u_t and the previous output state h_{t-1} to the interval $[-1, 1]$, as shown in Equation (9). Afterwards, the current memory cell state C_t can be obtained via Equation (10), which is used to store the long-term state automatically based on the forget gate f_t and input gate i_t. Finally, the output response h_t is calculated by the output gate o_t and the tanh map of memory cell state C_t, which yield Equation (11).

$$\tilde{C}_t = \tanh\,(W_{\tilde{C}} \cdot [y_{t-1}, u_t] + b_c), \tag{9}$$

$$C_t = f_t * C_{t-1} + i_t * \tilde{C}_t, \tag{10}$$

$$y_t = o_t * \tanh\,(C_t). \tag{11}$$

A multilayered LSTM neural network is employed to improve the generalization performance, and the network architecture for time-series prediction is presented in Figure 4(b) [21]. It should be pointed out that the test and prediction process of the LSTM neural network can be performed without the true output dataset, which is the same as the surrogate-based recurrence framework-based ROM.

3. Case Study and Discussion

3.1. The Droplet Drift through Time. The droplet deposition at different moments in the hover state can be obtained via the CFD method directly, and the desired droplet distribution in target area through time can be calculated approximately via the stack of deposition response at each moment, as shown in Figure 5. Let the velocity of free-stream be constant v, and the droplet distribution through time $\varphi_{\text{through time}}$ can be calculated, which yields,

$$\varphi_{\text{through time}} = \varphi_N(x, z, t_N) + \varphi_{N-1}(x + v \cdot \Delta t, z, t_{N-1}) + \cdots + \varphi_1(x + v \cdot (N-1)\Delta t, z, t_1), \tag{12}$$

where φ_k is the droplet distribution that moved along the free stream direction at different time intervals, which can be calculated by the following CFD simulation results.

$$\varphi_k(x, z, t_k) = \Phi_{k+1}(x, z, t_{k+1}) - \Phi_k(x, z, t_k), \tag{13}$$

where $\Phi_k(x, z, t_k)$ is the function of droplet distribution deposited on the ground directly obtained via the CFD method at the corresponding time k.

3.2. The Characteristics of Single-Rotor Model. To investigate the transport and deposition mechanism of droplet, the pressure contours of flow field at different heights are obtained as shown in Figure 6, where the velocity of free stream is 3 m/s, and the rotor is 3 meters above ground. It can be seen that a high-pressure area is located below the rotor, and a region of low-pressure behind the rotor is generated along the direction of free stream, forcing the droplet to move and deposit downstream under the coupled effect of

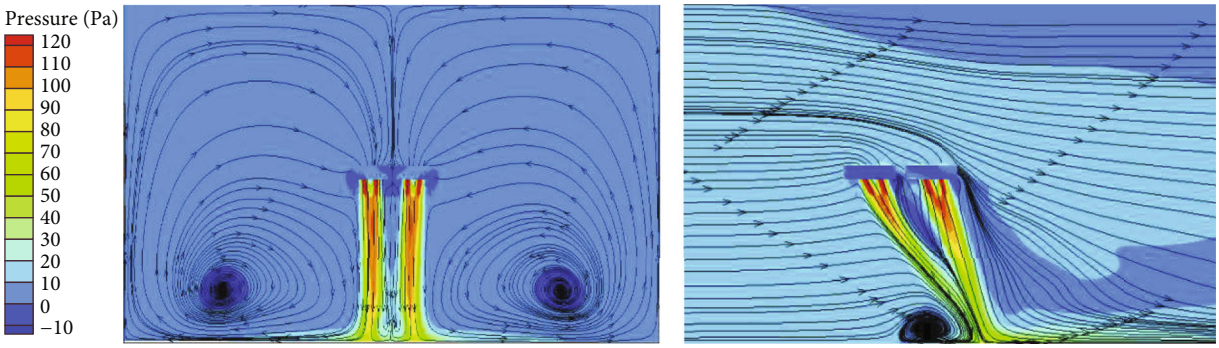

(a) Hover state (b) Flight state at 3m/s

Figure 14: The streamlines of quadrotor flow field.

gravity. In addition, with the increase of the distance from the rotor, the pressure gradient is reduced while the region of low-pressure is enlarged, which may contribute to the drift and transport of droplet near ground. The streamlines of flow field in hover state and flight state with 3 m/s free stream velocity are presented in Figure 7, it can be seen that the characteristics of the flow field, especially the distribution and strength of the vortex structure, are seriously affected by the free stream velocity.

The droplet depositions for various velocities are performed in Figures 8–10, and the top views of droplets trajectory including steady and transient solution when lateral wind velocity is 3 m/s are presented in Figure 11. The simulation results are consistent with the conclusion of flow field analysis performed in Section 3.2. In Figures 8–10, the hover state represents the rotor is hovering and the lateral wind velocity is considered, and the forward flight state means the rotor maintains horizontal flight with a given velocity. It can be found in the simulation of hover state that the peak location of droplet deposition will move downstream with the increase of lateral wind speed.

By changing the initial state of the droplet leaving, the nozzle and variable spraying parameters, such as spraying pressure and nozzle angle, could be used to control the movement and distribution of droplet. The distribution of droplet along the lateral wind direction in the hover state is presented in Figure 12, where the nozzle angle is zero and lateral wind velocity is 3 m/s, and it is indicated that the peak location is about 3 m from the center of rotor and the drift distance is 8 m to 10 m. For various nozzle angles, the distribution distance of droplet in hover state is presented in Figure 13; the negative and positive nozzle angle represents the deflections against and along the lateral wind direction, respectively. The average position $\bar{x}$ is calculated by Equation (14) as follows, where H_i and x_i are the height of liquid film and corresponding position of each grid cell. It can be found that there is little difference for the cases of negative nozzle angle between peak position and average position, while the gap of peak position and average position is enlarged when the nozzle angle is positive especially at 45 deg. In addition, compared with the average position, the peak position is more sensitive to the nozzle angle.

$$\bar{x} = \frac{\sum_{i=1}^{N}(H_i x_i)}{\sum_{i=1}^{N}(H_i)}. \tag{14}$$

3.3. The Characteristics of Quadrotor Model. For the quadrotor model, the steady cases with different velocities of free stream are simulated, which could provide accurate initial value for transient calculation. The height of the rotor from the ground is fixed at 3 m, the coordinates of the rotor center on the horizontal plane are (0, 0), (0, 1.5 m), (1.5 m, 0), and (1.5 m, 1.5 m), respectively. The streamlines of both hover state and forward flight state, which is under the background of total pressure, are presented in Figure 14. It should be noted that, with the near-ground vortex formed around the rotor in the hover state, the flow field structure especially the position and strength of the vortex structure in a forward flight state can be changed significantly by a slight velocity perturbation so that the movement of small and light droplets will be obviously different for various aerodynamic loads.

The trajectory of droplets under steady state with 3 m/s free stream velocity is performed in Figure 15(a). Furthermore, due to the effect of air curtain formed by the rotor flow field, the droplets drift farther along the outside. Based on the steady results, the transient cases are calculated numerically to perform the dynamic process of droplet migration. Figure 15(b) is the transient state of aerial spraying with the velocity of free stream 3 m/s, and it can be found that the drift distance along the lateral direction is much wider than that obtained via steady simulation.

Based on the wall-film boundary condition of the ground, the droplet deposition in the target area can be obtained. For instance, Figure 16 is the droplet distribution on the ground along the direction of free stream, where the nozzle angle is zero and lateral wind velocity is 3 m/s, and it indicates that the peak location is near about 3 meters away from the rotor, which performs a similar deposition distribution characteristic of a single-rotor model shown as Figure 12. In addition, for both the single-rotor model and quadrotor model, the average droplet drift distances defined

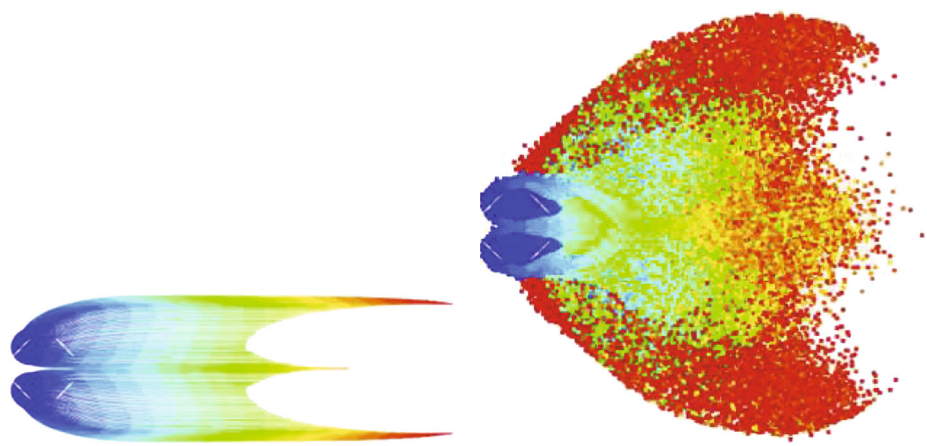

(a) steady state (b) transient state

Figure 15: Droplets trajectory of a quadrotor model when the free stream velocity is 3 m/s.

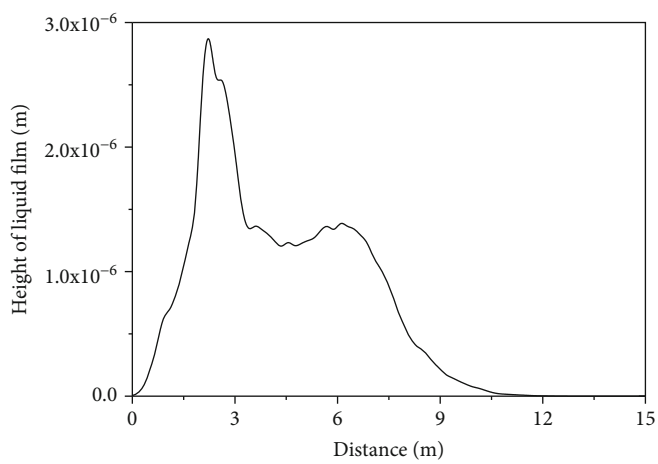

Figure 16: The droplet distribution of quadrotor model when free stream velocity is 3 m/s.

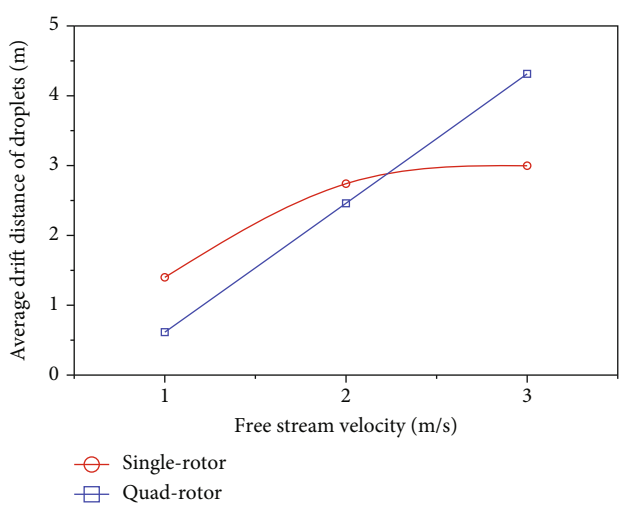

Figure 17: The average drift distance of droplets for different free stream velocities.

as Equation (14) are performed in Figure 17. It can be easily found that the average position of quadrotor model increases approximately linearly with the velocity of free stream, while the average position of single-rotor model increases nonlinearly, which indicates that the droplets deposition characteristics of a single-rotor model is more complicated.

3.4. The Droplet Drift due to Random Lateral Wind. Based on the analysis of flow field and droplet drift for various velocities in the above section, it is implied that the drift distance and distribution of droplets are closely related to lateral wind velocity. It should be noted that to obtain a sufficient amount of computational data with less computing resources, the single-rotor model is used to generate the high-fidelity output data. In addition, to mimic the random lateral wind in the real operation environment, a filter white Gaussian noise signal with 2.5 m/s mean value and low frequency presented in Figure 18 is employed to simulate the value of random lateral wind, which can be obtained via a

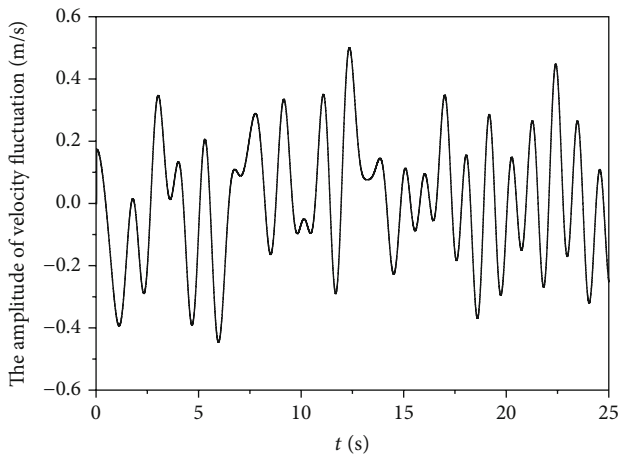

Figure 18: The signal for fluctuation of random lateral wind with 2.5 m/s mean value.

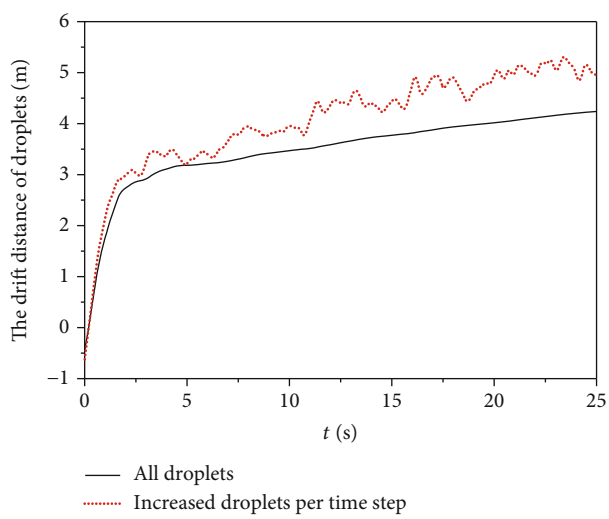

Figure 19: Droplet drift distance with the consideration of random lateral wind.

sum of finite number of harmonic function, namely [26],

$$v(t) = \sum_{i=1}^{100} \bar{v}_i \cos\left(\omega_{v,i} t + \phi_{v,i}\right), \tag{15}$$

where v is the velocity of random lateral wind and $\omega_{v,i}$ and $\phi_{v,i}$ are angular frequency and phase, respectively. The random lateral wind signal can be described by the user-defined function tool in Fluent software, which is compiled with C language and loaded as a boundary condition automatically.

Afterwards, the simulation with 10^4 timesteps in 25 seconds is performed to study the aerial spraying in hover state, and the drift distance between droplet and rotor is presented in Figure 19, where the straight line is the average drift distance of all droplets obtained from Equation (14), and the dot one represents the average drift distance of increased droplets in each time interval. As shown in Figure 19, it takes

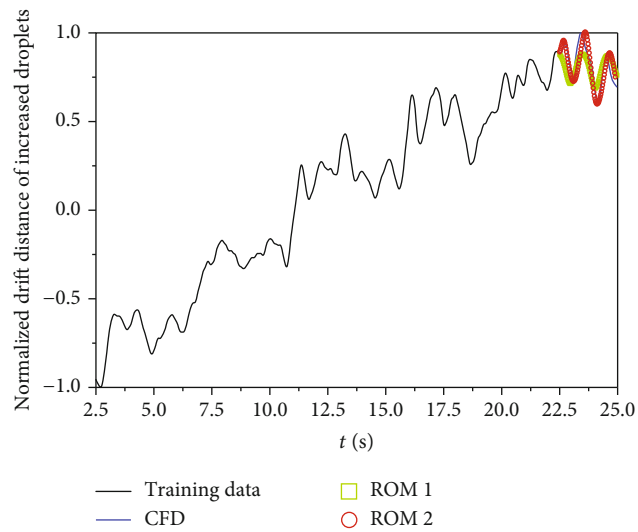

Figure 20: The training and prediction for the drift distance of increased droplets.

about 2.5 seconds for the droplets to reach the ground, then the drift distance of all droplets increases linearly approximately, while the drift distance of increased droplets is markedly changed with the variation of random lateral wind signals. It should be noted that the high-fidelity CFD calculation for the corresponding response of droplet which is subject wind load is time-consuming, i.e., it takes about 1.54×10^6 seconds for the transient calculation of Figure 18 (the computer platform is i7 8700k with 6 cores @3.7 GHz and 40 Gb 2400 MHz memory).

3.5. The Prediction of Droplet Drift via Surrogate-Based Recurrence Framework and LSTM. To predict the drift distance of droplets with the consideration of random lateral wind efficiently and accurately, the LSTM network and surrogate-based recurrence framework are used to establish the ROM, respectively, where the normalized data belong to $[2.5\,\text{s}, 22.5\,\text{s}]$ and $[22.5\,\text{s}, 25\,\text{s}]$ are the training and test datasets, respectively.

In the ROM based on the LSTM neural network, a two-stacked-layer structure with 32 cells in each layer is employed, and mean absolute error function is taken as the error function. In addition, the value of learning rate is given as 0.001 and the Adam optimizer is chosen to complete a 200-epoch training process [27].

In the ROM based on the recursive algorithm, the nonlinear autoregressive exogenous model is used to process the training process, where the number of neurons and is 24, and the delay order $m = n = 1$. The Bayesian regularization algorithm, which can result in good generalization for difficult, small, or noisy datasets, is employed to perform the training process [28]. In the test process, based on the measurable random lateral wind signal, the prediction for the response of aerial spraying system is performed via the surrogate-based recurrence framework without the true output dataset.

The prediction results are presented in Figure 20, and it can be seen that both of the proposed ROMs could

predict the trend of drift distance well, especially the ROM based on the surrogate-based recurrence framework scheme, where ROM 1 and ROM 2 are obtained via LSTM and surrogate-based recurrence framework, respectively. It should be noted that, due to the randomness of droplet motion and high time delay between the instantaneous loading of random lateral wind and droplet deposition, the difficulty of establishing efficient ROM is intensified significantly. In addition, the prediction accuracy of ROM could be further improved by increasing the scale of training data obtained from CFD technique. Furthermore, although it is time-consuming to obtain the training and test datasets via CFD technique, it only takes a fraction of one second to accurately predict the droplet response once the ROM is established. The efficient ROM has potential in designing the close-loop controller for a variable spraying system, which has been applied in fluid-structure interaction system successfully.

4. Conclusions

In this study, the droplet drift of the aerial spraying for various parameters including free-stream velocity, nozzle angle, and random lateral wind are performed numerically, and the distributions of droplets through time for different velocities are calculated to present the overall details. Finally, the efficient ROMs based on the LSTM neural network and surrogate-based recurrence framework are developed, respectively, to predict the droplet drift distance according to the measurable random lateral wind. The CFD data is employed to assess the effectiveness, and the following conclusions can be obtained:

(1) The distributions of droplet can be changed significantly for different nozzle angles, which could be treated as one of the variable spraying parameters

(2) The droplet drift is very sensitive to the wind velocity, in other words, a relatively huge difference of drift distance will be made by a small change of wind velocity

(3) The ROM technique based on surrogate-based recurrence framework and LSTM neural network can be used to predict the droplet drift distance induced by random lateral wind accurately with a low computational cost

Data Availability

All data included in this study are available upon request by contact with the corresponding author.

Conflicts of Interest

The authors declare that they have no known competing interests.

Acknowledgments

This work was supported by the National key research and development program of China (2021YFD1600503), Natural Science Foundation of Hubei Province of China (2020CFB309), and the Key Research and Development Program of Hubei Province of China (2020BBB062).

References

[1] X. Huang, S. Zhang, C. Luo, W. Li, and Y. Liao, "Design and experimentation of an aerial seeding system for rapeseed based on an air-assisted centralized metering device and a multi-rotor crop protection UAV," *Applied Sciences*, vol. 10, no. 24, p. 8854, 2020.

[2] X. Lei, Y. Liao, Q. Zhang, L. Wang, and Q. Liao, "Numerical simulation of seed motion characteristics of distribution head for rapeseed and wheat," *Computers and Electronics in Agriculture*, vol. 150, pp. 98–109, 2018.

[3] F. Ahmad, B. Qiu, X. Dong et al., "Effect of operational parameters of UAV sprayer on spray deposition pattern in target and off-target zones during outer field weed control application," *Computers and Electronics in Agriculture*, vol. 172, article 105350, 2020.

[4] Q. Guo, Y. Zhu, Y. Tang et al., "CFD simulation and experimental verification of the spatial and temporal distributions of the downwash airflow of a quad-rotor agricultural UAV in hover," *Computers and Electronics in Agriculture*, vol. 172, article 105343, 2020.

[5] K. Li, J. Kou, and W. Zhang, "Deep neural network for unsteady aerodynamic and aeroelastic modeling across multiple Mach numbers," *Nonlinear Dynamics*, vol. 96, no. 3, pp. 2157–2177, 2019.

[6] C. Song, Z. Zhou, Y. Zang et al., "Variable-rate control system for UAV-based granular fertilizer spreader," *Computers and Electronics in Agriculture*, vol. 180, article 105832, 2021.

[7] J. Li, Y. Lan, and Y. Shi, "Research progress on airflow characteristics and field pesticide application system of rotary-wing UAV," *Transactions of the Chinese Society of Agricultural Engineering*, vol. 34, pp. 104–118, 2018, (In Chinese).

[8] C. Wang, J. Song, X. He, Z. Wang, S. Wang, and Y. Meng, "Effect of flight parameters on distribution characteristics of pesticide spraying droplets deposition of plant-protection unmanned aerial vehicle," *Transactions of the Chinese Society of Agricultural Engineering*, vol. 33, pp. 109–116, 2017, (In Chinese).

[9] C. Wang, X. He, X. Wang et al., "Distribution characteristics of pesticide application droplets deposition of unmanned aerial vehicle based on testing method of deposition quality balance," *Transactions of the Chinese Society of Agricultural Engineering*, vol. 32, pp. 89–97, 2018, (In Chinese).

[10] M. Lv, S. Xiao, Y. Tang, and Y. He, "Influence of UAV flight speed on droplet deposition characteristics with the application of infrared thermal imaging," *International Journal of Agricultural and Biological Engineering*, vol. 12, pp. 10–17, 2019.

[11] Y. Zheng, S. Yang, X. Liu et al., "The computational fluid dynamic modeling of downwash flow field for a six-rotor UAV," *Frontiers of Agricultural Science and Engineering*, vol. 5, no. 2, pp. 159–167, 2018.

[12] W. Qin, B. Qiu, X. Xue, C. Chen, Z. Xu, and Q. Zhou, "Droplet deposition and control effect of insecticides sprayed with an

unmanned aerial vehicle against plant hoppers," *Crop Protection*, vol. 85, pp. 79–88, 2016.

[13] Y. Chen, C. Hou, Y. Tang, J. Zhuang, J. Lin, and S. Luo, "An effective spray drift-reducing method for a plant-protection unmanned aerial vehicle," *International Journal of Agricultural and Biological Engineering*, vol. 12, no. 5, pp. 14–20, 2019.

[14] J. Wang, Y. Lan, H. Zhang et al., "Drift and deposition of pesticide applied by UAV on pineapple plants under different meteorological conditions," *International Journal of Agricultural and Biological Engineering*, vol. 11, no. 6, pp. 5–12, 2018.

[15] S. Wen, J. Han, Z. Ning et al., "Numerical analysis and validation of spray distributions disturbed by quad- rotor drone wake at different flight speeds," *Computers and Electronics in Agriculture*, vol. 166, article 105036, 2019.

[16] S. Wen, N. Shen, J. Zhang et al., "Single-rotor UAV flow field simulation using generative adversarial networks," *Computers and Electronics in Agriculture*, vol. 167, article 105004, 2019.

[17] B. Zhang, Q. Tang, L. Chen, R. Zhang, and M. Xu, "Numerical simulation of spray drift and deposition from a crop spraying aircraft using a CFD approach," *Biosystems Engineering*, vol. 166, pp. 184–199, 2018.

[18] B. Glaz, L. Liu, and P. P. Friedmann, "Reduced-order nonlinear unsteady aerodynamic modeling using a surrogate-based recurrence framework," *AIAA Journal*, vol. 48, no. 10, pp. 2418–2429, 2010.

[19] W. Zhang, B. Wang, Z. Ye, and J. Quan, "Efficient method for limit cycle flutter analysis Based on nonlinear aerodynamic reduced-order models," *AIAA Journal*, vol. 50, no. 5, pp. 1019–1028, 2012.

[20] J. Li, Y. Shi, Y. Lan, and S. Guo, "Vertical distribution and vortex structure of rotor wind field under the influence of rice canopy," *Computers and Electronics in Agriculture*, vol. 159, pp. 140–146, 2019.

[21] W. Li, X. Gao, and H. Liu, "Efficient prediction of transonic flutter boundaries for varying Mach number and angle of attack via LSTM network," *Aerospace Science and Technology*, vol. 110, article 106451, 2021.

[22] R. Huang, H. Liu, Z. Yang, Y. Zhao, and H. Hu, "Nonlinear reduced-order models for transonic aeroelastic and aeroservoelastic problems," *AIAA Journal*, vol. 56, no. 9, pp. 3718–3731, 2018.

[23] A. D. Gosman and E. Loannides, "Aspects of computer simulation of liquid-fueled combustors," *Journal of Energy*, vol. 7, no. 6, pp. 482–490, 1983.

[24] T. Lin, B. G. Horne, P. Tino, and C. L. Giles, "Learning long-term dependencies in NARX recurrent neural networks," *IEEE Transactions on Neural Networks*, vol. 7, no. 6, pp. 1329–1338, 1996.

[25] S. Hochreiter and J. Schmidhuber, "Long short-term memory," *Neural Computation*, vol. 9, no. 8, pp. 1735–1780, 1997.

[26] D. E. Raveh, "Identification of computational-fluid-dynamics based unsteady aerodynamic models for aeroelastic analysis," *Journal of Aircraft*, vol. 41, no. 3, pp. 620–632, 2004.

[27] Z. Zhang, "Improved Adam optimizer for deep neural networks," in *2018 IEEE/ACM 26th International Symposium on Quality of Service*, Banff, AB, Canada, 2018.

[28] F. Burden and D. Winkler, *Bayesian Regularization of Neural Networks. Artificial Neural Networks: Methods and Applications*, Humana press, Totowa, NJ, 2009.